

# **Tricritical Casimir Forces in $^3\text{He}$ - $^4\text{He}$ Wetting Films**

Von der Fakultät Mathematik und Physik der Universität Stuttgart  
zur Erlangung der Würde eines Doktors der Naturwissenschaften  
(Dr. rer. nat.) genehmigte Abhandlung

vorgelegt von  
**Nima Farahmand Bafi**  
aus Teheran

Hauptberichter: Prof. Dr. Siegfried Dietrich

Mitberichter: Prof. Dr. Udo Seifert

Tag der mündlichen Prüfung: 8.2.2017

Max-Planck-Institut für Intelligente Systeme, Stuttgart &  
Institut für Theoretische Physik IV, Universität Stuttgart

2017



Ich versichere hiermit, dass ich, Nima Farahmand Bafi, die vorliegende Arbeit selbständig angefertigt habe und sowohl wörtliche, als auch sinngemäß entlehnte Stellen als solche kenntlich gemacht habe. Die Arbeit hat in gleicher oder ähnlicher Form noch keiner anderen Prüfungsbehörde vorgelegen.

Stuttgart, den 9.12.2016

Nima Farahmand Bafi



# Contents

<b>1. Introduction</b>	<b>7</b>
<b>2. Theoretical background</b>	<b>11</b>
2.1. Bulk critical phenomena . . . . .	11
2.2. Tricritical point . . . . .	15
2.3. Surface effects . . . . .	17
2.4. Wetting phenomena . . . . .	19
2.5. Finite-size scaling . . . . .	22
2.6. Critical Casimir effect . . . . .	26
2.7. Wetting films and critical Casimir forces . . . . .	27
<b>3. Helium mixtures</b>	<b>29</b>
3.1. Bulk phase diagram . . . . .	29
3.2. Superfluid order parameter . . . . .	33
3.3. Helium wetting films . . . . .	34
<b>4. Phase diagram of fluid phases in <math>^3\text{He}</math> - <math>^4\text{He}</math> mixtures</b>	<b>37</b>
4.1. The model . . . . .	38
4.2. Mean field approximation . . . . .	40
4.3. Phase diagrams . . . . .	43
4.3.1. Phase diagram for a classical binary liquid mixture . . . . .	44
4.3.2. Phase diagram including the superfluid phase . . . . .	47
<b>5. Tricritical Casimir forces in <math>^3\text{He}</math> - <math>^4\text{He}</math> wetting films</b>	<b>63</b>
5.1. The model . . . . .	66
5.1.1. Mean field approximation . . . . .	68
5.1.2. Limiting case: bulk phase diagram . . . . .	71
5.2. Layering and wetting for short-ranged surface fields . . . . .	73
5.2.1. Layering and wetting for classical binary liquid mixtures . . . . .	74
5.2.2. Layering and wetting for $^3\text{He}$ - $^4\text{He}$ mixtures . . . . .	78
5.2.3. Tricritical Casimir forces . . . . .	87

<b>6. Summary</b>	<b>95</b>
<b>7. Zusammenfassung</b>	<b>101</b>
<b>Acknowledgments</b>	<b>107</b>
<b>Appendices</b>	<b>109</b>
A. Scaling form of the Gibbs free energy . . . . .	109
B. Mean field approximation for the lattice model in section 5.1.1 . . . . .	112
<b>Bibliography</b>	<b>119</b>
<b>Curriculum vitae</b>	<b>127</b>

# 1. Introduction

One of the beauties of physics is the existence of certain universal mechanisms, which lead to similar phenomena in completely different systems. In 1948 Hendrik Casimir predicted an attractive force between two parallel uncharged perfectly conducting plates in vacuum. Named after him, these Casimir forces arise due to the restrictions, which the plates impose on the zero-point fluctuations of the electromagnetic fields [1]. Just 30 years later, in 1978 Fisher and de Gennes [2], and in 1981 Symanzik [3] predicted an analogue of the Casimir force within soft matter systems, which results from the confinement of the critical thermal fluctuations. The thermal fluctuations occur on the scale of the bulk correlation length, which diverges upon approaching the critical point of the system [4]. In this limit the fluid-mediated force present in confined fluids [5] acquires the *universal* long-ranged contribution, known as critical Casimir force (CCF) [2]. Although these forces are negligible on large scales, at sub-micrometer scale they become comparable with the thermal energy and thus, contribute to the physical and thermodynamical properties of the systems at these scales (e.g., controlling the phase behavior of colloidal particles, their rheological properties or spatial organizations).

The study of the CCFs is typically carried out in the framework of the finite-size scaling theory, which states that near the bulk critical point the *singular* behavior of thermodynamic quantities are governed by the ratio of the characteristic system size  $L$  and the bulk correlation length  $\xi$  [6–8]. Accordingly, CCF can be expressed in terms of a universal dimensionless scaling function of the scaling variable  $L/\xi$ . The shape of the scaling function depends on the bulk universality class of the confined fluid and on the surface universality classes of the confining surfaces [9]. The bulk universality class of a critical fluid is determined by the spatial dimension, the range of the interactions, and the dimension of the order parameter (OP) associated with the underlying second-order phase transition. In turn, the surface universality class of the confining surfaces is related to the boundary conditions (BCs) [6, 9, 10] imposed by the surfaces on the OP [10]. Interestingly, not only the form of the scaling function depends on BCs but also its sign; for symmetric BCs the scaling function of CCF is negative and the CCF

---

Parts of this chapter are reprinted with permission from [N. Farahmand Bafi, A. Maciolek, and S. Dietrich, Phys. Rev. E **95**, 032802 (2017).] Copyright 2017 by the American Physical Society.

## 1. Introduction

---

is attractive, whereas non-symmetric BCs lead to positive values of the scaling function corresponding to repulsive CCF.

The first experimental evidences for the CCF have been provided by their effect on the equilibrium thickness of the wetting films of classical binary liquid mixtures [11–14],  $^4\text{He}$  [15, 16], and  $^3\text{He}$ - $^4\text{He}$  mixtures [17, 18]. For wetting films of classical binary liquid mixtures such effects occur near the critical end point of the liquid, at which the line of critical points of liquid–liquid demixing transitions intersects the liquid–vapor coexistence line [19]. The CCFs in wetting films originate from the restriction and modification of the critical fluctuations of the composition of the mixture imposed on one side by the solid substrate and on the other side by the emerging liquid–vapor interface. The CCF acts by moving the liquid–vapor interface and together with the omnipresent background dispersion forces and gravity, determines the equilibrium thickness of the wetting films [11–14]. The dependence of the film thickness on temperature provides an indirect measurement of CCF [19, 20]. This approach also allows one to probe the universal properties of the CCF encoded in its scaling function [20]. By varying the undersaturation of the vapor phase one can tune the film thickness and thus determine the scaling behavior of the CCF as function of temperature and film thickness [20–22]. Classical binary liquid mixtures near their demixing transition belong to the three-dimensional Ising universality class. The surfaces confining them belong to the so-called normal transition [9], which is characterized by a strong effective surface field acting on the deviation of the concentration from its critical value serving as the OP. The surface field describes the preference of the surface for one of the two species forming the binary liquid mixture. Within wetting films the surface attracts one of the species and thus effectively shifts the other component towards the emerging liquid–vapor interface. Thus wetting films of classical binary liquid mixtures are often characterized by opposing surface fields ( $(+, -)$  BCs), which results in repulsive CCFs [11–14].

In wetting films of  $^4\text{He}$  [15], the CCF originates from the confined critical fluctuations associated with the continuous superfluid phase transition along the so-called  $\lambda$ -line. Similarly as for the classical binary liquid mixtures, here the CCF emerges near that critical end point, where the  $\lambda$ -line hits the line of first-order liquid–vapor phase transitions of  $^4\text{He}$ . Capacitance measurements of the equilibrium thickness of  $^4\text{He}$  wetting films have provided strong evidence for an attractive CCF [15, 16] in quantitative agreement with the theoretical predictions [20–22] for the corresponding bulk  $XY$  universality class with *symmetric* Dirichlet–Dirichlet BCs  $(O, O)$ , which corresponds to the vanishing of the superfluid OP with  $O(2)$  symmetry both at the surface of the substrate and at the liquid–vapor interface. The scaling function of this CCF has, to a certain extent, been determined analytically [20–26] and by using Monte Carlo simulations [27–32]. Their results are in excellent agreement with the experimental data.

---

Similar measurements [17] for wetting films of  $^3\text{He}$ - $^4\text{He}$  mixtures performed near the tricritical end point, at which the line of tricritical points encounters the surface of first-order liquid-vapor phase transitions, revealed a repulsive tricritical Casimir force (TCF). In turn, this points towards non-symmetric BCs for the superfluid OP, which is surprising because in this system there are no surface fields which couple to the superfluid OP. However, there is a subtle physical mechanism which can create  $(+, O)$  and thus non-symmetric BCs. As argued in Ref. [17], because the  $^3\text{He}$  isotope is lighter than  $^4\text{He}$  it experiences a larger zero-point motion and hence, it occupies a larger volume than  $^4\text{He}$ . As a result,  $^3\text{He}$  atoms are effectively expelled from the rigid solid substrate and tend to gather at the soft liquid-vapor interface. This leads to an effective attraction of  $^4\text{He}$  atoms to the solid substrate so that a  $^4\text{He}$ -rich layer forms near the substrate-liquid interface. Due to the increased  $^4\text{He}$  concentration this layer may become superfluid at temperatures already above the line of onset of superfluidity in the bulk [33]. Thus the two interfaces impose a nontrivial concentration profile across the film, which in turn couples to the superfluid OP. Explicit calculations [24, 25] within the vectorized Blume-Emery-Griffiths (VBEG) model of helium mixtures [34–36] have demonstrated that the concentration profile indeed induces indirectly non-symmetric BCs for the superfluid OP. A semi-quantitative agreement with the experimental data given in Ref. [17] has been found for the TCF, computed by assuming a symmetry-breaking  $(+)$  BC at the substrate-liquid interface and a Dirichlet  $(O)$  BC at the liquid-vapor interface. However, the VBEG model employed in Refs. [24, 25] does not incorporate the vapor phase and hence cannot exhibit wetting films. In these studies the confinement of the liquid between the substrate and the liquid-vapor interface has been modeled by a slab geometry with the boundaries introduced by fiat, mimicking the actual self-consistent formation of wetting films and thus differing from the actual experimental setup.

In order to provide a more realistic description of the experimental setup reported in Ref. [17] one has to introduce a model, which allows for the occurrence of a vapor phase and thus of wetting films. This is the subject of the present thesis. The model proposed here is a lattice model, which in addition to the sites occupied by  $^3\text{He}$  or  $^4\text{He}$  atoms allows for vacant sites and as a result, exhibits vapor phase if the number of vacant sites is sufficiently large. Furthermore, it includes the continuous  $O(2)$  symmetry of the superfluid OP. With proper set of coupling constants, the model phase diagram resembles that of  $^3\text{He}$ - $^4\text{He}$  mixtures. For a semi-infinite system with surfaces fields coupled to the number densities of  $^3\text{He}$  and  $^4\text{He}$ , the model exhibits wetting and therefore, enables one to reproduce the experimental results for the film thickness measurements of  $^3\text{He}$ - $^4\text{He}$  wetting films and to calculate the scaling functions of TCF. The model is studied in spatial dimension  $d = 3$  within mean field theory which, up to logarithmic corrections, captures the universal behavior of the TCF near the tricritical point of  $^4\text{He}$

## 1. Introduction

---

$^3\text{He}$ - $^4\text{He}$  mixtures. However, this approximation is insufficient near the critical points of the  $\lambda$ -transition, because for the tricritical phenomena the upper critical dimension is  $d^* = 3$ , whereas for the critical ones it is  $d^* = 4$ .

The thesis is organized as follows: In the next chapter, the theoretical background underlying the present thesis is briefly overviewed. Next, the properties of helium and its bulk behavior are reviewed and the experimental results of the measurements of TCF within wetting films of helium mixtures are discussed (chapter 3). Chapters 4 and 5 are devoted to the own results. In chapter 4 the model is proposed and after discussing some of the possible topologies of the bulk phase diagram, the fluid parts of the bulk phase diagram of the  $^3\text{He}$ - $^4\text{He}$  mixtures are obtained. In chapter 5 a semi-infinite system is considered and the model introduced in chapter 4 is modified by introducing surface fields, which couple to the number densities of  $^3\text{He}$  and  $^4\text{He}$ . In the present thesis only short-range surface fields are considered. First the wetting properties of the model are studied. Then the experimental results of Ref. [17] are reproduced and finally, the TCF within  $^3\text{He}$ - $^4\text{He}$  wetting films and its scaling function are calculated. At the end, the results are summarized with a conclusion and an outlook (chapter 6).

## 2. Theoretical background

In this chapter the basic concepts of different phenomena underlying the tricritical Casimir forces (TCFs) in  $^3\text{He}$ - $^4\text{He}$  wetting films are briefly reviewed. Section 2.1 focuses on the bulk critical phenomena, universality and the scaling hypothesis. In Sec. 2.2 the tricritical point and the tricritical scaling hypothesis are discussed. Next, a semi-infinite system is considered and it is explained how the bulk critical behavior of a system is changed at the surface (Sec. 2.3). Section 2.4 focuses on wetting phenomena; in particular the formation of liquid films on solid substrates are discussed. In Sec. 2.5 systems in the film geometry are considered. There, it is shown how the finite-size effects modify the bulk critical behavior of the system. One of the manifestations of these effects is the critical Casimir force (CCF). This is the subject of Sec. 2.6. Finally, in Sec. 2.7 it is explained how critical Casimir forces contribute to the determination of the equilibrium thickness of wetting films.

### 2.1. Bulk critical phenomena

Critical phenomena refer to the thermodynamic properties of a system near its critical point of the second-order phase transitions [4]. A simple example of a system, exhibiting a second-order phase transition is a ferromagnet which at the critical temperature  $T_c$ , the so-called Curie temperature, exhibits a continuous phase transition from the paramagnetic phase to the ferromagnetic one. For temperatures  $T$  above  $T_c$  the magnetization  $M$  is zero (paramagnetic phase), whereas for  $T < T_c$  spontaneous magnetization  $M$  occurs (ferromagnetic phase). In the ferromagnetic system,  $M$  serves as the order parameter (OP), a parameter which is zero above the critical point and increases continuously below<sup>1</sup> it [37]. The OP can be properly defined in any system exhibiting second-order phase transition. Consider, for example, the critical point of liquid-vapor phase transitions in a one component system. Along the line  $L_{l,v}$  of the

---

Parts of this chapter are reprinted with permission from [N. Farahmand Bafi, A. Maciolek, and S. Dietrich, Phys. Rev. E **95**, 032802 (2017).] Copyright 2017 by the American Physical Society.

<sup>1</sup>For systems with lower critical points the zero and nonzero values of the OP occur below and above the critical point, respectively.

## 2. Theoretical background

---

first-order liquid-vapor phase transitions a liquid phase with density  $n_l$  coexists with vapor phase with density  $n_v$ . Upon approaching the critical point of liquid-vapor phase transitions along  $L_{l,v}$ , the difference between the densities of the liquid and the vapor phases reduces and ultimately, at the critical point the two phases become identical; here  $\Delta n := n_l - n_v$  serves as the OP. In the following the ferromagnetic system is considered. The concepts which will be discussed can be adapted into other systems.

In the ferromagnetic system above  $T_c$  the magnetization is zero and hence, the system is rotationally invariant. However, below  $T_c$  spontaneous magnetization occurs and the rotational symmetry is broken<sup>2</sup>. Due to the difference in the symmetries below and above  $T_c$ , the behavior of the system in these two regions is described by different functions of the thermodynamic variables. These functions cannot be continued analytically and therefore,  $T_c$  is a singular point [4]. Near the critical point one can assume that the only important quantity is the OP. If the OP changes by  $dM$ , the work done on the system is

$$dW = HdM, \quad (2.1)$$

which defines the conjugate field  $H$  to the OP. In the case of the ferromagnetic system  $H$  is the magnetic field. Suppose that the total volume  $V$  and the total number of particles  $N$  are fixed. Using  $(H, T)$  as independent variables, the Gibbs free energy  $G(H, T)$  of the system is given by [4]

$$G(H, T) = -k_B T \ln(\text{Tr} e^{-\mathcal{H}/k_B T}), \quad (2.2)$$

where  $\mathcal{H}$  is the Hamiltonian of the system and  $k_B$  is the Boltzmann constant. Having the Gibbs free energy  $G(H, T)$  one can derive different thermodynamic quantities as [4]

$$\begin{aligned} \frac{M}{V} &= -\frac{1}{V} \frac{\partial G}{\partial H}, \\ \chi &= -\frac{1}{V} \frac{\partial M}{\partial H}, \\ C_V &= T \frac{\partial S}{\partial T} = -T \frac{\partial^2 G}{\partial T^2}, \end{aligned} \quad (2.3)$$

where  $S = -\frac{\partial G}{\partial T}$  is the entropy,  $\chi$  is the susceptibility, and  $C_V$  is the heat capacity<sup>3</sup> at fixed volume.

Since the critical point is a singular point, the Gibbs free energy  $G$  and the different thermodynamic quantities derived from it have a singular contribution at  $T_c$ . This singular part is often divergent upon approaching  $T_c$ . One of the most astonishing features

---

<sup>2</sup>Such symmetry breaking does not occur in every system with second-order phase transitions (e.g., it does not occur in the liquid-vapor phase transitions). However, what follows in this chapter applies to the second-order phase transitions in general [4].

<sup>3</sup>The heat capacity at fixed quantity  $Y$  is defined as  $C_Y := T \frac{\partial S}{\partial T} |_Y$

of the critical phenomena is that the singular behavior of the thermodynamic quantities is governed by power-laws, which are characterized by universal exponents [4, 38]. Accordingly, defining the reduced temperature  $t$  as

$$t = \frac{T - T_c}{T_c} \quad (2.4)$$

in the limit  $t \rightarrow 0$ , the singular parts of the thermodynamic quantities  $C_V$ ,  $M$ , and  $\chi$  defined in Eq. (2.3) are assumed to take the following forms [4, 38]

$$\begin{aligned} C_V &\sim |t|^{-\alpha}, \\ M &\sim |t|^\beta, \\ \chi &\sim |t|^{-\gamma}, \\ M &\sim |H|^{1/\delta}, \quad t = 0, \end{aligned} \quad (2.5)$$

where it is assumed that the singularities are the same type whether the critical point is approached from above or from below. (The relation  $A \sim x^b$  denotes that close to the critical point, up to the leading order  $A = A_0 x^b$ , where  $A_0$  is the amplitude<sup>4</sup>.) The four equations in Eq. (2.5) define four critical exponents  $\{\alpha, \beta, \gamma, \delta\}$ . In order to define the other critical exponents, first one can assume that the OP is given by an OP density as

$$M = \left\langle \int d^3r m(\mathbf{r}) \right\rangle, \quad (2.6)$$

where  $\mathbf{r}$  denotes the position vector,  $d^3r = d\mathbf{r}$  is the volume element, and  $m(\mathbf{r})$  is the OP density (note that  $M$  is independent of the position). Then, one defines the two point correlation function  $\Gamma(\mathbf{r}, \mathbf{r}')$  as

$$\Gamma(\mathbf{r}, \mathbf{r}') := \langle m(\mathbf{r})m(\mathbf{r}') \rangle - \langle m(\mathbf{r}) \rangle \langle m(\mathbf{r}') \rangle. \quad (2.7)$$

For rotationally homogenous systems, the two point correlation function decays as [4]

$$\Gamma(\mathbf{r}, \mathbf{r}')|_{t \rightarrow 0} = \Gamma(\mathbf{r} - \mathbf{r}')|_{t \rightarrow 0} \rightarrow \left| \frac{1}{\mathbf{r} - \mathbf{r}'} \right|^{d-2+\eta} e^{-|\mathbf{r}-\mathbf{r}'|/\xi}, \quad (2.8)$$

where  $\eta$  is another critical exponent,  $d$  is the spatial dimension, and  $\xi$  is the bulk correlation length. The bulk correlation length diverges upon approaching  $T_c$ . Close to  $T_c$  this divergence follows the power-law [4]

$$\xi \sim |t|^{-\nu}, \quad (2.9)$$

---

<sup>4</sup>Note that the amplitudes in Eq. (2.5) are not universal and are different above or below  $T_c$ . However, their ratio for each quantity is universal.

## 2. Theoretical background

---

which defines another critical exponent  $\nu$ . Note that due to the divergences of  $\xi$  upon approaching  $T_c$ , it follows from Eq. (2.8) that

$$\Gamma(\mathbf{r} - \mathbf{r}')|_{t=0} \sim \left| \frac{1}{\mathbf{r} - \mathbf{r}'} \right|^{d-2+\eta}. \quad (2.10)$$

The six critical exponents defined above are related due to the scaling laws. These relations are derived in Appendix A. According to these relations only two of these exponents are independent.

As mentioned before, the spectacular fact about the critical exponents is that they are universal, i.e., they are independent of the microscopic details of the system [4]. This arises from the scale invariance of the thermal fluctuations near the critical point. One of the experiments showing the universality of the critical exponents is the one carried out by Guggenheim [39], in which he studied the behavior of the density  $n$  versus temperature for different materials near the critical point of their liquid–vapor phase transitions. He observed that although the critical density  $n_c$  and the critical temperature  $T_c$  of these materials differ, for all of them the density of the liquid phase  $n_l$  and of that of the vapor phase  $n_v$  follow the relation [39]

$$\frac{n_l - n_v}{n_c} = \frac{7}{2}(1 - T/T_c)^{1/3}. \quad (2.11)$$

Considering the order parameter  $\Delta n = n_l - n_v$ , Eq. (2.11) renders  $\Delta n \sim t^{1/3}$  which, due to the definition of the critical exponent  $\beta$  in Eq. (2.5), implies that  $\beta = 1/3$ . A more precise value of  $\beta$  has been obtained theoretically based on the renormalization group (RG), a concept which has provided the first theoretical explanation of the universality of critical exponents [40,41]. The basic underlying idea in the RG approach is to change the length scale of the system and to rescale the relevant system parameters such that the Hamiltonian keeps its form. These transformations lead to a flow of the parameters in their phase space towards a fixed point at which the system parameters (and thus the system) remain unchanged upon further transformations. This corresponds either to the zero value or to the infinite value of the bulk correlation length  $\xi$ . The case  $\xi = 0$  corresponds to the infinite temperature, whereas  $\xi = \infty$  means that the system is at the critical point. Considering the second case, by studying the system upon approaching the fixed point one obtains the critical exponents. If two systems reach the same fixed points in the flow of RG transformations they have the same critical exponents [4]. Therefore, based on RG analysis, different critical points are categorized into different universality classes. Within each universality class the systems share the same critical exponents and thus, the same critical behavior of the different thermodynamic quantities. The universality class of the system depend on the spatial dimension, the range of the interactions, and the dimension of the OP. The ferromagnetic system belongs to the Ising

universality class, in which the OP is a scalar. A two dimensional OP belongs to the  $XY$  universality class, whereas a three dimensional one corresponds to the Heisenberg universality class.

The modern studies of the critical phenomena are mostly based on the scaling theory, which was first introduced in 1965 for describing the critical points in simple fluids [42, 43]. Scaling hypothesis states that since the correlation length diverges upon approaching the critical point, it is the dominating characteristic length scale near the critical point [4]. Based on the scaling hypothesis the singular parts of thermodynamic quantities are expressed in terms of dimensionless universal scaling functions of the relevant scaling variables like the ratios of the geometric length scales and the correlation length. (These scaling functions are universal in the sense that their shapes depend only on the universality class of the system.) One way to implement the scaling hypothesis is to express the correlation function in Eq. (2.8) in terms of the variables  $|\mathbf{r} - \mathbf{r}'|/\xi \sim |\mathbf{r} - \mathbf{r}'||t|^{-\nu}$  and  $H\xi^w \sim H|t|^{-\nu w}$  with some exponent  $w$ , and to obtain the scaling form of other quantities using the relation between the different quantities. Such implementation leads to the Widoms's scaling law for the singular part of the Gibbs free energy density as (see Appendix A for the derivation)

$$g = \frac{G}{V} \sim |t|^{2-\alpha} \mathcal{P}_{\pm}(H/|t|^{\Delta}), \quad (2.12)$$

where  $H/|t|^{\Delta}$  is the scaling variable with  $\Delta = \beta + \gamma$  being the cross-over exponent, and  $\mathcal{P}_{\pm}$  is the universal scaling function with  $\pm$  denoting the regions below or above the critical point. Likewise, close to the critical point all other thermodynamic quantities in Eq. 2.3 can be expressed via universal scaling functions similar to Eq. (2.12) (see Appendix A).

## 2.2. Tricritical point

In the previous section the scaling hypothesis for a simple critical point have been discussed. The critical point is the end of the two-phase coexistence line, at which the two phases become identical. By analogy to this definition, the tricritical point is defined as the end of a line of three-phase coexistence, where all three phases become identical. One of the first observations of the tricritical point has been in a four-component mixture of  $(\text{NH}_4)_2\text{SO}_4$ , water, ethanol and benzene, where for suitable values of concentrations and temperature three-phase coexistence was observed [43, 44]. The other examples of systems showing tricritical point are the antiferromagnetic materials (also known as metamagnets). In these systems the phase transition between the antiferromagnetic and the paramagnetic phases is of second-order for zero magnetic field. Upon increasing

## 2. Theoretical background

---

the magnetic field the temperature of the second-order phase transitions decreases and ultimately, upon further increase of the magnetic field, the phase transition becomes of first-order. This change occurs at a tricritical point [43, 45]. As will be discussed in the next chapter  $^3\text{He}$ - $^4\text{He}$  mixtures exhibit a line of tricritical points as well.

Like in the case of critical points, close to a tricritical point the singular part of the thermodynamic quantities are universal, which can be expressed via universal scaling functions similar to Eq. (2.12). However, the tricritical scaling is more complicated and requires more scaling fields [43]. The formulation of the scaling hypothesis for the tricritical point tc has been developed in Refs. [43, 46–50]. Accordingly, a full description of the tricritical scaling requires four fields  $\{\tau, h_i | i = 1, 2, 3\}$ , where  $h_1$  is the ordering field, whereas  $\tau$ ,  $h_2$  and  $h_3$  are the fields expressing the deviations from the tricritical point. The field  $\tau$  is the reduced temperature given by

$$\tau = \frac{T - T_{\text{tc}}}{T_{\text{tc}}}, \quad (2.13)$$

with  $T_{\text{tc}}$  being the temperature of the tricritical point, whereas the fields  $h_2$  and  $h_3$  are combinations of different thermodynamic quantities.

By analogy to the scaling form in Eq. (2.12) one can postulate the following scaling form for the singular part of the Gibbs free energy density around the tricritical point [43]

$$g(\tau, \{h_i | i = 1, 2, 3\}) \sim |\tau|^{2-\alpha_t} \mathcal{G}_{\pm}(\{h_i/|\tau|^{\phi_i}\}), \quad (2.14)$$

where  $\mathcal{G}_{\pm}$  is the universal scaling function,  $\{\phi_i | i = 1, 2, 3\}$  are the tricritical cross-over exponents controlling the importance of the corresponding field near  $\tau = 0$ , and  $\alpha_{\tau}$  is the tricritical counterpart of the exponent  $\alpha$  defined in Eq. (2.5).

Note that, the expression in Eq. (2.14) follows also from the requirement that near tricritical point the singular part of the Gibbs free energy  $G(\tau, \{h_i\})$  is a generalized homogeneous function [38, 43, 49, 51, 52]. This requirement for the Gibbs free energy density implies [43]

$$g(\tau, \{h_i | i = 1, 2, 3\}) = \lambda^{-d} g(\lambda^y \tau, \{\lambda^{y_i} h_i\}), \quad (2.15)$$

where  $\lambda$  is a (positive) real number,  $d$  is chosen as spatial dimension to make a connection with RG analysis [43], and the exponents  $y$  and  $\{y_i | i = 1, 2, 3\}$  are tricritical exponents. By choosing  $\lambda = |\tau|^{1/y}$  one obtains the same expression as in Eq. (2.14) provided that

$$\mathcal{G}_{\pm}(\{|\tau|^{-y_i/y} h_i\}) \equiv g(\pm 1, \{|\tau|^{-y_i/y} h_i\}) \quad \text{with } i = 1, 2, 3, \quad (2.16)$$

and

$$2 - \alpha_{\tau} = d/y, \quad \phi_i = y_i/y, \quad \text{with } i = 1, 2, 3. \quad (2.17)$$

## 2.3. Surface effects

The scaling hypothesis discussed in Secs. 2.1 and 2.2 considers the system in the thermodynamic limit, i.e., in the limit of infinite number of particles and infinite volume. However, in real experimental situations, no matter how large the system is, it is finite and has boundaries. These boundaries interact with the system and modify its critical behavior. Moreover, the finite size of a system adds another length scale to the system, which in addition to the bulk correlation length plays a role in the critical behavior of different thermodynamic quantities. In this section the surface effects are discussed. The finite-size effects are the focus of Sec. 2.5

Consider a semi-infinite system, i.e., a system close to a single wall. The wall lacks neighbors on one side and as a result, the interactions at the surface differ from the bulk ones. This leads to the increase or decrease of the tendency of the system to order at the wall. Such a tendency can be represented by a variable  $c$  denoting the enhancement of the surface interactions. In addition, the system can be exposed to an external surface field  $H_1$ . This field together with the surface enhancement impose boundary conditions (BCs) on the OP and modify the critical behavior of the system at the surface. The surface critical behavior is described by the fixed points of the RG transformations of  $c$  and  $H_1$ , in addition to the bulk fields. In the absence of the external surface fields the fixed points  $c = \infty, -\infty$ , and  $0$  correspond to the ordinary, extraordinary, and special transition surface universality classes, respectively<sup>5</sup>. Ordinary transition corresponds to the case, for which upon reducing temperature both surface and bulk order simultaneously [9, 53]. At the surface transition the surface orders while the bulk remains unordered. Extraordinary transition denotes the ordering of the bulk for the case that the surface is already ordered [9, 53]. All these transitions are of second-order and meet at the *special* [9, 54] or the *surface-bulk* point [9, 55, 56]. The interaction of the surface in real physical systems (like attraction of the particles to the wall) is given by an effective surface field, which induces ordering at the surface even above the critical temperature. Such a case belongs to the normal transition surface universality class, which is characterized by infinitely strong surface field and  $c = \infty$ . As discussed above, in the semi-infinite system the surface enhancement and the external surface field impose BC on the OP. The Dirichlet ( $O$ ) and (+) BCs are the ones at the RG transformation fixed points of the ordinary and normal transition surface universality classes, respectively. The ( $O$ ) BC corresponds to the vanishing OP at the surface, whereas in a continuum description (+) BC denotes infinite value of the OP at the surface [7, 9, 57].

---

<sup>5</sup>Note that the above classifications of the surface universality classes are based on the Ginzburg-Landau theory.

## 2. Theoretical background

---

Suppose that the total volume  $V$  of the system and the area  $A$  of the wall are fixed. (They are so large that the system can be considered as being semi-infinite.) The total Gibbs free energy  $G_{\text{total}}$  of the system can be decomposed as  $G_{\text{total}} = G_{\text{b}} + G_{\text{s}} = Vg_{\text{b}} + Ag_{\text{s}}$ , where  $g_{\text{b}} = G_{\text{b}}/V$  is the bulk Gibbs free energy per volume and depends on the bulk fields only, and  $g_{\text{s}} = G_{\text{s}}/A$  is the surface Gibbs free energy<sup>6</sup> per area (surface tension) and depends on the bulk and the surface fields [9]. In a similar way, in which  $G_{\text{b}}$  provides thermodynamic properties of the bulk system (see Eq. (2.3)),  $G_{\text{s}}$  provides all the thermodynamic information about the surface; the derivatives of  $G_{\text{s}}$  with respect to the surface fields provide the local quantities, whereas the derivatives of  $G_{\text{s}}$  with respect to the bulk fields provide the excess quantities [9]. These quantities follow power-laws similar to the bulk ones, however, they are governed by the surface critical exponents. For example one can define the excess specific heat as  $C_{V,s} := -T\partial^2 G_{\text{s}}/\partial T^2$  and associate the surface critical exponent  $\alpha_s$  to it as  $C_{V,s} \sim |t|^{-\alpha_s}$ . Similarly, one can define other surface critical exponents, which describe the singular part of the different physical quantities at the surface [9, 60, 61]. These surface critical exponents depend on the surface universality class of the wall and the bulk universality class of the system. Moreover, the values of surface critical exponents differ from their bulk counterparts<sup>7</sup>. However, they can be expressed via the bulk critical exponents (see Ref. [7] for example).

As discussed in Sec. 2.1, near the critical point different physical quantities exhibit a universal behavior expressed via corresponding universal scaling functions. Likewise in a semi-infinite system, near the ordinary or extraordinary transitions one can assume a scaling hypothesis for a semi-infinite system similar to the one in Eq. (2.12) and write the singular part of  $g_{\text{s}}$  as [9]

$$g_{\text{s}} \sim |t|^{2-\alpha_s} \mathcal{P}_{\pm}^s(H/|t|^{\Delta}, H_1/|t|^{\Delta_1}), \quad (2.18)$$

where the exponent  $\Delta_1$  is the surface counterpart of the bulk crossover exponent  $\Delta$ , and  $\mathcal{P}_{\pm}^s$  is the universal scaling function which is different for the ordinary and the extraordinary transitions<sup>8</sup> [9]. Note that the shape of  $\mathcal{P}_{\pm}^s$  depends not only on the bulk universality class of the system but also on the surface universality class of the wall.

The tricritical behavior of semi-infinite systems has been discussed in Refs. [62–65] and the analogs of the ordinary, extraordinary, surface, and special transitions have been reported. In a similar way to Eq. (2.18) one can generalize the tricritical scaling as in Eq. (2.14) by considering the relevant bulk and surface scaling variables.

---

<sup>6</sup>The existence of such a decomposition has been discussed in Refs. [9, 58, 59].

<sup>7</sup>In addition to the excess and local quantities, higher derivatives with respect to the combination of both the surface and the bulk fields render mixed quantities, governed by other surface critical exponents.

<sup>8</sup>At the special transition, the scaling variable  $c|t|^{-\Phi}$  with the exponent  $\Phi$  is also relevant [9].

As discussed above, in a semi-infinite system due to the interaction of the wall with the system, the particles are attracted towards the solid surface. Such an attraction might lead to the formation of liquid films on solid substrates. The next section focuses on these phenomena.

## 2.4. Wetting phenomena

Wetting phenomena refer to the formation of macroscopic films of one phase of a condensed matter, at the interface of two other phases [66]. A typical example of these phenomena is the formation of liquid wetting films on solid substrates, which might occur due to adsorption of the fluid molecules to the substrate [67]. Figure 2.1 shows the phase diagram of a simple one-component system in the pressure–temperature plane ( $P - T$ ). The solid curves denote the lines of first-order phase transitions between the corresponding phases.  $T_p$  denotes the triple point, where all three phases coexist, and  $c$  denotes the critical point of liquid–vapor phase transitions. The red point indicates an example thermodynamic state, for which a liquid like wetting film may form on a solid substrate; it depends on the surface tensions of the emerging interfaces. The surface becomes wet upon approaching the liquid–vapor coexistence if  $\sigma_{s,v} = \sigma_{s,l} + \sigma_{l,v}$ , where  $\sigma_{s,l}$  is the substrate–liquid surface tension, and  $\sigma_{s,l}$  and  $\sigma_{l,v}$  are the substrate–liquid and the liquid–vapor surface tensions, respectively. For  $\sigma_{s,v} < \sigma_{s,l} + \sigma_{l,v}$  the surface remains nonwet [66].

Figure 2.2 shows the density profile close to the surface for the case, where a liquidlike film of thickness  $\ell$  is formed for the thermodynamic state given by the red point in Fig. 2.1. (Note that this is a coarse-grained picture.) The density near the surface is close to that of the metastable liquid phase  $D_l$  at the corresponding thermodynamic state. Further away from the substrate the density decreases to the stable bulk vapor phase  $D_v$ . The densities  $D_l$  and  $D_v$  and the film thickness  $\ell$  depend on the thermodynamic state.

Typically, for the thermodynamic states of the vapor phase (like the red point in Fig. 2.1) the wetting film is finite (if formed at all). However, at the liquid–vapor coexistence line the wetting film becomes infinite above the so-called wetting temperature  $T_w$ . This raises the question: *how does a finite film grow?* Figures 2.3 and 2.4 summarize the various scenarios for the growth of the wetting film [67, 68]. In these figures the chemical potential is shown by  $\mu$ , its value at the liquid–vapor coexistence is denoted by  $\mu_0$ , whereas  $T_c$  is the critical point of the liquid–vapor phase transitions. Figs. 2.3(a) and 2.4(a) show various thermodynamic paths, along which the liquid–vapor coexistence line is approached at different temperatures. Figs. 2.3(b) and 2.4(b) show the film thickness as a function of  $\mu$  for the thermodynamic paths with the same color as in

## 2. Theoretical background

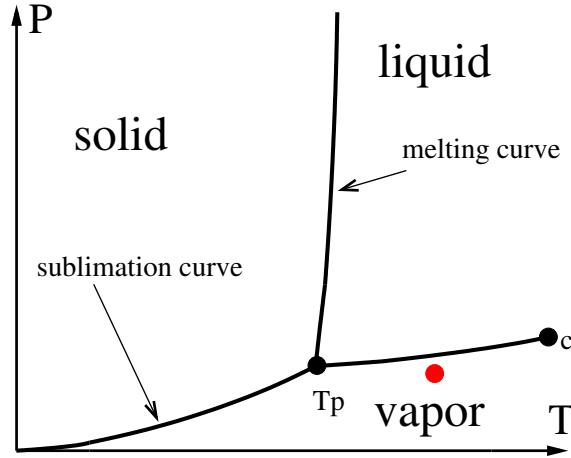


**Figure 2.1.** Phase diagram of a simple one-component system in the pressure–temperature plane ( $P - T$ ). The solid black curves denote the lines of first-order phase transitions between the corresponding phases. At the triple point  $T_p$  all three phases coexist. The line of liquid–vapor phase transitions terminates at a critical point  $c$ . The red point denotes an example thermodynamic state, at which liquid wetting films might form on solid substrates [66].

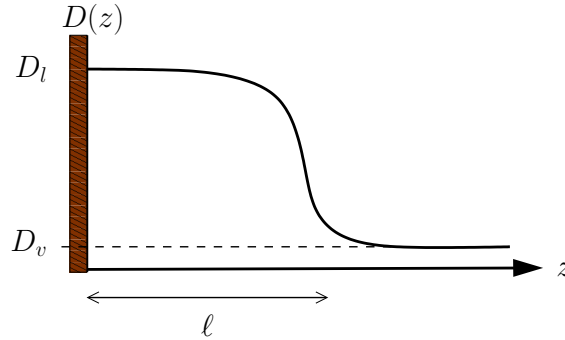


**Figure 2.2.** Density profile  $D(z)$  of the fluid near the substrate in the case of formation of a wetting film of thickness  $\ell$  for a thermodynamic state given by the red point in Fig. 2.1.  $D_l$  is close to the density of the metastable liquid phase at the thermodynamic state, at which the stable bulk phase is the vapor phase with density  $D_v$  [66].

Figs. 2.3(a) and 2.4(a). Upon approaching liquid–vapor coexistence line at  $T < T_w$  (blue dashed arrows in Figs. 2.3(a) and 2.4(a)) the film thickness remains finite (blue dashed arrows in Figs. 2.3(b) and 2.4(b)), which corresponds to the so-called *partial* or *incomplete* wetting. Upon approaching the liquid–vapor coexistence line at  $T_w < T < T_c$  (red dashed arrows in Figs. 2.3(a) and 2.4(a)) the film thickness becomes infinite (red dashed arrows in Figs. 2.3(b) and 2.4(b)); this corresponds to the so-called *complete* wetting. To figure out how the films in the partial and complete wetting regimes are transformed into each other, one chooses a thermodynamic path at the liquid–vapor

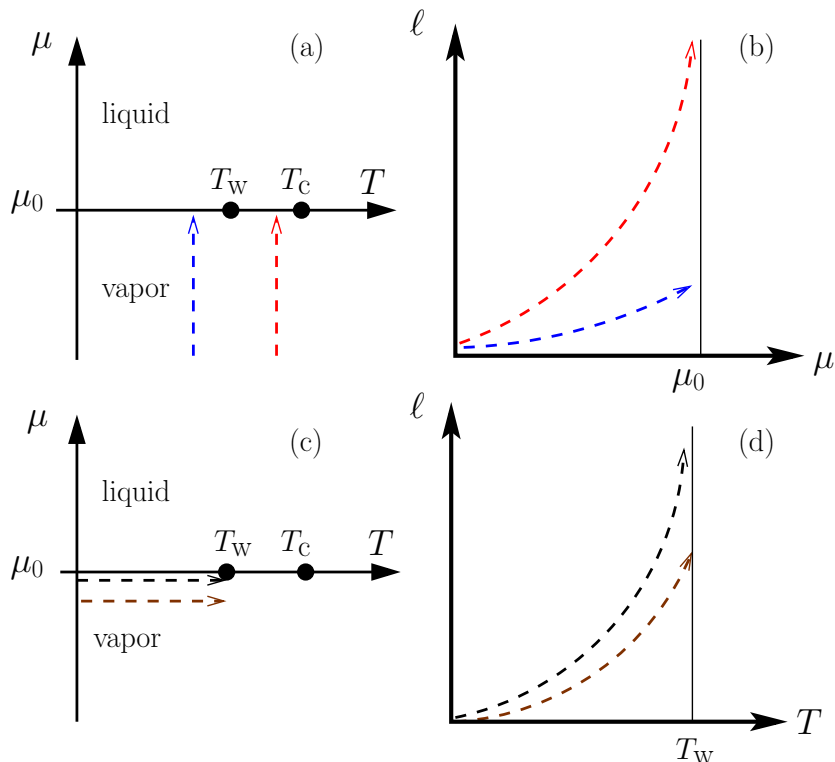


**Figure 2.3.** Different thermodynamic paths (panels (a) and (c)) and the growth of the film thickness  $\ell$  as a function of chemical potential  $\mu$  (panel (b)) and temperature  $T$  (panel (d)) along the paths in panels (a) and (c) (same color code in all panels). The wetting temperature is denoted by  $T_w$ , the critical point of the liquid–vapor phase transitions is represented by  $T_c$ .  $\mu = \mu_0$  shows the liquid–vapor coexistence line. Note that the dashed black arrow in panel (c) refers to a thermodynamic path at coexistence (i.e. at  $\mu = \mu_0$ ) however, for the sake of readability it is drawn slightly below  $\mu = \mu_0$  [66].

coexistence line (i.e., at  $\mu = \mu_0$ ) and changes  $T$ . Such thermodynamic paths are shown by the black dashed arrows in Figs. 2.3(c) and 2.4(c) (Note for the sake of readability these arrows are drawn slightly below  $\mu = \mu_0$ ). For these thermodynamic path if upon approaching  $T_w$  the thickness of the wetting film diverges continuously (black dashed arrow in Fig. 2.3(d)), then a second–order or critical wetting transition occurs. On the other hand if this growth is discontinuous, then a first–order wetting transition takes place (black dashed arrow in Fig. 2.4(d)). In the case of first–order wetting such a discontinuity occurs also for the thermodynamic paths in the vapor phase (see the thermodynamic path given by the brown dashed arrow in Fig. 2.4(c) and the growth of the film thickness given by the brown dashed arrow in Fig. 2.4(d)). The position of the jumps on the  $(\mu, T)$  plane determines the *pre-wetting* line (the curve between  $T_w$  and  $T_c$  in Fig. 2.4(c)), which terminates at a critical point  $T_c$ . Note that in both cases of first– and second–order wetting transitions, for a thermodynamic path in the vapor phase but close to the liquid–

## 2. Theoretical background

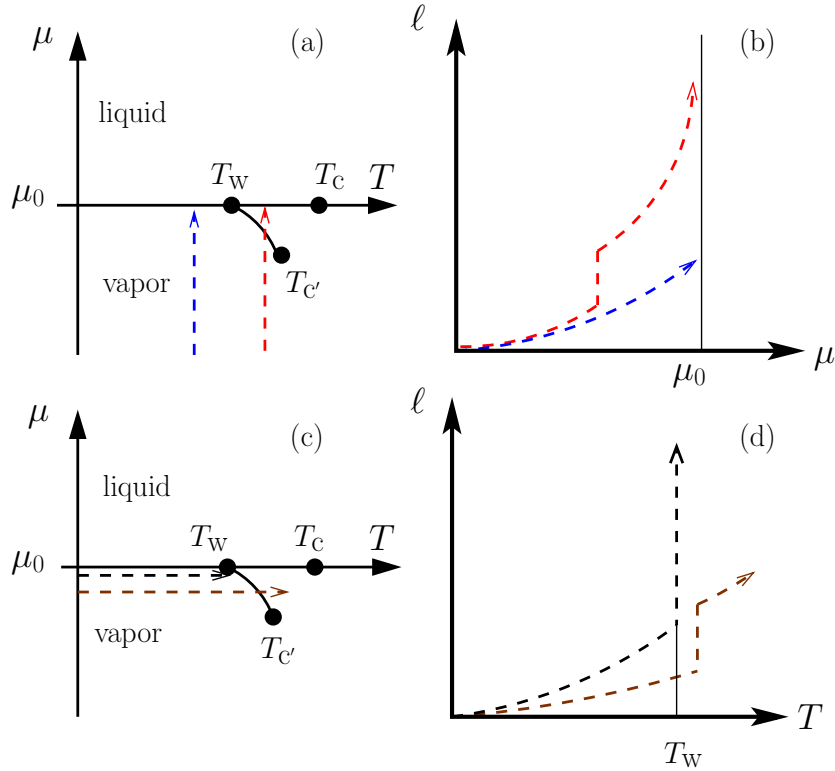


**Figure 2.4.** Same as in Fig. 2.3 but for first-order wetting transition.  $T_{c'}$  represents the critical point, at which the pre-wetting line (the line between  $T_{c'}$  and  $T_w$ ) terminates [66].

vapor coexistence line (brown dashed arrows in Figs. 2.3(c) and 2.4(c)) the film thickness does not diverge upon approaching  $T_w$  but increases to a finite value (brown dashed arrows in Figs. 2.3(d) and 2.4(d)). This finite value increases steeply upon approaching  $T_c$ . The growth of the wetting film as a function of chemical potentials depends on the range of the substrate potential and of the adsorbate–adsorbate interaction [67]. These potentials can be either short- or long-ranged. For short-ranged interactions the growth of the film thickness in the complete wetting regime is logarithmic, i.e.,  $\ell(T, \Delta\mu = \mu - \mu_0) \sim \ln(|\Delta\mu|)$ , whereas for long-ranged interactions this growth obeys the power-law  $\ell(T, \Delta\mu = \mu - \mu_0) \sim |\Delta\mu|^{-1/3}$  [69].

## 2.5. Finite-size scaling

As discussed in Sec. 2.3, the boundaries in the real experimental setups modify the bulk critical behavior of the system. On one hand side these boundaries cause surface effects, on the other hand side they limit the system. The surface effects have been explained in Sec. 2.3. In this section the finite-size effects are discussed. In finite systems the partition function is a definite sum of analytical terms. Therefore, the free energy remains finite

and the thermodynamic quantities do not have any singularities even very close to the bulk critical point. However, for very large systems with large number of particles the power-laws discussed in the previous sections will be fair approximations of the thermodynamic behavior of the system except in the close vicinity of the critical point [6]. In the following the film geometry is considered; a system composed of two parallel infinite walls at a finite distance. Since such a system is infinite in  $d - 1$  dimensions, it can still show singularities, which are however different from the bulk ones. In such systems, there is an interplay between two length scales: the bulk correlation length  $\xi$ , and the distance between the walls  $L$ . When  $L \sim \xi$  then the properties of the system become  $L$ -dependent, however if  $L \gg \xi$  the finite size effects are negligible.

One of the finite-size effects is that the critical point might be shifted to another temperature  $T_{c,L}^{(\iota)}$ , where  $(\iota)$  denotes the dependency of this shift on the type of the BCs which the two surfaces impose on the OP (see Sec. 2.3). For very large systems, the shift in the critical temperature is characterized by the shift exponent  $\lambda$  as [10]

$$\epsilon_L^{(\iota)} = \frac{T_c - T_{c,L}^{(\iota)}}{T_c} \simeq b^{(\iota)} L^{-\lambda}, \quad (2.19)$$

where  $\epsilon_L^{(\iota)}$  is the so-called fractional shift,  $T_c$  denotes the bulk critical temperature (i.e., for the infinite system), and  $b^{(\iota)}$  is the amplitude. Consider a thermodynamic quantity  $K$ , which in the bulk shows a critical behavior associated with an exponent  $\rho$  as

$$K_\infty \simeq A_\infty t^{-\rho}, \quad (2.20)$$

where  $K_\infty$  denotes the singular part of quantity  $K$  in the bulk with  $A_\infty$  being its amplitude. In the finite system upon approaching  $T_{c,L}^{(\iota)}$  the behavior of  $K$  is governed by another exponent  $\dot{\rho}$  as [10, 70]

$$K_L^{(\iota)} \simeq \dot{A}_L^{(\iota)} \dot{t}^{-\dot{\rho}}, \quad (2.21)$$

where  $K_L$  denotes the singular part of quantity  $K$  in the film geometry, with  $\dot{A}_L^{(\iota)}$  being the amplitude and

$$\dot{t} = \frac{T - T_{c,L}^{(\iota)}}{T_c}. \quad (2.22)$$

If the spatial dimension  $d \leq d_*$  (where,  $d_*$  is the lower critical dimension below which there is no bulk phase transition), the singularities of thermodynamic quantities are rounded. The rounding shows to what extent the behavior of a thermodynamic quantity in a confined system deviates from the one in the bulk. If such deviations become significant at temperature  $T_{*,L}^{(\iota)}$  then the fractional rounding  $\delta_L^{(\iota)}$ , as defined below, is

## 2. Theoretical background

---

related to  $L$  with the exponent  $\theta$  and the amplitude  $c^{(\ell)}$  as [10]

$$\delta_L^{(\ell)} = \frac{T_{*,L}^{(\ell)} - T_c}{T_c} \simeq c^{(\ell)} L^{-\theta}. \quad (2.23)$$

The two exponents  $\lambda$  and  $\theta$  describe how the behavior of a confined system approaches the infinite one as a function of the system size  $L$ . In order to relate  $\lambda$  and  $\theta$  to the bulk critical exponents, first one considers the decomposition of the total Gibbs free energy of a system within film geometry. One can assume that the total Gibbs free energy for such a system is the sum of the bulk contribution, the two surface contributions and the finite-size contribution as [6]

$$\begin{aligned} G_{\text{total}}(T, H, H_{1,(1)}, c_{(1)}, H_{1,(2)}, c_{(2)}; L) = & ALg_b(T, H) + Ag_{s,(1)}(T, H, H_{1,(1)}, c_{(1)}) \\ & + Ag_{s,(2)}(T, H, H_{1,(2)}, c_{(2)}) \\ & + Ag_{\text{excess}}(T, H, H_{1,(1)}, c_{(1)}, H_{1,(2)}, c_{(2)}; L), \end{aligned} \quad (2.24)$$

where  $H$  is the bulk magnetic field,  $g_b$  is the bulk free energy per volume  $V$ ,  $g_{s,(1)}$  and  $g_{s,(2)}$  are the surface free energy per area  $A$  at the two surfaces labeled by (1) and (2) with the surface magnetic field and the surface enhancement at the corresponding wall denoted by  $(H_{1,(1)}, c_{(1)})$  and  $(H_{1,(2)}, c_{(2)})$ , respectively, and  $g_{\text{excess}}$  is the finite-size contribution to the total Gibbs free energy<sup>9</sup>. The validity of this decomposition depends on the ratio  $\xi/L$ ; such a decomposition fails if  $L \sim \xi$  [71]. Since the temperature  $T_{*,L}^{(\ell)}$  as in Eq. (2.23) is a measure of deviations from the bulk behavior, the correlation length at this temperature provides a proper criteria for the validity of the decomposition in Eq. (2.24). This means that if  $\xi(T_{*,L}^{(\ell)}) \sim L$  then decomposing the total Gibbs free energy as in Eq. (2.24) is not valid anymore. Using Eqs. (2.9) and (2.4), the correlation length at  $T = T_{*,L}^{(\ell)}$  is [70]

$$\xi(T_{*,L}^{(\ell)}) \sim \left| \frac{T_{*,L}^{(\ell)} - T_c}{T_c} \right|^{-\nu}. \quad (2.25)$$

Now using Eqs. (2.23) and (2.25), the criteria  $\xi(T_{*,L}^{(\ell)}) \sim L$  for the validity of the decomposition in Eq. (2.24) gives

$$\theta = 1/\nu. \quad (2.26)$$

Note that this relation can also be predicted by RG analysis [70]. In a similar way, applying the criteria  $\xi \sim L$  to Eq. (2.19) renders<sup>10</sup> [70, 71]

$$\lambda = \theta = 1/\nu. \quad (2.27)$$

---

<sup>9</sup> If the BCs induce an interface in the system (for example two walls preferring different components of a binary liquid mixture) then an additional term with surface tension must be included in Eq. (2.24).

<sup>10</sup>See Ref. [70] for the validity of Eq. (2.27).

In Secs. 2.1 and 2.3 it has been discussed that near the critical point different thermodynamic quantities can be expressed in terms of dimensionless universal scaling functions of the relevant bulk and surface scaling fields. In finite systems, the scaling variable  $L/\xi$  must also be considered. The two key assumptions of finite-size scaling are [10, 70]

- (1) In a finite system near the critical point in addition to the bulk and surface scaling variables,  $L/\xi \sim L|t|^\nu$  is the relevant scaling variable
- (2) The rounding takes place when the bulk correlation length  $\xi \sim L$  (which has been discussed above)

For the thermodynamic quantity  $K$  as in Eq. (2.20) the finite-size scaling hypothesis states that<sup>11</sup>

$$K_L^{(\iota)} \sim L^w \Pi_L^{(\iota)}(L/\xi), \quad (2.28)$$

or equivalently

$$K_L^{(\iota)} \sim L^w \hat{\Pi}_L^{(\iota)}(tL^{1/\nu}) \sim L^w \bar{\Pi}_L^{(\iota)}(Lt^\nu), \quad (2.29)$$

where  $\Pi_L^{(\iota)}$ ,  $\hat{\Pi}_L^{(\iota)}$ , and  $\bar{\Pi}_L^{(\iota)}$  are dimensionless universal finite-size scaling functions, and  $w$  is the exponent relating Eq. (2.28) to Eq. (2.20) in the limit  $L \rightarrow \infty$ . In this limit Eq. (2.28) renders Eq. (2.20) if<sup>12</sup>

$$w = \varrho\theta = \varrho/\nu. \quad (2.31)$$

Note that the above finite-size scaling form is valid in the limit of vanishing other scaling fields. In general one must consider all the relevant bulk and surface scaling fields and assumes a similar scaling form as in Eq. (2.30). Accordingly, one first assumes that the Gibbs free energy is a generalized homogeneous function of  $L$  and associates specific powers of  $L$  to different scaling fields and relates these powers to the bulk and surface critical exponents by taking the limit  $L \rightarrow \infty$ .

One of the manifestations of the finite-size effects is the so-called critical Casimir effect. This is the focus of the next section.

---

<sup>11</sup>Here the other bulk and surface scaling variables are ignored.

<sup>12</sup>In a more general manner instead of  $t$  one considers the fractional temperature  $\hat{t}$  as in Eq. (2.22). Since the deviations from the bulk behavior is governed by exponent  $\theta$  as in Eq. (2.23), the finite size of the systems matters if  $\hat{t}$  becomes of the size of  $L^{-\theta}$ . The ratio  $\hat{t}/L^{-\theta} = \tilde{t}L^\theta$  is the relevant scaling variable and the finite-size scaling form of the thermodynamic quantity  $K$  reads as

$$K_L^{(\iota)} \sim L^w \tilde{\Pi}_L^{(\iota)}(\tilde{t}L^\theta), \quad (2.30)$$

where  $\tilde{\Pi}_L^{(\iota)}$  is the dimensionless universal finite-size scaling function.

### 2.6. Critical Casimir effect

In 1948 Hendrik Casimir predicted an attractive force between two parallel uncharged perfectly conducting<sup>13</sup> plates in vacuum [1]. These forces arise due to the confinement of the zero-point fluctuations of the electromagnetic field and the BCs, which the plates impose on them. The BCs restrict the allowed wavelengths between the plates so that the energy density between the plates becomes smaller than that of the outer space. This leads to an attractive force  $F$  between the two plates given by

$$F/A = -\frac{\pi^2 \hbar c}{240 L^4}, \quad (2.32)$$

where  $A$  is the area of the plates,  $L$  is the distance between them,  $\hbar$  is the reduced Planck's constant [72], and  $c$  is the velocity of light.

The analog of the Casimir effect within soft matter systems, the so-called critical Casimir effect was predicted theoretically by Fisher and de Gennes in 1978 [2] and some years later by Symanzik [3]. In soft matter systems the confinement of the critical thermal fluctuations and the modification of the OP profiles (caused by the surfaces) lead to the critical Casimir forces (CCFs) between the confining surfaces. Generally, a fluid mediated force  $F_s$  between two parallel planar walls with the surface area  $A$  and at the distance  $L$  arising from the finite-size effects is given by [5]

$$F_s = - \left( \frac{\partial(Ag_{\text{excess}})}{\partial L} \right)_{T,H,\dots} \quad (2.33)$$

where  $g_{\text{excess}}$  is the finite-size contribution to the Gibbs free energy given by Eq. (2.24), and  $T, H, \dots$  stand for all thermodynamic fields. Upon approaching the bulk critical point of the confined fluid,  $F_s$  acquires the *universal* long-ranged contribution  $F_C$  [10, 73, 74].

$$F_C = \frac{k_B T_c}{L^d} \Theta^{(\iota)}(L/\xi), \quad (2.34)$$

where  $d$  is the spatial dimension,  $k_B$  is the Boltzmann constant,  $T_c$  is the critical temperature,  $\Theta^{(\iota)}$  is the dimensionless universal finite-size scaling function,  $\xi$  is the bulk correlation length. Note that the scaling function  $\Theta^{(\iota)}$  depends on the bulk universality class of the confined fluid and on surface universality classes of the confining surfaces.

The CCF can be both attractive and repulsive; the sign of the scaling function in Eq. (2.34) depends on the type of BCs. For symmetric BCs the CCF is attractive, whereas non-symmetric BCs lead to repulsive CCF. To get an intuition about this dependency consider a binary liquid mixture confined between two surfaces, which adsorb

---

<sup>13</sup>It is enough that the penetration depth is much smaller than the distance between the plates.

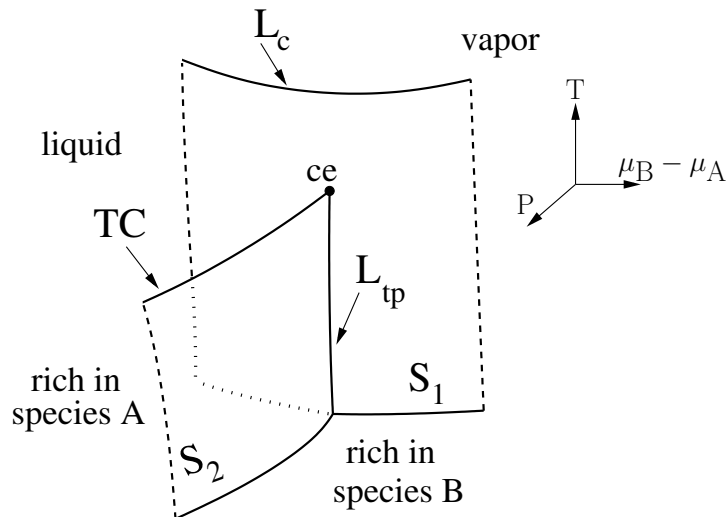


**Figure 2.5.** Schematic representation of fluid parts of the phase diagram of a classical binary liquid mixture in the  $(T, P, \mu_B - \mu_A)$  plane where,  $P$  is the pressure,  $T$  is the temperature, and  $\mu_A$  and  $\mu_B$  denote the chemical potentials of species A and B, respectively [20]. For the details see the main text.

specific species of the mixture and therefore, attract that species. As a result of this attraction, near each surface a layer with high concentration of the preferred species forms; the thickness of this layer is of the order of the correlation length. Upon approaching the critical point the bulk correlation length diverges and the effect of the surfaces on the bulk becomes more pronounced. This leads to the so-called critical adsorption [9, 75], where macroscopic layers of a phase rich in species preferred by the substrates form near them. If the two surfaces are close enough, the bulk system between them is affected by both of them. The competition between the two surfaces to dominate over the bulk leads to the effective force between them; if the two surfaces have the same preference, they tend to come closer to envelop a region with high concentration of the same preferred species (attractive CCF), whereas for different preferences the two surfaces get further from each other to form distinct regions with high concentrations of the different preferred species near themselves (repulsive CCF).

## 2.7. Wetting films and critical Casimir forces

As mentioned in Introduction, the first experimental evidences for CCFs have been provided by their effect on the equilibrium thickness of the wetting films of classical binary liquid mixtures [11–14],  $^4\text{He}$  [15, 16], and  $^3\text{He}$  -  $^4\text{He}$  mixtures [17, 18]. In this section the case of classical binary liquid mixtures is discussed. CCFs within wetting films of  $^4\text{He}$  and  $^3\text{He}$  -  $^4\text{He}$  mixtures will be explained in the next chapter.

## 2. Theoretical background

---

Figure 2.5 shows the fluid parts of the phase diagram of a classical binary liquid mixture of species A and B [20]. Therein,  $P$  is the pressure,  $T$  is the temperature, and  $\mu_A$  and  $\mu_B$  denote the chemical potentials of species A and B, respectively.  $S_1$  is the surface of first-order liquid-vapor phase transitions, whereas  $S_2$  denotes the surface of first-order liquid-liquid demixing transitions between phases rich in either species A or B. The surfaces  $S_1$  and  $S_2$  intersect along a line  $L_{tp}$  of triple points. The surface  $S_1$  terminates at a line  $L_c$  of critical points, whereas the surface  $S_2$  terminates at a line TC of critical points of liquid-liquid demixing transitions. The line TC ends at  $S_1$  at the critical end point  $ce$ .

In wetting films of classical binary liquid mixtures, the CCFs arise near the critical end point  $ce$  of the mixture [19] and originate from the restriction and modification of critical fluctuations of the composition of the mixture imposed by the solid substrate and the emerging liquid-vapor interface. The CCF together with the gravity and the omnipresent dispersion forces acts on the liquid-vapor interface and determines the equilibrium wetting film thickness [11–14]. This enables one to calculate CCF indirectly by monitoring the wetting film thickness [19, 20]. The critical point of the demixing transitions in classical binary liquid mixtures belongs to the three-dimensional Ising universality class and the OP is defined as the deviation of the difference of the concentrations of the two species from its critical value. The solid substrate on which the wetting film grows belongs to the normal transition universality class, characterized by a strong effective surface field, which describes the preference of the surface for one of the two species forming the binary liquid mixture (see Sec. 2.3). This preference results in the attraction of one of the components towards the solid substrate and therefore, effectively leads to the repelling of the other component towards the liquid-vapor interface. As a result, the two interfaces impose non-symmetric (+, -) BCs on the OP, which give rise to repulsive CCF [11–14].

## 3. Helium mixtures

In this chapter the properties of helium, and the phase diagram of  $^4\text{He}$  isotope and its mixture with  $^3\text{He}$  are reviewed briefly (Sec. 3.1). As will be discussed, liquid helium exhibits second-order phase transitions to the superfluid phase (a liquid phase without viscosity). In Sec. 3.2 a proper order parameter (OP) is introduced, which describes the superfluid transitions of  $^4\text{He}$ . Finally, in Sec. 3.3 it will be discussed how the wetting films of  $^4\text{He}$  and  $^3\text{He}$ - $^4\text{He}$  mixtures have provided evidences for critical and tricritical Casimir forces.

### 3.1. Bulk phase diagram

Helium is the simplest atom after hydrogen and is the first noble gas. It has two protons and two electrons and can appear naturally as two isotopes:  $^3\text{He}$  with one neutron and  $^4\text{He}$  with two neutrons. The helium atom is spherically symmetric. The van der Waals forces in liquid helium are weaker than in other substances and therefore, the boiling point and the critical point of the liquid-vapor phase transitions in helium are lower than in other substances [76]. The thermal energy of helium atom is also weak. Therefore, in addition to the weak thermal energy and van der Waals forces, the solidification of helium is subject to the zero-point energy<sup>1</sup>. The van der Waals forces tend to pack the molecules into a regular structure, whereas the thermal energy and the zero-point energy perturb such ordering. As a result, due to the zero-point energy down to the absolute zero the liquid remains the stable phase and one has to apply pressure to solidify helium [76].

One of the other astonishing features of helium is that it can become superfluid; a liquid phase with zero viscosity. The discovery of the superfluidity started with the observations of some unusual properties of liquid  $^4\text{He}$ . In 1911 Kamerlingh Onnes used

---

Parts of this chapter are reprinted with permission from [N. Farahmand Bafi, A. Maciołek, and S. Dietrich, *Phys. Rev. E* **95**, 032802 (2017).] Copyright 2017 by the American Physical Society and [N. Farahmand Bafi, A. Maciołek, and S. Dietrich, *Phys. Rev. E* **91**, 022138 (2015).] Copyright 2015 by the American Physical Society.

<sup>1</sup>The zero-point energy is the lowest energy of a quantum system.

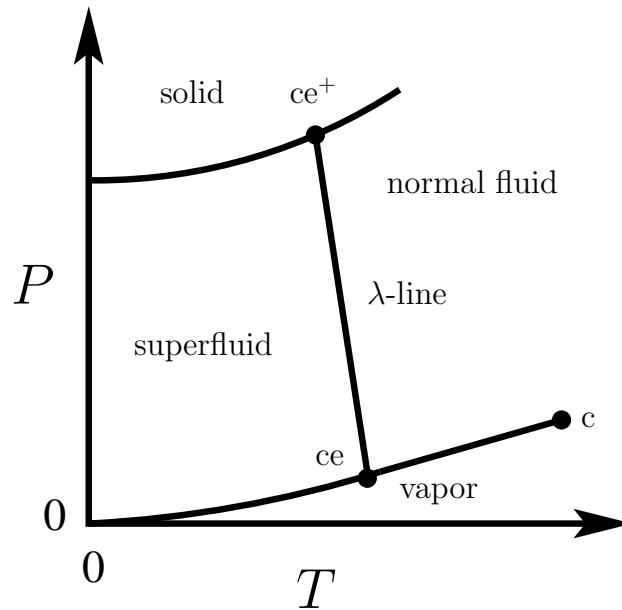


**Figure 3.1.** Schematic bulk phase diagram of  ${}^4\text{He}$  in the pressure–temperature plane  $(P, T)$  exhibiting the vapor, superfluid, normal fluid, and solid phases. The liquid–vapor critical point is denoted by  $c$ , whereas  $ce^+$  and  $ce$  are critical end points. The  $\lambda$ -line is the line of second–order phase transitions between the superfluid and the normal fluid. The liquid remains the stable phase down to absolute zero and one has to apply pressure to solidify  ${}^4\text{He}$  [20, 87].

liquid  ${}^4\text{He}$  as coolant for studying the resistivity of mercury at low temperatures [77, 78]. In his experiments he noticed that at low enough temperatures  ${}^4\text{He}$  stops boiling [78, 79]. In 1927 Keesom and Wolfke reported a sudden jump in their measurements of the dielectric constant in liquid  ${}^4\text{He}$  at temperature  $T = 2.17\text{ K}$  [78, 80, 81]. This was followed by the observation of the anomaly in the heat capacity  $C$  of  ${}^4\text{He}$  by Clusius near the same temperature [78, 82, 83]. Due to the shape of the behavior of the heat capacity  $C$  as a function of temperature  $T$  around  $T = 2.17\text{ K}$  the transition received its famous name, the  $\lambda$ -point [78]. Later in 1935 Burton reported a drop of almost an order of magnitude in viscosity coefficient of  ${}^4\text{He}$  around the  $\lambda$ -point [78, 84]. This was followed by two similar reports on the flow of  ${}^4\text{He}$  through narrow slit [78, 85] and narrow capillary [78, 86]. Following these observations, by analogy to superconductors this special state was given the name *superfluid* [78, 85]. The temperature  $T$  of the superfluid transition in  ${}^4\text{He}$  depends on the pressure  $P$ . Accordingly, in the  $(P, T)$  plane the superfluid and normal fluid phases are separated by a line of second–order phase transitions, the so-called  $\lambda$ -line (see Fig. 3.1) [87].

The theoretical explanation of the  $\lambda$ -transition dates back to 1938 [78, 88, 89], when London associated the superfluid transition in  ${}^4\text{He}$  with the Bose–Einstein condensation

(BEC) [78, 90–92]. In the Bose–Einstein condensate, a macroscopic number of atoms occupy the lowest quantum energy level at which the atoms have small momentum. This corresponds to large values of the de Broglie wave length, for which the wave functions of the individual atoms span over large distances and are not distinguishable from each other anymore. As a result, all atoms behave as a whole and one single wave function describes their behavior. Although London foresees BEC as the phenomenon being relevant to all anomalous properties of helium, he does not mention the superfluidity. The unusual dynamics of  $^4\text{He}$  was later addressed theoretically by Tisza [78, 93]. Associating the superfluidity to BEC, he proposed that the atoms in the lowest energy level exhibit superfluid behavior, whereas the atoms in the excited states cause the friction [78]. In 1941, Landau reported a criticism to Tisza’s idea, saying that even in an ideal Bose gas the collision of atoms and therefore the friction between them would be unavoidable [78, 94]. Instead, he proposed a two–fluid model, which assumes that below the  $\lambda$ -transition  $^4\text{He}$  can be regarded as a mixture of two liquids types; a superfluid with no viscosity and a normal fluid. The two–fluid model does not explain the reason for the superfluid transition. However, based on the two–fluid picture of  $^4\text{He}$ , the model explains the other anomalies in the properties of  $^4\text{He}$ . The connection between BEC and superfluidity was addressed in 1951, when Penrose reported that in certain cases the two–fluid picture of  $^4\text{He}$  would also follow from a quantum mechanical description of a system of identical interacting particles [78, 95]. He showed that if the probability of a particle having large de Broglie wavelength (i.e., having a negligible momentum) is finite—which is satisfied in Bose–Einstein condensate—then a new velocity field overtakes the velocity of a normal fluid<sup>2</sup>.

The other helium isotope ( $^3\text{He}$ ) becomes superfluid as well [76]. Although  $^4\text{He}$  is boson and its superfluidity is related<sup>3</sup> to BEC,  $^3\text{He}$  is fermion and its superfluid transition is due to the formation of cooper pairs, which act like bosons [76]. The superfluid transition of  $^3\text{He}$  occurs at much lower temperatures<sup>4</sup> than that of  $^4\text{He}$  and for the temperature range of the  $\lambda$ -transitions in  $^4\text{He}$ ,  $^3\text{He}$  remains normal fluid. This provides the opportunity to build a unique binary liquid mixture; a mixture of  $^4\text{He}$  which can become superfluid and  $^3\text{He}$  which remains normal fluid within the proper temperature range.

Figure 3.2 shows the schematic phase diagram of  $^3\text{He}$ - $^4\text{He}$  mixtures at fixed pressure

---

<sup>2</sup>Further developments of the theory of superfluidity was done by Onsager, Penrose and others [78], discussing of which is out of the focus of the present thesis.

<sup>3</sup>For the relevance of BEC to superfluidity see Ref. [78].

<sup>4</sup>The low temperature superfluid transition in  $^3\text{He}$  (around 2.6 mK) has made the experimental conditions more difficult to achieve. Therefore, the study of the superfluid transitions in  $^3\text{He}$  has been postponed to more recent times. Among these experiments are the specific heat measurements by Greywall [96] in 1983 and the viscosity measurements by Parpia et al. [97] in 1978 [76].

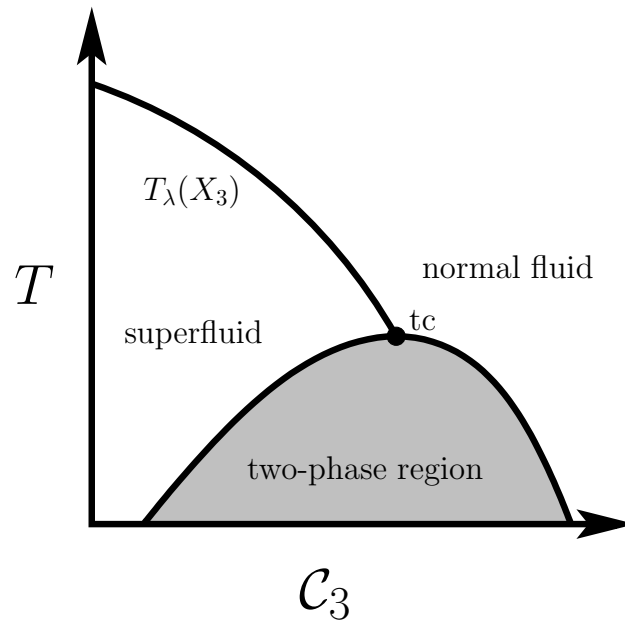


**Figure 3.2.** Schematic bulk phase diagram of  ${}^3\text{He}$ - ${}^4\text{He}$  mixtures at fixed pressure.  $\mathcal{C}_3$  is the concentration of  ${}^3\text{He}$  and  $T_\lambda(\mathcal{C}_3)$  is the line of second-order superfluid transitions, which turn into first-order superfluid transitions at the tricritical point  $t_c$ . Note that  $T_\lambda(\mathcal{C}_3)$  meets the two-phase region at its top. If  $T_\lambda(\mathcal{C}_3)$  met the two-phase region below  $T_{t_c}$ , this would imply that there is a first-order phase transition either between two normal fluid phases or between two superfluid phases, which is not the case [20, 76, 98, 99].

in the  $(T, \mathcal{C}_3)$  plane, where  $T$  denotes the temperature and  $\mathcal{C}_3$  is the concentrations of  ${}^3\text{He}$  [76, 98, 99]. Adding  ${}^3\text{He}$  atoms to the pure  ${}^4\text{He}$  liquid, dilutes the  ${}^4\text{He}$  carriers of superfluidity and thus lowers the critical temperature of the superfluid transition of  ${}^4\text{He}$  atoms [76]. Accordingly, the transition temperature  $T_\lambda$  of the second-order phase transition to the superfluid phase depends on the concentration  $\mathcal{C}_3$  of  ${}^3\text{He}$  atoms. Beyond a certain dilution due to  ${}^3\text{He}$  atoms the superfluid transition turns into a first-order phase transition [76], which is accompanied by a two-phase region; this change occurs at a tricritical point  $t_c$ . The schematic phase diagram of  ${}^3\text{He}$ - ${}^4\text{He}$  mixtures in the  $(T, Z, P)$  space, where  $Z$  is the fugacity of  ${}^3\text{He}$ , is shown in Fig. 3.3 (see the figure caption for the definition of  $Z$ ) [20]. In the plane  $Z = 0$ , i.e., in the case of pure  ${}^4\text{He}$ , the phase diagram is the same as the one in Fig. 3.1. The surfaces  $A_1$  and  $A_2$  are the surfaces of first-order solid-liquid and vapor-liquid phase transitions, respectively. The surfaces  $A_3$  and  $A_4$  are the surfaces of second- and first-order phase transitions between the superfluid and the normal fluid, respectively. The surfaces  $A_3$  and  $A_4$  are separated by a line TC of tricritical points, which terminates at the tricritical end points  $tce^+$  and  $tce$ . The points  $tce^+$  and  $ce^+$  as well as  $tce$  and  $ce$  are connected by lines of critical end points on  $A_1$  and  $A_2$ , respectively. The surface  $A_4$  intersects the surfaces  $A_1$  and  $A_2$  along triple lines

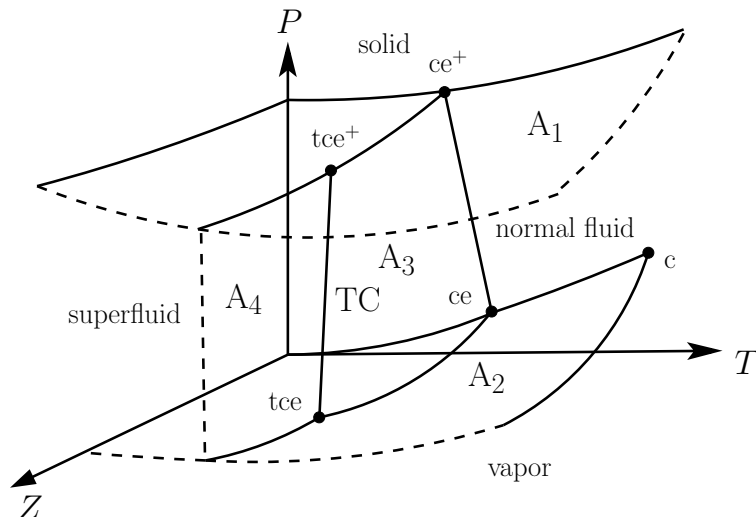


**Figure 3.3.** Schematic phase diagram of  ${}^3\text{He}$ - ${}^4\text{He}$  mixtures in the  $(T, Z, P)$  space, where  $Z = \exp(\mu_3/T)$  is the fugacity of  ${}^3\text{He}$  ( $\mu_3$  is the chemical potential of  ${}^3\text{He}$  atoms) and  $P$  is the pressure. The surfaces  $A_1$  and  $A_2$  are the surfaces of the first-order solid-liquid and vapor-liquid phase transitions, respectively, whereas  $A_3$  and  $A_4$  are the surfaces of second- and first-order phase transitions between the normal fluid and the superfluid, respectively. The surface  $A_3$  intersects  $A_1$  and  $A_2$  along a line of critical end points connecting  $ce^+$  with  $tce^+$  and  $ce$  with  $tce$ , respectively. The surfaces  $A_3$  and  $A_4$  are separated by a line TC of tricritical points, which meets  $A_1$  and  $A_2$  at the tricritical end points  $tce^+$  and  $tce$ , respectively. The surface  $A_2$  terminates at a line of critical points, starting from  $c$  in the plane  $Z = 0$ . The phase diagram in the plane  $Z = 0$  is the same as the one in Fig. 3.1. The dashed lines have no physical meaning; they indicate that the corresponding surface continues [20].

of three-phase coexistence between the solid and the two liquid phases, and the vapor and the two liquid phases, respectively.

The phase diagram in Fig. 3.2 corresponds to a specific cut (e.g. constant pressure or constant total density) of the phase diagram in Fig. 3.3; different cuts result in phase diagrams, which differ quantitatively from each other but share the same topology as in Fig. 3.2. The liquid-liquid phase transitions at coexistence with the vapor phase exhibit a phase diagram similar to the one in Fig. 3.2 as well. However, in this case the tricritical point is replaced by the tricritical end point  $tce$ .

## 3.2. Superfluid order parameter

The superfluid phase of  ${}^4\text{He}$  is related<sup>5</sup> to the BEC [4]; it is described by a wave function, which gives the probability distribution of finding  ${}^4\text{He}$  in the Bose Einstein

<sup>5</sup>See Ref. [78] for the relevance of BEC to superfluidity.

### 3. Helium mixtures

---

condensate and therefore in the superfluid phase [4]. Since the wave function is defined over the complex domain, the superfluid phase transitions of  $^4\text{He}$ , can be described via a two dimensional real valued order parameter  $\vec{M}$ . As a result, these transitions belong to the bulk  $XY$  universality class. As will be shown in chapter 4, the direction of  $\vec{M}$  is irrelevant in the mean field description of the superfluid phase;  $|\vec{M}| \neq 0$  denotes the superfluid, whereas  $|\vec{M}| = 0$  corresponds to the normal fluid<sup>6</sup>. In Sec. 2.1 it has been discussed how near the critical point of second-order phase transitions the singular part of the thermodynamic quantities are described via dimensionless universal scaling functions. This holds for the behavior of different thermodynamic quantities near the superfluid transitions as well. As illustrated in Fig. 3.1, for pure  $^4\text{He}$  the  $\lambda$ -line is described by the values of the thermodynamic fields  $P$  and  $T$ ; both of these fields are relevant in the scaling description around the  $\lambda$ -line. For the superfluid transitions in  $^3\text{He}$ - $^4\text{He}$  mixtures the situation is more complicated. First of all, a thermodynamic state in the phase diagram in Fig. 3.3 is described by three fields  $(P, T, Z)$  which are all relevant in the scaling description near the surface of second-order superfluid transitions (i.e., the surface  $A_3$  in Fig. 3.3). Secondly, the superfluid transitions turn from second-order into first-order along the line TC of tricritical points and close to this line one must assume a tricritical scaling like the one discussed in Sec. 2.2 with the tricritical exponents.

### 3.3. Helium wetting films

As discussed in Sec. 2.7, experimental studies of wetting films of critical fluids have provided convincing evidences for critical Casimir forces (CCFs). These effects occur near the critical end point of the liquid mixtures (see Sec. 2.7). The phase diagram of  $^4\text{He}$  exhibits a line of critical points, which ends at the vapor phase at a critical end point (see Sec. 3.1). This provides a situations similar to the one discussed in Sec. 2.7 and enables one to study CCF within wetting films of  $^4\text{He}$ . In these wetting films [15], the CCF originates from the confined critical fluctuations associated with the superfluid transition in the fluid film. Capacitance measurements<sup>7</sup> of the equilibrium

---

<sup>6</sup>Note that in contrast to the magnetic field  $H$ , which couples to the OP in the ferromagnetic system, the ordering field conjugate to the superfluid OP is not physical. The phase diagram of  $^3\text{He}$ - $^4\text{He}$  mixtures in the presence of such an imaginary ordering field has been studied in Ref. [46].

<sup>7</sup>In these measurements first a wetting film of helium has been formed on the plates of a capacitor. Then, based on the difference in the dielectric constants of the vapor and the film, by measuring the capacitance and relating it to the dielectric constants, the film thickness has been determined in an indirect way [15].

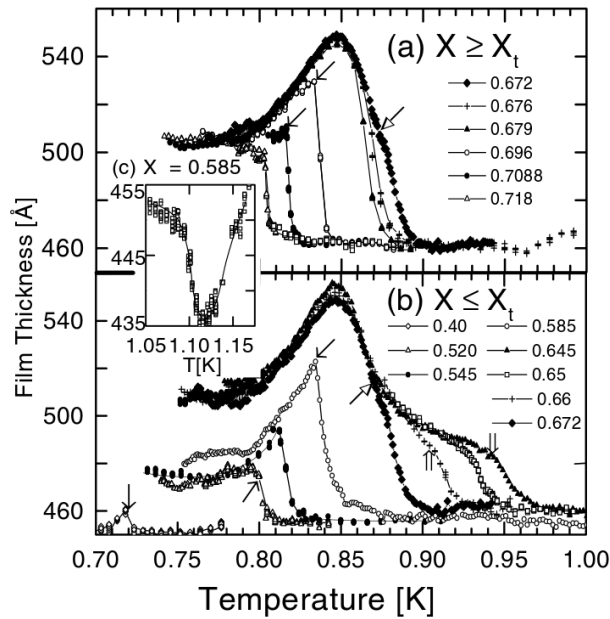


**Figure 3.4.** Experimental results of Ref. [17] for the film thickness measurements in  $^3\text{He}$ - $^4\text{He}$  wetting films. For the details see the main text. Reprinted figure with permission from Ref. [17] Copyright 2002 by the American Physical Society.

thickness of  $^4\text{He}$  complete wetting films<sup>8</sup> of the equilibrium thickness of  $^4\text{He}$  wetting films provided evidence for an attractive CCF [15,16]. These results are in agreement with the theoretical predictions [20–22] for the corresponding bulk  $XY$  universality class with symmetric Dirichlet–Dirichlet BCs ( $O, O$ ). These BCs correspond to the vanishing of the superfluid OP with  $O(2)$  symmetry at both the surface of the substrate and at the liquid–vapor interface.

Similar measurements [17] for wetting films of  $^3\text{He}$ - $^4\text{He}$  mixture performed near the tricritical end point indicated that tricritical Casimir force (TCF) is repulsive, which suggests non-symmetric BCs for the superfluid OP. Since there is no field coupled to the superfluid OP the mechanism which can possibly create such BCs is as follows [17]:  $^3\text{He}$  is lighter than  $^4\text{He}$  and experiences a larger zero–point motion. Hence, it occupies a larger volume than  $^4\text{He}$  and therefore  $^3\text{He}$  atoms are effectively expelled from the

<sup>8</sup>Experiments have shown that  $^3\text{He}$  in the temperature range where it is a normal Fermi–liquid wets graphite [67, 100–102] and platinum [67, 102] incompletely. Several experiments have shown that superfluid  $^4\text{He}$  also wets graphite incompletely [67, 103–106]. However, more recent experiments [67, 102] have shown that below  $\lambda$ -transition temperature  $^4\text{He}$  wets graphite completely. In the case of  $^3\text{He}$ - $^4\text{He}$  mixtures, considering the liquid–vapor interface the wetting film, forming upon approaching the liquid–vapor coexistence, is complete [67, 107]. Moreover, experiments [67, 108] have shown that for specific molar concentrations of  $^3\text{He}$  upon approaching the two–phase region from the normal fluid side the superfluid  $^4\text{He}$ -rich phase wets a glass substrate completely.

### 3. Helium mixtures

---

rigid solid substrate; they tend to gather at the soft liquid–vapor interface. As a result,  $^4\text{He}$  atoms are effectively attracted to the solid substrate so that a  $^4\text{He}$ -rich layer forms near the substrate–liquid interface. Due to the increased  $^4\text{He}$  concentration, this layer may become superfluid at temperatures already above the line of onset of superfluidity in the bulk [33]. leading to the symmetry breaking (+) BCs at the solid substrate. On the other hand at the liquid–vapor phase due to the low concentrations of  $^4\text{He}$  the superfluid OP remains zero leading to Dirichlet ( $O$ ) BCs. Thus the two interfaces impose non-symmetric BCs on the superfluid OP, which is merely due to the nontrivial concentration profile across the film.

Figure 3.4 shows the experimental data for the thickness measurements of  $^3\text{He}$ - $^4\text{He}$  wetting films as function of temperature [17]. The values of  $X$  refer to various concentrations of  $^3\text{He}$ . The concentration of  $^3\text{He}$  at the tricritical point is  $X_t = 0.672$ . Panels (a) and (b) corresponds to  $X \geq X_t$  and  $X \leq X_t$ , respectively. Thin arrows show the points, where the bulk liquid phase separates. The large headed arrow indicates the tricritical point. In panel (b) the arrows with double lines indicate the onset temperature of superfluidity. For the thermodynamic path on the superfluid side (panel (b)), the growth of the film thickness exhibits a characteristic shoulder between the tricritical temperature and the superfluid transition temperature on the  $\lambda$ -line. Along these thermodynamic paths in addition to the attractive TCF near the tricritical point, the wetting film is influenced by the attractive critical Casimir force close to the  $\lambda$ -transition temperature; this gives rise to the increase of the film thickness at two different temperatures and thus to the formation of the characteristic shoulder in the curves in panel (b). The growth of the film thickness as a function of temperature is due to repulsive TCFs between the solid wall and the liquid–vapor interface, arising near the tricritical point. For small values of  $X$  the wetting film resembles a film of pure  $^4\text{He}$ , in which case ( $O, O$ ) BCs are imposed on the superfluid OP. Like in the case of pure  $^4\text{He}$  films [15] these symmetric BCs lead to an attractive CCF arising near the  $\lambda$ -transitions, which causes a decrease in the wetting film thickness as shown in panel (c) [17].

## 4. Phase diagram of fluid phases in $^3\text{He}$ - $^4\text{He}$ mixtures

As discussed in Introduction the goal of the present thesis is to provide a more realistic theoretical description of tricritical Casimir forces in  $^3\text{He}$  -  $^4\text{He}$  wetting films. The first step towards such a description is to introduce a model, which allows for the occurrence of vapor phase and exhibits a bulk phase diagram, resembling the topology like the one of the actual  $^3\text{He}$  -  $^4\text{He}$  mixtures. This is the focus of the present chapter. Here the phase diagram of fluid phases in  $^3\text{He}$  -  $^4\text{He}$  mixtures are obtained by mean field analysis of a proper lattice gas model. Such a model was first introduced by Blume, Emery, and Griffiths (called the BEG model) and was used to for describing the phase diagram of  $^3\text{He}$  -  $^4\text{He}$  mixtures near the tricritical point [34]. In this classical spin-1 model, the superfluid order parameter (OP) is mimicked by two discrete values; the remaining possible value for the state variable indicates whether a lattice site is occupied by a  $^3\text{He}$  atom instead of a  $^4\text{He}$  atom. Since this interpretation of the spin-1 model does not allow for vacancies, it does not exhibit a vapor phase. Furthermore, due to the discrete values assigned to the superfluid OP, this model does not capture the actual complex character of the superfluid OP, which belongs to the  $XY$  universality class (see Sec. 3.2). Another interpretation of the BEG model is to allow for vacant sites in a *classical* binary liquid mixture of species A and B, which leads to the formation of an A-rich liquid, a B-rich liquid, a mixed fluid phase, and a vapor phase. Such a model has been used to study the condensation and the phase separation in binary liquid mixtures [109–111]. The reduced phase diagrams of ternary mixtures have also been studied within this model [112].

An improvement of the description of the superfluid transitions has been achieved by enriching the classical spin-1/2 model by a continuous value for the superfluid OP. Such a model with  $O(2)$  symmetry of the superfluid OP, is given by the so-called, vectorized BEG (VBEG) model which has been proposed and studied in two dimensions ( $d = 2$ ) by Cardy and Scalapino [36] and, independently, by Berker and Nelson [35]. More recently it has been investigated in  $d = 3$  within mean field theory and by Monte Carlo

---

This chapter is reprinted with permission from [N. Farahmand Bafi, A. Maciolek, and S. Dietrich, Phys. Rev. E **91**, 022138 (2015).] Copyright 2015 by the American Physical Society.

## 4. Phase diagram of fluid phases in ${}^3\text{He}$ - ${}^4\text{He}$ mixtures

---

simulations [113]. In this model the lattice sites are occupied either by  ${}^3\text{He}$  or  ${}^4\text{He}$  (indicated by the two values of the state variable). Since this model does not allow for vacant sites it does not exhibit a vapor phase.

In this chapter a classical spin-1 model is proposed, which allows for vacant sites in addition to the ones occupied by  ${}^3\text{He}$  or  ${}^4\text{He}$ . This enables the model to exhibit a vapor phase if the number of vacant sites is sufficiently large. Moreover, the model includes another state variable, which accounts for the continuous  $O(2)$  symmetry of the superfluid OP. In the next two sections the model is introduced (Sec. 4.1) and mean field approximation is carried out on it (Sec. 4.2). In Sec. 4.3 the various features of the phase diagram are obtained and the range of parameters are specified for which the phase diagrams have the topology corresponding to the one of the actual  ${}^3\text{He}$  -  ${}^4\text{He}$  mixture.

### 4.1. The model

In order to model the  ${}^3\text{He}$  -  ${}^4\text{He}$  mixtures let us consider a three-dimensional ( $d = 3$ ) simple cubic lattice with lattice spacing  $a = 1$ , where the lattice sites  $\{i \mid i = 1, \dots, \mathcal{N}\}$  are occupied by either  ${}^3\text{He}$  or  ${}^4\text{He}$  or they are unoccupied. The Hamiltonian of this system is

$$\begin{aligned} \mathcal{H} = & -J_{44}N_{44} - J_{33}N_{33} - J_{34}N_{34} \\ & - \mu_4N_4 - \mu_3N_3 - J_s\tilde{N}_{44} - \mathbf{H} \cdot \tilde{\mathbf{N}}_4, \end{aligned} \quad (4.1)$$

where  $N_{mn}$ , with  $m, n \in \{3, 4\}$ , denotes the number of pairs of nearest neighbors of species  $m$  and  $n$  on the lattice sites,  $N_m$  denotes the number of atoms of species  $m$ , and  $-J_s\tilde{N}_{44}$  denotes the sum of the interaction energy between the superfluid degrees of freedom  $\Theta_i$  and  $\Theta_j$  associated with the nearest-neighbor pairs  $\langle i, j \rangle$  of  ${}^4\text{He}$  with  $J_s$  as the corresponding interaction strength.  $\mathbf{H} = (H_x, H_y)$  is the field conjugate to the superfluid degrees of freedom given by the vector  $(\cos \Theta_i, \sin \Theta_i)$ , provided that the lattice site  $i$  is occupied by a  ${}^4\text{He}$  atom (note that this field is physically inaccessible and  $|\mathbf{H}| = 0$  describes the actual experimental situation).  $J_{33}$ ,  $J_{44}$ , and  $J_{34}$  describe the effective interactions between the three types of pairs of He isotopes. The  ${}^3\text{He}$  -  ${}^3\text{He}$  and  ${}^4\text{He}$  -  ${}^4\text{He}$  pair potentials between the isotopes are not quite the same due to the slight differences in their electronic states. Moreover, the corresponding effective interactions differ due to the distinct statistics of the two isotopes.  $\mu_m$  denotes the chemical potential of species  $m$ . (In  ${}^3\text{He}$  -  ${}^4\text{He}$  mixtures treated as a mixture of ideal Bose and Fermi gases the phase transition to the superfluid phase depends only on the concentration of  ${}^4\text{He}$  atoms. In the present model this is captured by the last two terms in Eq. (4.1). However, a refined

theory such as the present one takes into account that the exchange interactions between the three possible pairs of helium isotopes affect the concentrations of the two species and thus implicitly influence the phase transition to the superfluid phase.)

In order to proceed, one can express  $N_m$  and  $N_{mn}$  in terms of occupation numbers of the lattice sites  $\{i\}$ . One associates with each lattice site  $i$  an occupation variable  $s_i$  which can take the three values  $+1$ ,  $-1$ , or  $0$ , where  $+1$  means that the lattice site is occupied by  $^4\text{He}$ ,  $-1$  means the lattice site is occupied by  $^3\text{He}$ , and  $0$  means the lattice site is unoccupied. Accordingly one has

$$\begin{aligned}
 N_4 &= \frac{1}{2} \sum_i s_i(s_i + 1) \equiv \sum_i p_i, \\
 N_3 &= \frac{1}{2} \sum_i s_i(s_i - 1), \\
 N_{44} &= \frac{1}{4} \sum_{\langle i,j \rangle} (s_i(s_i + 1)s_j(s_j + 1)) \equiv \sum_{\langle i,j \rangle} p_i p_j, \\
 N_{33} &= \frac{1}{4} \sum_{\langle i,j \rangle} (s_i(s_i - 1)s_j(s_j - 1)), \\
 N_{34} &= \frac{1}{4} \sum_{\langle i,j \rangle} (s_i(s_i + 1)s_j(s_j - 1) + s_i(s_i - 1)s_j(s_j + 1)),
 \end{aligned} \tag{4.2}$$

where  $\sum_{\langle i,j \rangle}$  denotes the sum over nearest neighbors. Using the above definitions one obtains

$$\begin{aligned}
 \mathcal{H} &= -K \sum_{\langle i,j \rangle} s_i s_j - J \sum_{\langle i,j \rangle} q_i q_j - C \sum_{\langle i,j \rangle} (s_i q_j + q_i s_j) \\
 &\quad - \mu_- \sum_i s_i - \mu_+ \sum_i q_i - J_s \sum_{\langle i,j \rangle} p_i p_j \cos(\Theta_i - \Theta_j) \\
 &\quad - H_x \sum_i p_i \cos \Theta_i - H_y \sum_i p_i \sin \Theta_i,
 \end{aligned} \tag{4.3}$$

where

$$\begin{aligned}
 \sum_{\langle i,j \rangle} p_i p_j \cos(\Theta_i - \Theta_j) &= \tilde{N}_{44} = \sum_{\langle i,j \rangle} p_i p_j \begin{pmatrix} \cos \Theta_i \\ \sin \Theta_i \end{pmatrix} \cdot \begin{pmatrix} \cos \Theta_j \\ \sin \Theta_j \end{pmatrix}, \\
 \sum_i p_i (\cos \Theta_i, \sin \Theta_i) &= \tilde{\mathbf{N}}_4,
 \end{aligned} \tag{4.4}$$

and

$$\begin{aligned}
 q_i &= s_i^2, \\
 p_i &= \frac{1}{2}s_i(s_i + 1), \\
 K &= \frac{1}{4}(J_{44} + J_{33} - 2J_{34}), \\
 J &= \frac{1}{4}(J_{44} + J_{33} + 2J_{34}), \\
 C &= \frac{1}{4}(J_{44} - J_{33}), \\
 \mu_- &= \frac{1}{2}(\mu_4 - \mu_3), \\
 \mu_+ &= \frac{1}{2}(\mu_4 + \mu_3),
 \end{aligned} \tag{4.5}$$

and  $\Theta_i \in [0, 2\pi]$  represents the superfluid degree of freedom at the lattice site  $i$ , provided it is occupied by  $^4\text{He}$ .

### 4.2. Mean field approximation

In this section mean field approximation is applied to the above model. This approximation follows from a variational method based upon approximating the total equilibrium density matrix by a product of density matrices associated with each lattice site [114].

Due to the variation principle, the free energy  $F$  obeys the following inequality:

$$F \leq \phi = \hat{\text{Tr}}(\rho \mathcal{H}) + (1/\beta)\hat{\text{Tr}}(\rho \ln \rho), \tag{4.6}$$

where  $\rho$  is any trial density matrix with  $\hat{\text{Tr}}(\rho) = 1$ , with respect to which  $\phi$  on the right hand side of Eq. (4.6) should be minimized in order to obtain the best approximation;

$$\hat{\text{Tr}} = \sum_{s_1=\pm 1,0} \int_0^{2\pi} d\Theta_1 \cdot \dots \cdot \sum_{s_N=\pm 1,0} \int_0^{2\pi} d\Theta_N \tag{4.7}$$

denotes the trace and  $\beta = 1/T$  where  $T$  is the temperature times  $k_B$ . The mean field approximation assumes that any lattice site experiences the same mean field generated by its neighborhood so that the total density matrix will be the product of the density matrices corresponding to each lattice site:

$$\rho = \prod_i \rho_i, \tag{4.8}$$

with

$$\text{Tr} \rho_i = \sum_{s_i=\pm 1,0} \int_0^{2\pi} d\Theta_i \rho_i(s_i, \Theta_i) = 1. \quad (4.9)$$

For homogeneous bulk systems the local density matrix is independent of the site.

The variational mean field free energy per site for the Hamiltonian introduced in the previous section is (with  $\cos(\Theta_i - \Theta_j) = \cos \Theta_i \cos \Theta_j + \sin \Theta_i \sin \Theta_j$ )

$$\begin{aligned} \frac{\phi}{\mathcal{N}} = & -\frac{z}{2}[K\langle s_i \rangle^2 + J\langle q_i \rangle^2 + 2C\langle q_i \rangle\langle s_i \rangle \\ & + J_s(\langle p_i \cos \Theta_i \rangle^2 + \langle p_i \sin \Theta_i \rangle^2)] \\ & - \mu_- \langle s_i \rangle - \mu_+ \langle q_i \rangle - H_x \langle p_i \cos \Theta_i \rangle - H_y \langle p_i \sin \Theta_i \rangle \\ & + (1/\beta)\text{Tr}(\rho_i \ln \rho_i), \end{aligned} \quad (4.10)$$

where  $\mathcal{N}$  is the total number of sites and  $z$  is the coordination number of the lattice ( $z = 2d$ , where  $d$  is the spatial dimension of the system; here  $z = 6$ ), and  $\langle \dots \rangle = \text{Tr}(\rho_i \dots)$  denotes the thermal average, taken with the trial density matrix  $\rho_i$  associated with the lattice site  $i$ .

Minimizing the variational function  $\phi/\mathcal{N}$  with respect to  $\rho_i$  renders the best normalized functional form of  $\rho_i$ . There are two approaches to find the variational minima. In the first approach one parametrizes the density matrix  $\rho_i$  in terms of the OPs of the phase transitions and minimizes  $\phi/\mathcal{N}$  with respect to the coefficients multiplying these OPs. In the second approach one treats  $\rho$  itself as a variational function and minimizes  $\phi/\mathcal{N}$  with respect to it [114]. Let us follow the second approach and calculate the functional derivative of  $\phi/\mathcal{N}$  in Eq. (4.10) with respect to  $\rho_i(s_i, \Theta_i)$  using  $\frac{\delta \rho_i(s_i, \Theta_i)}{\delta \rho_j(s_j, \Theta_j)} = \delta(\Theta_i - \Theta_j)\delta_{s_i, s_j}$ , and equate it to the Lagrange multiplier  $\eta$  corresponding to the constraint  $\text{Tr}(\rho_i) = 1$

$$\begin{aligned} \eta = & \frac{\delta(\phi/\mathcal{N})}{\delta \rho_i(s_i, \Theta_i)} \\ = & -z[K\langle s_i \rangle s_i + J\langle q_i \rangle q_i + C(q_i \langle s_i \rangle + \langle q_i \rangle s_i) \\ & + J_s(\langle p_i \cos \Theta_i \rangle p_i \cos \Theta_i + \langle p_i \sin \Theta_i \rangle p_i \sin \Theta_i)] \\ & - \mu_- s_i - \mu_+ q_i - H_x p_i \cos \Theta_i - H_y p_i \sin \Theta_i \\ & + (1 + \ln \rho_i)/\beta. \end{aligned} \quad (4.11)$$

Equation (4.11) can be solved for  $\rho_i(s_i, \Theta_i)$ :

$$\rho_i = e^{\beta\eta - 1 - \beta h_i}, \quad (4.12)$$

where

$$\begin{aligned} h_i(s_i, \Theta_i) = & -s_i(kX + cD + \mu_-) - q_i(jD + cX + \mu_+) \\ & - p_i((j_s M_x + H_x) \cos \Theta_i + (j_s M_y + H_y) \sin \Theta_i) \end{aligned} \quad (4.13)$$

#### 4. Phase diagram of fluid phases in $^3\text{He}$ - $^4\text{He}$ mixtures

is the single-site Hamiltonian in which the coupling constants are rescaled as  $j = zJ$ ,  $c = zC$ ,  $k = zK$ ,  $j_s = zJ_s$  and where the following OPs are introduced:

$$\begin{aligned} X &:= \langle s_i \rangle, \\ D &:= \langle q_i \rangle, \\ M_x &:= \langle p_i \cos \Theta_i \rangle, \\ M_y &:= \langle p_i \sin \Theta_i \rangle, \end{aligned} \tag{4.14}$$

which in the bulk are independent of  $i$ . In accordance with Eq. (4.4) one has  $\langle \tilde{\mathbf{N}}_4 \rangle = \mathcal{N}\mathbf{M}$ . The normalization  $\text{Tr}(\rho_i) = 1$  yields

$$e^{-\beta\eta+1} = \text{Tr}(e^{-\beta h_i}) \tag{4.15}$$

so that

$$\rho_i = \frac{e^{-\beta h_i}}{\text{Tr}(e^{-\beta h_i})}, \tag{4.16}$$

where  $h_i$  is given by Eq. (4.13).

The OPs defined in Eq. (4.14) allow one to determine the number densities  $X_4 = \frac{\langle N_4 \rangle}{\mathcal{N}} = \frac{D+X}{2}$  and  $X_3 = \frac{\langle N_3 \rangle}{\mathcal{N}} = \frac{D-X}{2}$  so that  $X = (\langle N_4 \rangle - \langle N_3 \rangle)/\mathcal{N} = X_4 - X_3$  is the difference of the number densities and  $D = (\langle N_4 \rangle + \langle N_3 \rangle)/\mathcal{N}$  is the total number density. The concentration of  $^4\text{He}$  and  $^3\text{He}$  is  $\frac{\langle N_4 \rangle}{\langle N_4 \rangle + \langle N_3 \rangle} \equiv \mathcal{C}_4 = \frac{D+X}{2D} = X_4/D$  and  $\frac{\langle N_3 \rangle}{\langle N_4 \rangle + \langle N_3 \rangle} \equiv \mathcal{C}_3 = \frac{D-X}{2D} = X_3/D$ , respectively.  $M_x$  and  $M_y$  are the components of the two-dimensional superfluid order parameter  $\mathbf{M} = (M_x, M_y)$  with  $M := \sqrt{|\mathbf{M}|^2} = \sqrt{M_x^2 + M_y^2}$ . The equilibrium superfluid order parameter  $\mathbf{M}$  points into the direction of  $\mathbf{H}$ . This follows from the principle of minimum free energy together with the relation  $\frac{\partial F}{\partial \mathbf{H}} = -\mathbf{M}$ , where  $F$  is the free energy of the system, which implies that for fixed  $T$ ,  $\mu_+$ , and  $\mu_-$  one has  $dF = -d\mathbf{H} \cdot \mathbf{M}$ . Thus for  $\mathbf{H}$  with an orientation  $\psi$ , i.e.,  $\mathbf{H} = (H_x, H_y) = H(\cos \psi, \sin \psi)$  with  $H := \sqrt{|\mathbf{H}|^2} = \sqrt{H_x^2 + H_y^2}$ ,  $\mathbf{M}$  points into the same direction, i.e.,  $\mathbf{M} = (M_x, M_y) = M(\cos \psi, \sin \psi)$ .

Within the aforementioned mean field approximation the order parameters  $X(\mu_-, \mu_+, H, T)$ ,  $D(\mu_-, \mu_+, H, T)$ , and  $M(\mu_-, \mu_+, H, T)$  (with the latter obtained from  $M_x = \text{Tr}(\rho_i p_i \cos \Theta_i)$  and  $M_y = \text{Tr}(\rho_i p_i \sin \Theta_i)$ ) are given by three coupled self-consistent equations:

$$X = \frac{-W(X, D; \mu_-, \mu_+, H, T) + R(X, D; \mu_-, \mu_+, H, T)I_0(\beta j_s M + \beta H)}{1 + W(X, D; \mu_-, \mu_+, H, T) + R(X, D; \mu_-, \mu_+, H, T)I_0(\beta j_s M + \beta H)}, \tag{4.17}$$

$$D = \frac{W(X, D; \mu_-, \mu_+, H, T) + R(X, D; \mu_-, \mu_+, H, T)I_0(\beta j_s M + \beta H)}{1 + W(X, D; \mu_-, \mu_+, H, T) + R(X, D; \mu_-, \mu_+, H, T)I_0(\beta j_s M + \beta H)}, \tag{4.18}$$

and

$$M = \frac{R(X, D; \mu_-, \mu_+, H, T)I_1(\beta j_s M + \beta H)}{1 + W(X, D; \mu_-, \mu_+, H, T) + R(X, D; \mu_-, \mu_+, H, T)I_0(\beta j_s M + \beta H)}, \tag{4.19}$$

where  $I_0$  and  $I_1$  are modified Bessel functions (see Sec. 9.6 in Ref. [115]). The functions  $W(X, D; \mu_-, \mu_+, H, T)$  and  $R(X, D; \mu_-, \mu_+, H, T)$  are given by

$$W(X, D; \mu_-, \mu_+, H, T) = e^{\beta[(c-k)X + (j-c)D + \mu_+ - \mu_-]} > 0 \quad (4.20)$$

and

$$R(X, D; \mu_-, \mu_+, H, T) = e^{\beta[(c+k)X + (j+c)D + \mu_+ + \mu_-]} > 0 \quad (4.21)$$

so that  $D > X$ . The equilibrium free energy  $\phi(\mu_-, \mu_+, H, T)$  is given by (note that due to Eq. (4.18)  $\text{Tr}e^{-\beta h_i} = (1 - D)^{-1}$ )

$$\begin{aligned} \phi(\mu_-, \mu_+, H, T) = \mathcal{N} & \left[ \frac{k}{2} X^2 + \frac{j}{2} D^2 + cXD + \frac{j_s}{2} M^2 \right. \\ & \left. + \frac{1}{\beta} \ln(1 - D) \right]. \end{aligned} \quad (4.22)$$

In the limit  $\mu_+ \rightarrow +\infty$  both  $W$  and  $R$  diverge so that according to Eq. (4.18) one has  $D(\mu_-, \mu_+ \rightarrow +\infty, H, T) \rightarrow 1$ , i.e., all lattice sites are occupied and the concentrations reduces to  $\mathcal{C}_4 = (1 + X)/2$  and  $\mathcal{C}_3 = (1 - X)/2$ . With the explicit expressions in Eqs. (4.20) and (4.21), in the limit  $\mu_+ \rightarrow +\infty$ , Eqs. (4.17) and (4.19), reduce to:

$$X = \frac{-e^{-\beta(2kX + 2c + 2\mu_-)} + I_0(\beta j_s M + \beta H)}{e^{-\beta(2kX + 2c + 2\mu_-)} + I_0(\beta j_s M + \beta H)}, \quad \mu_+ = \infty, \quad (4.23)$$

and

$$M = \frac{I_1(\beta j_s M + \beta H)}{e^{-\beta(2kX + 2c + 2\mu_-)} + I_0(\beta j_s M + \beta H)}, \quad \mu_+ = \infty. \quad (4.24)$$

Expressing  $X$  in Eqs. (4.23) and (4.24) in terms of  $\mathcal{C}_4$  renders

$$\mathcal{C}_4 = \frac{I_0(\beta j_s M + \beta H)}{e^{\beta(-\tilde{k}\mathcal{C}_4 + \tilde{\Delta}_-)} + I_0(\beta j_s M + \beta H)}, \quad \mu_+ = \infty, \quad (4.25)$$

and

$$M = \frac{I_1(\beta j_s M + \beta H)}{e^{\beta(-\tilde{k}\mathcal{C}_4 + \tilde{\Delta}_-)} + I_0(\beta j_s M + \beta H)}, \quad \mu_+ = \infty, \quad (4.26)$$

where  $\tilde{k} = 4k$  and  $\tilde{\mu}_- = 2(-\mu_- + k - c)$ . For  $H = 0$  these equations have the same form as the corresponding ones in Ref. [113], which do not allow for vacant sites from outset. Thus in the limit  $\mu_+ \rightarrow +\infty$  and for  $H = 0$  our present more general results reduce to those of the more restricted model studied before.

### 4.3. Phase diagrams

In this section various topologies of the phase diagram of VBEG model within mean field theory are obtained. Although certain features of the phase diagram can be obtained

## 4. Phase diagram of fluid phases in $^3\text{He}$ - $^4\text{He}$ mixtures

---

analytically, most parts of it can be determined only numerically; this has been done using Mathematica software [116, 117]. In order to find the coexisting states of phase equilibria, one has to identify those distinct states  $(X_\nu, D_\nu, M_\nu)$ , which share the same values for the chemical potentials and the pressure at a common temperature. The chemical potentials can be obtained by solving Eqs. (4.17) and (4.18) together with Eqs. (4.20) and (4.21) for  $\mu_+$  and  $\mu_-$ :

$$\begin{aligned} \mu_+(X, D, M; H, T) = & \frac{T}{2} \ln(D^2 - X^2) - T \ln(2(1 - D)) - cX - jD \\ & - \frac{T}{2} \ln(I_0(j_s M/T + H/T)) \end{aligned} \quad (4.27)$$

and

$$\mu_-(X, D, M; H, T) = \frac{T}{2} \ln \frac{D + X}{D - X} - kX - cD - \frac{T}{2} \ln(I_0(j_s M/T + H/T)). \quad (4.28)$$

Within the grand canonical ensemble the pressure is given by  $\phi/\mathcal{N} = -P$ . (Note that the sample volume is  $V = \mathcal{N}a^3$ , here with  $a = 1$ ). According to Eqs. (4.17) - (4.19) the OPs of any state must fulfill the relation

$$\frac{2M}{X + D} = \frac{M}{X_4} = \frac{I_1(\beta j_s M + \beta H)}{I_0(\beta j_s M + \beta H)}, \quad (4.29)$$

which expresses  $M$  in terms of  $\frac{X+D}{2} = X_4$ ,  $T$ , and  $H$ . Depending on the value of the coupling constant  $j_s$  the phase diagram exhibits various topologies.

### 4.3.1. Phase diagram for a classical binary liquid mixture

For  $j_s = 0$  and  $H = 0$  there is no superfluid phase and  $M$  is always zero (compare Eq. (4.29) with  $I_1(y \rightarrow 0) = \frac{1}{2}y$  and  $I_0(y \rightarrow 0) = 1$ ). For  $j_s = 0$ , due to  $I_0(0) = 1$  the last term in Eq. (4.27) and in Eq. (4.28) drops out. Thus the phase diagram will be that of a classical binary liquid mixture of species 3 and 4, similar to the ones shown in Refs. [109–111]. The first-order demixing transitions occur at low temperatures, whereas at high temperatures the liquid is mixed. The demixing transitions terminate in a line of critical points which due to  $\frac{\partial \phi}{\partial X} = -\mu_-$  (see Eqs. (4.10) and (4.14)) are given by [114]

$$\left. \frac{d\mu_-}{dX} \right|_{\mu_+, T} = \left. \frac{d^2\mu_-}{dX^2} \right|_{\mu_+, T} = 0, \quad \left. \frac{d^3\mu_-}{dX^3} \right|_{\mu_+, T} > 0, \quad (4.30)$$

where  $\frac{d^n \mu_-}{dX^n} \Big|_{\mu_+, T}$  denotes the  $n^{\text{th}}$  total derivative of  $\mu_-$  (see Eq. (4.28)) with respect to  $X$  at constant  $\mu_+$  and  $T$ . Note that the independent variables are  $(T, \mu_+, \mu_-)$ . Since  $\mu_-$  as given by Eq. (4.28) depends on  $D$ , which for  $\mu_+ = \text{const}$  depends in turn implicitly on

$X$  via Eq. (4.27), calculating the total derivative of  $\mu_-$  with respect to  $X$  requires the knowledge of the partial derivative of  $D$  with respect to  $X$ . Thus the first condition in Eq. (4.30) reads

$$\left. \frac{d\mu_-}{dX} \right|_{\mu_+, T} = \left. \frac{\partial \mu_-}{\partial X} \right|_{\mu_+, T} + \left. \frac{\partial \mu_-}{\partial D} \frac{\partial D}{\partial X} \right|_{\mu_+, T} = 0, \quad (4.31)$$

where  $\left. \frac{\partial \mu_-}{\partial X} \right|_{\mu_+, T}$  and  $\left. \frac{\partial \mu_-}{\partial D} \right|_{\mu_+, T}$  follow from Eq. (4.28) and where  $\left. \frac{\partial D}{\partial X} \right|_{\mu_+, T}$  is obtained by taking the derivative of Eq. (4.27) with respect to  $X$  at fixed  $\mu_+$  and  $T$  and by solving for  $\left. \frac{\partial D}{\partial X} \right|_{\mu_+, T}$ . Accordingly, the first condition in Eq. (4.30) leads to a quadratic equation:

$$T^2 + a_1 T + a_0 = 0 \quad (4.32)$$

with

$$\begin{aligned} a_1 &= -D(-2cX + j + k) + X(kX - 2c) + D^2 j, \\ a_0 &= (D - 1)(D^2 - X^2)(c^2 - jk). \end{aligned} \quad (4.33)$$

Equation (4.32) renders as solution two branches  $T_{1,2}(X, D)$ . Similarly, the second condition in Eq. (4.30) leads to an equation  $G(X, D, T) = 0$  where, due to the first condition,  $T = T_{1,2}(X, D)$ . Thus it takes the form  $G(X, D, T_{1,2}(X, D)) =: g_{1,2}(X, D) = 0$ . Therefore, for a given value  $D^{(0)}$  of  $D$ , the solution of  $g_{1,2}(X, D^{(0)}) = 0$  (which must be solved numerically) renders  $X(D_{1,2}^{(0)}) = X_{1,2}^{(0)}$  so that at  $T_{1,2}^{(0)} = T_{1,2}(X_{1,2}^{(0)}, D_{1,2}^{(0)})$  the model exhibits a critical point, provided the condition  $\left. \frac{d^3 \mu_-}{dX^3} \right|_{\mu_+, T} > 0$  is fulfilled. This latter condition and the physical constraints  $T > 0$ ,  $P > 0$ , and  $D > |X|$  exclude one of the two branches of  $T_{1,2}(X, D)$ . Thus for various values of  $D$  one obtains a set of points  $\{(D, X(D), T(X(D), D))\}$ , which forms a line of critical points in the space spanned by  $(X, D, T)$ . According to Eqs. (4.27) and (4.28), the set  $\{(D, X, T)\}$  can be transformed to the set  $\{(\mu_+(D, X; T), \mu_-(D, X; T), T)\}$ , which yields a line of critical points in the space spanned by  $(\mu_+, \mu_-, T)$ . This line ends at the liquid–vapor coexistence surface forming a critical end point (see Fig. 4.1).

The schematic phase diagram for  $j_s = 0$  in the  $(T, Z, P)$  space is shown in Fig. 4.1, with  $Z = \exp(\mu_3/T)$ . There are four surfaces separating various phases: the surface SL of first–order phase transitions between the solid and the liquid phases, the surface VL of first–order phase transitions between the vapor and the liquid phases, the surface SV of first–order phase transitions between the solid and the liquid phases, and the surface LL of first–order phase transitions between the phase rich in component 3 and the phase rich in the component 4. This latter surface terminates at a line of critical points (brown line), and VL terminates at a line of critical points (green line).

In Fig. 4.2, the demixing transitions at coexistence with the vapor phase (see the line connecting the points 'a' and 'c' in Fig. 4.1) are shown for the coupling constants

#### 4. Phase diagram of fluid phases in $^3\text{He}$ - $^4\text{He}$ mixtures

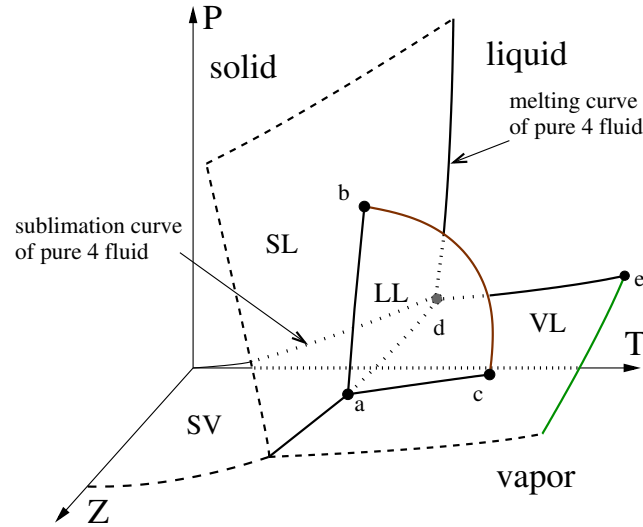


**Figure 4.1.** Schematic phase diagram for  $H = 0$  and  $j_s = 0$  (i.e., without coupling between the superfluid degrees of freedom). The phase diagram in the plane  $Z = 0$  is that of a one-component system consisting of particles "4". Upon increasing the fugacity  $Z$  of particles "3", the transition lines in the plane  $Z = 0$  extend to form three distinct surfaces. The surface SL is a surface of first-order phase transitions between the solid and the liquid phases. The transition surfaces between the vapor and the liquid phases, and between the solid and the vapor phases are denoted by VL and SV, respectively. The surface VL terminates at a line of critical points (green line). The critical point of the pure system of "4" particles is denoted by 'e'. The liquid can be either mixed or demixed. Concerning the demixed phases, LL denotes the surface of first-order phase transitions between the phase rich in component 3 (large  $Z$ ) and the phase rich in the component 4 (small  $Z$ ). This surface terminates at a line of critical points (brown line), which meets the surfaces SL and VL at the critical end points 'b' and 'c', respectively. The point 'a' is a quadruple point, whereas 'd' is a triple point. The lines a-b, a-c, and a-d are triple lines. The dashed lines have no physical meaning; they indicate that the corresponding surfaces continue.

chosen as  $(c/k, j/k, j_s/k) = (1, 5.714, 0)$ . Along this triple line of first-order liquid-liquid transitions at coexistence with the vapor phase, three thermodynamic states with distinct number densities and concentrations coexist. The values of the OPs of these three states are shown in Figs. 4.2(a) - (d). The corresponding values of the pressure  $P/k$  and of the fugacity,  $Z = \exp(\mu_3/T) = \exp(\frac{\mu_3}{k} \frac{1}{T/k})$  of the component 3 of the mixture ( $\mu_3 = \mu_+ - \mu_-$  and  $T$  are rescaled by the coupling constant  $k$ ) are shown in Figs. 4.2(e) and (f), respectively. The vapor phase is characterized by a small value  $D_v$  of the order parameter  $D$ , whereas a large value  $D_l$  of the density order parameter  $D$  corresponds to the liquid state. In Fig. 4.2, at fixed temperatures below the critical end point (ce) (which is denoted as 'c' in Fig. 4.1), three values for  $X_3$ , i.e., two values  $X_3^l$  for  $X_3$  in the liquid phases (Fig. 4.2(a)) and one value for the vapor phase ( $X_v$  in Fig. 4.2(b)), and

three values for  $D$  (Figs. 4.2(c) - (d)) characterize the three states which share the same values of the pressure (Fig. 4.2(e)) and of the chemical potentials (and thus the fugacity, Fig. 4.2(f)). At  $T_{ce}/k = 1.947$  the two liquid states merge into a single state with  $(X_l^{ce}, D_l^{ce}, M_l^{ce}) = (0.050, 0.913, 0)$ , which coexists with the vapor state characterized by  $(X_v^{ce}, D_v^{ce}, M_v^{ce}) = (-0.120, 0.180, 0)$ . For  $T > T_{ce}$  the liquid is mixed. The transitions between the vapor and the liquid phases are always first order, above and below  $T_{ce}$ .

### 4.3.2. Phase diagram including the superfluid phase

For  $j_s > 0$  the model exhibits superfluid transitions, which can be either first or second order. In order to find the surface of second-order phase transitions to the superfluid phase (see  $A_3$  in Fig. 3.3), one can introduce the appropriate thermodynamic potential  $A$  as the Legendre transform of  $\phi$ :

$$A(\mu_-, \mu_+, M, T) = \phi(\mu_-, \mu_+, H(\mu_-, \mu_+, M, T), T) - MH(\mu_-, \mu_+, M, T), \quad (4.34)$$

where, according to Eq. (4.1),

$$\frac{\partial \phi(\mu_-, \mu_+, M, T)}{\partial H} = M \quad (4.35)$$

which implicitly renders  $H = H(\mu_-, \mu_+, M, T)$  so that  $\frac{\partial A(\mu_-, \mu_+, M, T)}{\partial M} = -H(\mu_-, \mu_+, M, T)$ . In order to determine the explicit expression of  $H$  in terms of the OPs, one can use Eq. (4.29). Since  $H = 0$  corresponds to the actual experimental situation, the right hand side of Eq. (4.29) can be replaced by its approximation linear in  $H$ :

$$\frac{2M}{X + D} = \frac{I_1(j_s M/T)}{I_0(j_s M/T)} + \frac{H I_1'(j_s M/T) I_0(j_s M/T) - I_0'(j_s M/T) I_1(j_s M/T)}{I_0^2(j_s M/T)}. \quad (4.36)$$

Solving this equation for  $H$  (using  $I_0' = I_1$ ,  $I_1' = (I_0 + I_2)/2$ , and  $I_2(a) = I_0(a) - \frac{2}{a}I_1(a)$ ) leads to

$$\begin{aligned} H &= \frac{I_1(j_s M/T)}{M/T} \frac{2MI_0(j_s M/T) - (X + D)I_1(j_s M/T)}{I_0^2(j_s M/T) + I_0(j_s M/T)I_2(j_s M/T) - 2I_1^2(j_s M/T)} \\ &= \frac{-j_s T I_1(j_s M/T)[-2MI_0(j_s M/T) + (D + X)I_1(j_s M/T)]}{2[-j_s M(I_1(j_s M/T))^2 + I_0(j_s M/T)[T I_1(j_s M/T) + j_s M I_2(j_s M/T)]}. \end{aligned} \quad (4.37)$$

Due to  $\frac{\partial A}{\partial M} = -H$  the conditions for the critical points, where  $M$  vanishes continuously (see  $A_3$  in Fig. 3.3), are (compare Eq. (4.30))

$$\left. \frac{dH}{dM} \right|_{\mu_+, \mu_-, T} = \left. \frac{d^2 H}{dM^2} \right|_{\mu_+, \mu_-, T} = 0, \quad \left. \frac{d^3 H}{dM^3} \right|_{\mu_+, \mu_-, T} > 0, \quad (4.38)$$

#### 4. Phase diagram of fluid phases in ${}^3\text{He}$ - ${}^4\text{He}$ mixtures

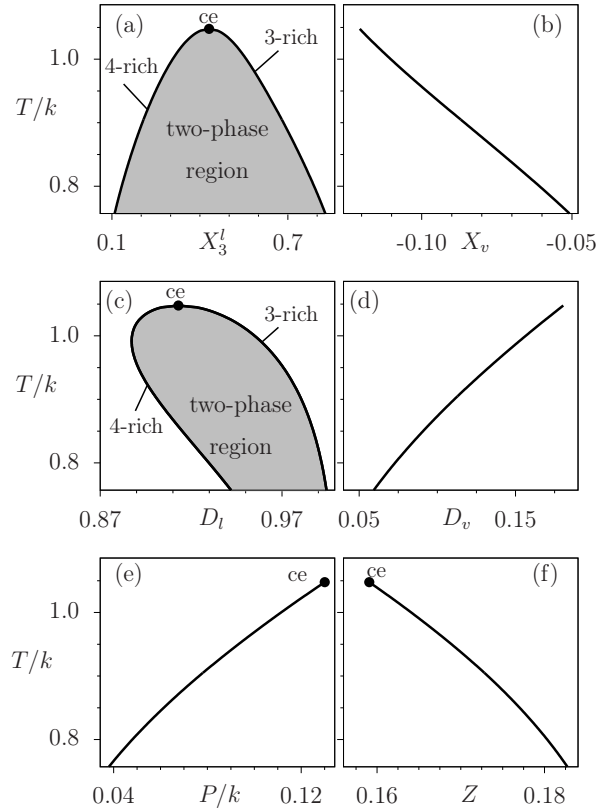


**Figure 4.2.** Phase diagrams for the coupling constants  $(c/k, j/k, j_s/k) = (1, 5.714, 0)$  and  $H = 0$ . Along the triple line of three-phase coexistence (see line a-c in Fig. 4.1) the figures show the first-order demixing transitions of the liquid at coexistence with the vapor phase (a) in the  $(X_3^l, T)$  plane, with  $X_3^l = \langle N_3 \rangle_l / \mathcal{N}$  corresponding to the 3-particles in the liquid phase, (b) in the  $(X_v, T)$  plane at coexistence with the two liquid phases, where  $X_v = (\langle N_4 \rangle_v - \langle N_3 \rangle_v) / \mathcal{N}$  in the vapor phase, (c) in the  $(D_l, T)$  plane, where  $D_l = (\langle N_4 \rangle_l + \langle N_3 \rangle_l) / \mathcal{N}$  in the liquid phase, and (d) in the  $(D_v, T)$  plane, where  $D_v = (\langle N_4 \rangle_v + \langle N_3 \rangle_v) / \mathcal{N}$  in the vapor phase. The indices 'l' and 'v' refer to the values of the OPs in the liquid and in the vapor phase, respectively. The critical end point ce here corresponds to the point c in Fig. 4.1. Panels (e) and (f) show the dependences of the pressure  $P$  and of the fugacity  $Z = \exp(\mu_3/T)$  on the temperature along the triple line a-c in Fig. 4.1. The two liquid states become identical at the critical end point ce at  $T_{ce}/k = 1.947$ , above which the liquid is mixed. The coexisting liquid and vapor phases at ce are  $(X_l^{ce}, D_l^{ce}, M_l^{ce}) = (0.050, 0.913, 0)$  and  $(X_v^{ce}, D_v^{ce}, M_v^{ce}) = (-0.120, 0.180, 0)$ , respectively. The transitions between the vapor phase and the liquid phases are always first order. According to (e) and (f), along a-c both  $P$  and  $Z$  vary as function of  $T$ , with the requirement of staying in coexistence with the vapor phase. This implies that the white domains in (a) and (c) are not projections of a three-dimensional surface, given by the equation of state, onto the  $(T, X_3)$  and  $(T, D)$  plane, respectively. The black lines provide only the  $T$ -dependence of  $X_3$  and  $D_l$  along the line a-c, which contains two branches. Similar remarks hold for Figs. 4.6 - 4.9.

with all total derivatives to be taken at  $M = 0$  and at constant  $\mu_+$ ,  $\mu_-$ , and  $T$  (compare Eq. (4.31)). Note that the independent variables are  $(T, \mu_+, \mu_-)$ . According to Eq. (4.37), calculating the total derivatives of  $H$  with respect to  $M$  requires the expression for  $\frac{\partial H}{\partial M}$  and the knowledge of the partial derivatives of  $X$  and  $D$  with respect to  $M$ . These latter ones are obtained by taking the partial derivatives of Eqs. (4.27) and (4.28) with respect to  $M$  at fixed  $\mu_+$  and  $\mu_-$  and by solving the resulting two coupled equations for the required derivatives  $\frac{\partial X}{\partial M}$  and  $\frac{\partial D}{\partial M}$ .

Applying the conditions for critical points (Eq. (4.38)) leads to the following expression for the surface  $A_3$  of superfluid transitions:

$$T_s = \frac{j_s}{4}(D + X). \quad (4.39)$$

Note that the same relation follows independently from Eq. (4.29) for  $H = 0$  in the limit  $M \rightarrow 0$ . The route via Eq. (4.37) has, however, the additional advantage of facilitating also the calculation of tricritical points (see Eqs. (4.40) - (4.42)). Furthermore, expanding the right hand side of Eq. (4.29) up to and including the order  $H^3$  leaves the result in Eq. (4.39) unchanged.

With  $D$  and  $X$  given by Eqs. (4.17) - (4.19) in terms of  $\mu_+$ ,  $\mu_-$ , and  $T$  (note that  $H = 0$  and that on this surface  $M = 0$ ), Eq. (4.39) renders  $T_s(\mu_-, \mu_+)$  which corresponds to a surface in the space spanned by  $(\mu_+, \mu_-, T)$ . This surface of second-order phase transitions between the normal fluid ( $M = 0$ ) and the superfluid ( $M \neq 0$ ) ends at the surface of liquid-vapor coexistence, forming a line of critical end points (see the line connecting *ce* and *tce* in Fig. 3.3). The conditions for tricritical points are

$$\left. \frac{dH}{dM} \right|_{\mu_+, \mu_-, T} = \left. \frac{d^2 H}{dM^2} \right|_{\mu_+, \mu_-, T} = \left. \frac{d^3 H}{dM^3} \right|_{\mu_+, \mu_-, T} = \left. \frac{d^4 H}{dM^4} \right|_{\mu_+, \mu_-, T} = 0, \quad \left. \frac{d^5 H}{dM^5} \right|_{\mu_+, \mu_-, T} > 0, \quad (4.40)$$

with all total derivatives to be taken also at  $M = 0$ , which again requires to consider the partial derivatives of  $X$  and  $D$  with respect to  $M$ , as discussed after Eq. (4.38). The vanishing of the first four derivatives leads to a quadratic equation for  $D$  (where Eq. (4.39) has been used to eliminate the dependence on  $T$ ):

$$b_2 D^2 + b_1 D + b_0 = 0, \quad (4.41)$$

where the coefficients  $b_{0,1,2}$  are given in terms of the order parameter  $X$  and the coupling constants:

$$\begin{aligned} b_0 &= X(16c^2 - (4j + j_s)(4k + j_s)) \\ &\quad + X^2 j_s(4k + j_s), \\ b_1 &= 2X(j_s^2 - 8c^2 + 8jk + 2j_s(j + k)) \\ &\quad - (4c + j_s)^2 + 16jk, \\ b_2 &= 16c^2 + j_s(8c - 4k + j_s) - 16jk. \end{aligned} \quad (4.42)$$

#### 4. Phase diagram of fluid phases in ${}^3\text{He}$ - ${}^4\text{He}$ mixtures

Note that, also here, expanding the right hand side of Eq. (4.29) up to and including the order  $H^2$  does not change the results in Eqs. (4.41) and (4.42).

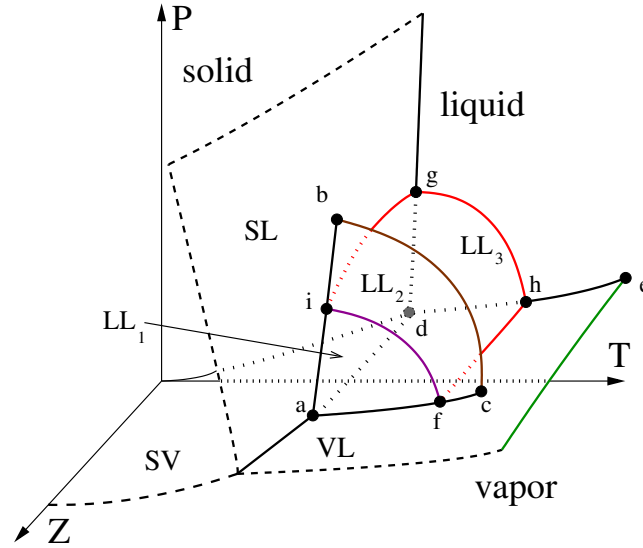


**Figure 4.3.** Schematic phase diagram for small values of  $j_s$ . SL, VL, and SV are surfaces of first-order phase transitions with the same meanings as in Fig. 4.1. The points denoted as 'g' and 'h' are critical end points of the continuous superfluid transition of the 4-pure fluid (i. e.,  $Z = 0$ ); g-h is the line of critical points for the continuous superfluid transition of the 4-pure fluid.  $LL_3$  (enclosed by the lines g-h, h-f, f-i, i-g) is a surface of continuous superfluid transitions bounded by the red lines g-h, h-f, i-g, and the violet line f-i. The triple point of the solid, vapor, and superfluid phases of the 4-pure fluid is denoted as 'd'. In the plane  $Z = 0$  the line to the left of 'd' is the sublimation curve of the 4-pure fluid; d-h-e is the liquid-vapor coexistence line of the 4-pure fluid, which ends at its critical point 'e'; the extension of the latter to  $Z > 0$  forms the green line. The line d-g is the melting curve of the 4-pure solid into the superfluid and above 'g' into the normal fluid. The line d-a is the triple line along which solid, vapor, and superfluid coexist; beyond 'a' this line extends into a triple line along which solid, vapor, and normal fluid coexist. At the quadruple point 'a' solid, vapor, normal fluid, and superfluid coexist. The surfaces  $LL_1$  and  $LL_2$  are enclosed by the lines a-f, f-i, i-a and the lines f-c, c-b, b-i, respectively. The surface  $LL_1 \cup LL_2$ , which corresponds to the surface LL in Fig. 4.1, is the surface of first-order transitions between the 4-rich liquid at the back and the 3-rich liquid in the front; it is bounded by the brown line b-c of critical points which connects the critical end points 'b' and 'c'. The surface  $LL_1 \cup LL_2$  of first-order liquid-liquid demixing transitions terminates the surface  $LL_3$  of continuous superfluid transitions. At this intersection this gives rise to the violet line f-i of critical end points, which themselves end at the end points 'i' and 'f' of this line of critical end points. At the surface  $LL_2$  there are first-order phase transitions between two normal fluids whereas at the surface  $LL_1$  there are first-order phase transitions between a normal fluid with high concentration of 3-particles and a superfluid with high concentration of 4-particles. Accordingly, the superfluid phase forms a dome formed by the plane  $Z = 0$ , SL, VL,  $LL_3$ , and  $LL_1$  with the vertices 'd', 'a', 'f', 'h', 'g', and 'i'.

Accordingly, the solution of Eq. (4.41) yields  $D = D_0(X)$  which due to Eqs. (4.17) - (4.19) leads to the relation  $D(\mu_-, \mu_+, T) = D_0(X(\mu_-, \mu_+, T))$ . This turns into a relationship  $T(\mu_-, \mu_+)$  which corresponds to a surface in the space spanned by  $(\mu_+, \mu_-, T)$ . Simultaneously Eq. (4.39) has to hold which also corresponds to a surface in this space. Therefore the tricritical points correspond to the intersection of these two surfaces and thus form a line of tricritical points (TC in Fig. 3.3). The condition for the fifth derivative along this line can be checked only numerically. This condition and the fact that  $D > |X|$  exclude one of the two solutions of Eq. (4.41). For small values of  $j_s$  the model exhibits a superfluid transition in the liquid phase (see Fig. 4.3). In certain parts of the phase diagram this transition is second order, in other parts it is first order. Thus upon switching on  $j_s$  a new surface  $LL_3$  raises above the bottom (i. e., VL) of the phase diagram shown in Fig. 4.1 and changes the character of the lower part of the surface LL in Fig. 4.1, indicated as  $LL_1$ , in Fig. 4.3.

The surface  $LL_3$  of continuous transitions separates the superfluid and the normal fluid both 4-rich. The surface  $LL_1$  corresponds to first-order phase transitions between the 4-rich superfluid and the 3-rich normal fluid. The surface  $LL_1 \cup LL_2$  terminates  $LL_3$  at a line f-i of critical end points.

Upon increasing the coupling constant  $j_s$  (Fig. 4.4), the model exhibits as a new feature a line j-k of tricritical points. In comparison with the phase diagram for weak  $j_s$  (Fig. 4.3), a new surface  $LL_4$  emerges (j-k-f-i-j) which is the surface of first-order phase transitions between the superfluid and the normal fluid, both 4-rich (Fig. 4.4). The surface  $LL_3$  of the second-order phase transitions between the superfluid and the normal fluid both 4-rich meet the surface  $LL_4$  at a line of tricritical points (dark blue line j-k).  $LL_1$  and  $LL_2$  meet  $LL_4$  at a triple line (i-f), where the superfluid and the 4-rich normal fluid coexist with the 3-rich normal fluid. Thus the increase of  $j_s$  changes the character of that part of  $LL_3$  in Fig. 4.3, which is close to  $LL_2$ , from second-order to first-order phase transitions.

If the coupling constant  $j_s$  is increased further (Fig. 4.5), first-order phase transitions between liquid phases occur only between the superfluid and the normal fluid phase. There are no longer first-order demixing transitions between two normal fluids. Thus, upon increasing  $j_s$ , the surface  $LL_3 \cup LL_4$  in Fig. 4.4 moves up (i.e., towards higher  $P$  and  $T$ ) so that accordingly the line i-f also moves up towards the line b-c. This implies that  $LL_2$  shrinks and the wedge between the lines i-b and i-j becomes shorter. Finally  $LL_2$  and b-c disappear and  $LL_1$  and  $LL_4$  become a single surface of first-order transitions between 4-rich superfluid and 3-rich normal liquid; this implies that the line i-f disappears, too. Accordingly, the phase diagram is left with only a (blue) line of tricritical points k-j. This topology of the phase diagram is shown in Fig. 4.5. In this case the liquid-liquid phase transitions are either second-order phase transitions on  $LL_3$  between the normal fluid

#### 4. Phase diagram of fluid phases in $^3\text{He}$ - $^4\text{He}$ mixtures

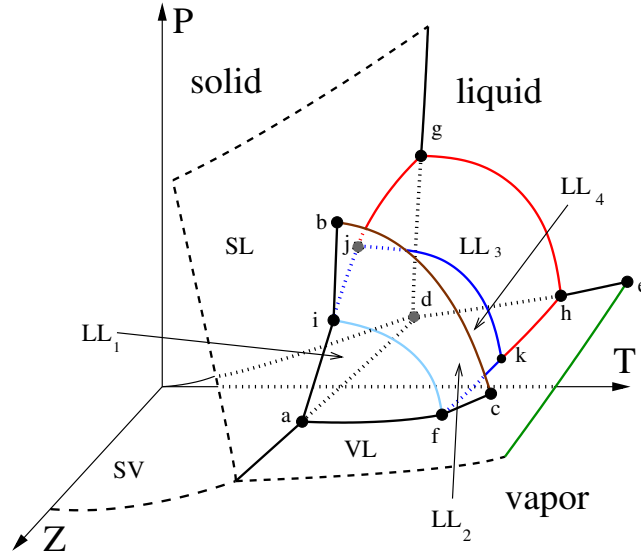


**Figure 4.4.** Schematic phase diagram for a value of  $j_s$ , for which both critical (b-c and  $LL_3$ ) and tricritical (j-k) phase transitions between liquids occur. SL, VL, and SV are the surfaces of first-order phase transitions similar to Fig. 4.1. The superfluid dome is characterized by the vertices 'a', 'f', 'k', 'h', 'g', 'd', 'j', 'i'. Outside this region the liquid is a normal fluid.  $LL_1$  (enclosed by the lines a-i, i-f, f-a) is the surface of first-order phase transitions between the 3-rich normal fluid and the 4-rich superfluid,  $LL_2$  (enclosed by the lines i-b, b-c, c-f, f-i) is the surface of first-order demixing phase transitions between 3-rich and 4-rich normal fluids, whereas  $LL_3$  (enclosed by the lines j-g, g-h, h-k, k-j) is the surface of second-order phase transitions between the normal fluid and the superfluid. The blue line (j-k) is the line of tricritical points where the surface  $LL_3$  connects to the new surface  $LL_4$  (enclosed by the lines i-j, j-k, k-f, f-i) of first-order phase transitions between the normal fluid and the superfluid liquid phases both being 4-rich. The surfaces  $LL_2$  and  $LL_3 \cup LL_4$  meet at the line of triple points (light blue line i-f). The brown and the green lines are lines of critical points; 'a', 'i', and 'f' are quadruple points, 'd' is a triple point, whereas 'b', 'c', 'g', and 'h' are critical end points. The line of triple points (i-f) ends on the surfaces SL and VL at the points 'i' and 'f', respectively. The points 'j' and 'k' are tricritical end points. Note that in Fig. 4.3 the line i-f is a line of critical end points whereas here it is a triple line. This different character motivates their different color code (violet versus light blue). This different character also implies that the lines a-i-b and a-f-c have a break in slope at 'i' and 'f', respectively, here, but not in Fig. 4.3.

and the superfluid mixed liquid, or first-order phase transitions on  $LL_4 \cup LL_1$  between the normal fluid and the superfluid liquid.

As discussed in Sec. 3.1, in the case of actual  $^3\text{He}$  -  $^4\text{He}$  mixtures the solid phase is formed only at high pressures, whereas for sufficiently low pressures the superfluid reaches down to  $T = 0$ . In order to obtain this topology from that of Fig. 4.5, by fiat one has to pull up and tilt the surface SL and to shift the superfluid dome down to  $T = 0$  so that the surface SV disappears. This transforms the phase diagram in Fig. 4.5 to the

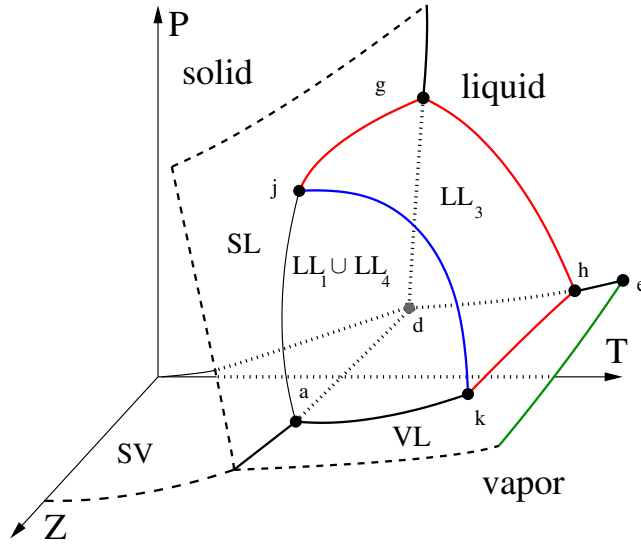


**Figure 4.5.** Schematic phase diagram for a value of  $j_s$ , for which only a tricritical line occurs. In this case, first-order phase transitions between liquid phases occur only between the superfluid and the normal fluid so that the model exhibits only a (blue) line of tricritical points (j-k). SL, VL, and SV are the surfaces of first-order phase transitions as described in Fig. 4.1. The superfluid dome is characterized by the vertices 'a', 'k', 'h', 'g', 'd', and 'j'. Outside this region the liquid is a normal fluid. The surface  $LL_2$  from Fig. 4.4 does not exist anymore and the transitions between liquid phases are either second-order phase transitions between the normal fluid and the superfluid mixed liquid ( $LL_3$  enclosed by the lines g-j, j-k, k-h, h-g), or first-order phase transitions between the normal fluid and the superfluid liquid ( $LL_1 \cup LL_4$  enclosed by the lines a-k, k-j, j-a). The surfaces  $LL_3$  and  $LL_1 \cup LL_4$  meet at the line j-k of tricritical points (blue line). The points 'g' and 'h' are critical end points, whereas 'j' and 'k' are tricritical end points. The point 'a' is a quadruple point and 'd' is a triple point.

one shown in Fig. 3.3 such that  $g = ce^+$ ,  $h = ce$ ,  $e = c$ ,  $LL_3 = A_3$ ,  $j-k = TC$ ,  $j = tce^+$ ,  $k = tce$ , and  $LL_1 \cup LL_4 = A_4$ . In this sense the bulk phase diagram shown in Fig. 4.5 is supposed to mimic the one of the actual  ${}^3\text{He}$ - ${}^4\text{He}$  mixtures.

The demixing transitions at coexistence with the vapor phase for various sets of the coupling constants are shown in Figs. 4.6 - 4.9. In these figures the values of  $c/k$  and  $j/k$  are the same; only the value of  $j_s$  is changed. For the choice of coupling constants  $(c/k, j/k, j_s/k) = (1, 5.714, 1.717)$  (see Fig. 4.6), the phase diagram exhibits the topology of the schematic phase diagram shown in Fig. 4.3. The red line in Fig. 4.6(a) provides the temperature dependence of  $X_3$  along the red line in Fig. 4.3 emanating from 'f' towards 'h'. The green point 'e' in Fig. 4.6 corresponds to the point 'f' in Fig. 4.3 and the black point in Fig. 4.6 corresponds to the point 'c' in Fig. 4.3. Because in Fig. 4.3 the red line h-f is a line of continuous phase transitions right up to the point 'f', the line a-f-c does not exhibit a break in slope at 'f'. Below e, the liquid transitions are

#### 4. Phase diagram of fluid phases in $^3\text{He}$ - $^4\text{He}$ mixtures

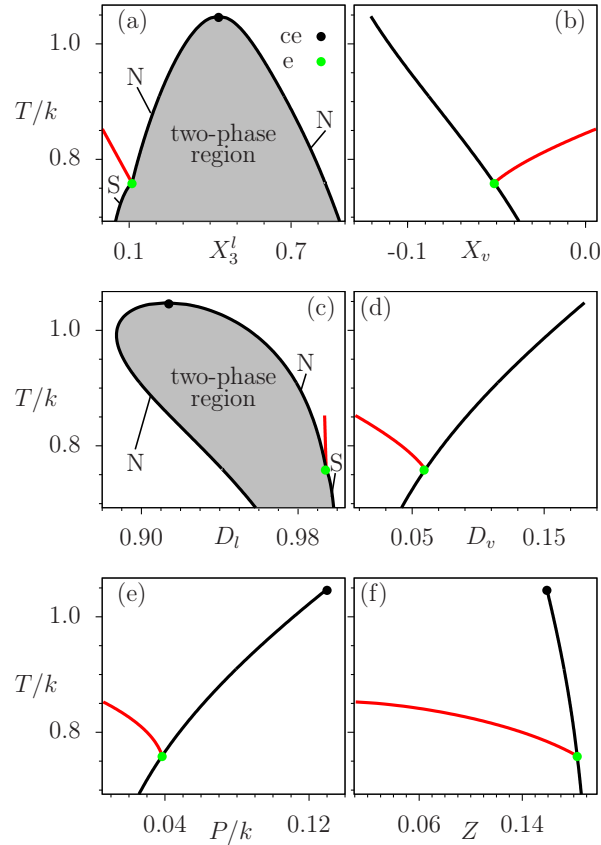


**Figure 4.6.** Phase diagram for the coupling constants  $(c/k, j/k, j_s/k) = (1, 5.714, 1.717)$  and  $H = 0$  corresponding to Fig. 4.3. Along the triple line a-f in Fig. 4.3 the figures show the coexistence between vapor, normal fluid, and superfluid (a) in the  $(X_3^l, T)$  plane, with  $X_3^l = \langle N_3 \rangle / \mathcal{N}$  corresponding to the number density of 3-particles in the liquid phase, (b) in the  $(X_v, T)$  plane at coexistence with the two liquid phases, where  $X_v = (\langle N_4 \rangle_v - \langle N_3 \rangle_v) / \mathcal{N} = \langle X_4^v \rangle - \langle X_3^v \rangle$  in the vapor phase, (c) in the  $(D_l, T)$  plane, where  $D_l = (\langle N_4 \rangle_l + \langle N_3 \rangle_l) / \mathcal{N}$  is the total number density in the liquid phase, and (d) in the  $(D_v, T)$  plane, where  $D_v = (\langle N_4 \rangle_v + \langle N_3 \rangle_v) / \mathcal{N}$  is the total number density in the vapor phase. The indices 'l' and 'v' refer to the values of the OPs in the liquid and the vapor phase, respectively. Panels (e) and (f) show the temperature dependence of  $P$  and  $Z$  along the triple line a-c Fig. 4.3 (black) and along the red line f-h near 'f' in Fig. 4.3. The red line is the line of second-order transitions between the normal fluid and superfluid at coexistence with vapor, which ends at the demixing curve at the green critical end point 'e' (i. e., 'f' in Fig. 4.3). At 'e' the liquid state  $(X_l^e, D_l^e, M_l^e) = (0.773, 0.994, 0)$  coexists with the vapor state  $(X_v^e, D_v^e, M_v^e) = (-0.051, 0.059, 0)$  at  $T_e/k = 0.758$ . N and S denote normal fluid and superfluid, respectively. The transitions between the vapor and the liquid phases are always first order. The points 'ce' and 'e' here correspond to the points 'c' and 'f' in Fig. 4.3. The red curve in panel (c) continues further away from the green point; however, it is plotted only within the temperature range of the red curves in the other panels.

first-order transitions between the normal fluid and the superfluid liquid, whereas above the demixing curve remains the same as in the case of  $j_s = 0$  (see Fig. 4.1).

As discussed in Fig. 4.4, for even larger values of  $j_s$ , both continuous and first-order superfluid transitions occur, giving rise to the occurrence of a line of tricritical points. For the choice of coupling constants  $(c/k, j/k, j_s/k) = (1, 5.714, 2.231)$  and  $(c/k, j/k, j_s/k) = (1, 5.714, 2.747)$  Figs. 4.7 and 4.8, respectively, show the liquid-liquid transitions at coexistence with the vapor phase for such a topology of the phase diagram. In both figures one finds two types of first-order liquid-liquid transitions. One between two normal liquids, which occur between *ce* and *qp*, and another one between the normal liquid phase and the superfluid liquid phase, which occur below *tce*. The points '*ce*', '*tce*', and '*qp*' in Figs. 4.7 and 4.8 correspond to the points '*c*', '*k*', and '*f*', respectively, in Fig. 4.4. The transitions between the two normal liquids correspond to the line *f-c* in Fig. 4.4, the transitions between the normal liquid and the superfluid correspond to the line *a-f* in Fig. 4.4, the small two phase region between '*tce*' and '*qp*' corresponds to the line *f-k* in Fig. 4.4, and the red line above '*tce*' corresponds to the red line emanating from '*k*' towards '*h*' in Fig. 4.4. In Fig. 4.4 the triple lines *a-f* and *k-f* merge at the quadrupole point '*qp*' = '*f*', where four phases coexist: two normal liquids, the superfluid, and the vapor phase. Below '*qp*', the liquid-liquid transitions at coexistence with the vapor phase are first-order transitions between the normal fluid and the superfluid. Upon increasing  $j_s$  the tricritical end point  $tce = k$  is pulled towards higher temperatures (compare Figs. 4.7 and 4.8).

In order to obtain phase diagrams with the topology illustrated in Fig. 4.5, one has to choose the coupling constants such that the demixing transitions at coexistence with the vapor phase occur only between the normal fluid and the superfluid. This means that in Fig. 4.4 the line *f-c* has to shrink to zero which implies that the critical point '*c*' coincides with the quadruple point '*f*'. Within Fig. 4.8(a) this means that *tce* (= *k* in Fig. 4.4) has to be pulled up to higher temperatures such that the demixing critical end point *ce* (= *c* in Fig. 4.4) slides below the quadruple *qp* (= *f* in Fig. 4.4) so that the demixing phase transition between two normal fluids becomes an unstable one within the two-phase region of the superfluid and the mixed normal fluid (see Fig. 4.9(a)). For the coupling constants  $(c/k, j/k) = (1, 5.714)$  this is fulfilled, provided that  $j_s/k > 2.96$ . For the coupling constants  $(c/k, j/k, j_s/k) = (1, 5.714, 2.96)$  at  $T_{ce}/k = 1.047$  only three thermodynamic states coexist: the critical state  $(X_{ce}, D_{ce}, M_{ce}) = (0.050, 0.913, 0)$ , the vapor phase, and a superfluid state  $(X_s, D_s, M_s) = (0.756, 0.983, 0.497)$ . Accordingly, for coupling constants  $(c/k = 1, j/k = 5.714, j_s/k > 2.96)$  one obtains the type of phase diagram shown in Figs. 4.5 and 4.9.

Note that the condition  $j_s/k > 2.96$  guarantees the correct topology of the liquid-liquid demixing transitions at coexistence with the vapor. Later in this chapter whole

#### 4. Phase diagram of fluid phases in ${}^3\text{He}$ - ${}^4\text{He}$ mixtures

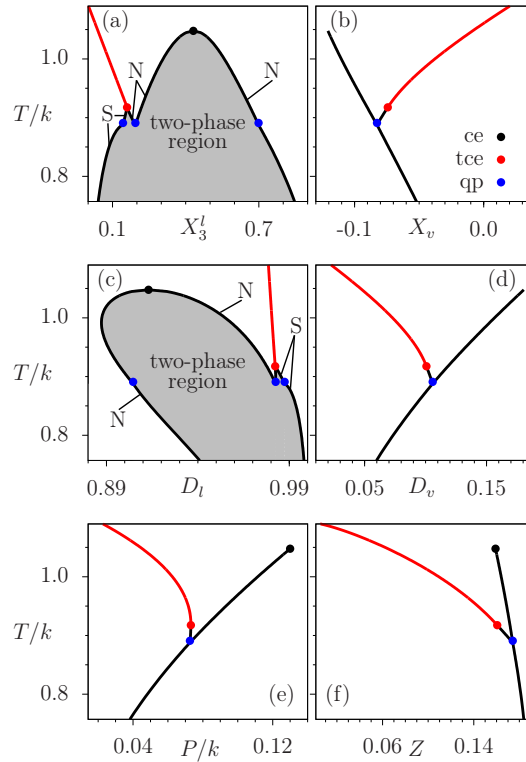


**Figure 4.7.** Phase diagram for the coupling constants  $(c/k, j/k, j_s/k) = (1, 5.714, 2.231)$  and  $H = 0$  which corresponds to Fig. 4.4. Along the triple lines a-f and f-c in Fig. 4.4 the figures show the first-order demixing transitions of the liquid phase at coexistence with the vapor phase (a) in the  $(X_3^l, T)$  plane, with  $X_3^l = \langle N_3 \rangle_l / \mathcal{N}$  as the number density of 3-particles in the liquid phase, (b) in the  $(X_v, T)$  plane at coexistence of the vapor with the two liquid phases, where  $X_v = (\langle N_4 \rangle_v - \langle N_3 \rangle_v) / \mathcal{N}$  in the vapor phase, (c) in the  $(D_l, T)$  plane, where  $D_l = (\langle N_4 \rangle_l + \langle N_3 \rangle_l) / \mathcal{N}$  in the liquid phase, and (d) in the  $(D_v, T)$  plane, where  $D_v = (\langle N_4 \rangle_v + \langle N_3 \rangle_v) / \mathcal{N}$  in the vapor phase. The indices 'l' and 'v' refer to the values of the OPs in the liquid and the vapor phase, respectively. Panels (e) and (f) show the temperature dependence of  $P$  and  $Z$  along the triple lines a-f, f-c, and f-k, in Fig. 4.4. The red line corresponds to second-order phase transitions between normal fluids and superfluids (line k-h in Fig. 4.4). At tce, the liquid state  $(X_l^{\text{tce}}, D_l^{\text{tce}}, M_l^{\text{tce}}) = (0.662, 0.982, 0)$  coexists with the vapor state  $(X_v^{\text{tce}}, D_v^{\text{tce}}, M_v^{\text{tce}}) = (-0.074, 0.100, 0)$  at  $T_{\text{tce}}/k = 0.917$ . The point 'ce' remains as in the case  $j_s = 0$ . N and S denote normal liquid and superfluid, respectively. At the quadruple point 'qp' the four coexisting states at  $T_{\text{qp}}/k = 0.887$  are two normal liquids  $(X_l^{\text{qp}}, D_l^{\text{qp}}, M_l^{\text{qp}}) = \{(-0.493, 0.904, 0), (0.594, 0.982, 0)\}$ , a superfluid  $(X_l^{\text{qp}}, D_l^{\text{qp}}, M_l^{\text{qp}}) = (0.701, 0.987, 0.281)$ , and the vapor state  $(X_v^{\text{qp}}, D_v^{\text{qp}}, M_v^{\text{qp}}) = (-0.082, 0.105, 0)$ . The points 'ce', 'tce', and 'qp' here correspond to the points 'c', 'k', and 'f', respectively in Fig. 4.4. In (b), (d), (e), and (f), the long black coexistence curves are expected to exhibit a break in slope at 'qp'; on the present scales this is not visible.

fluid parts of the phase diagram are to be obtained. Therefore, to make sure that such a topology holds even in the liquid phase away from the liquid-vapor coexistence, a higher

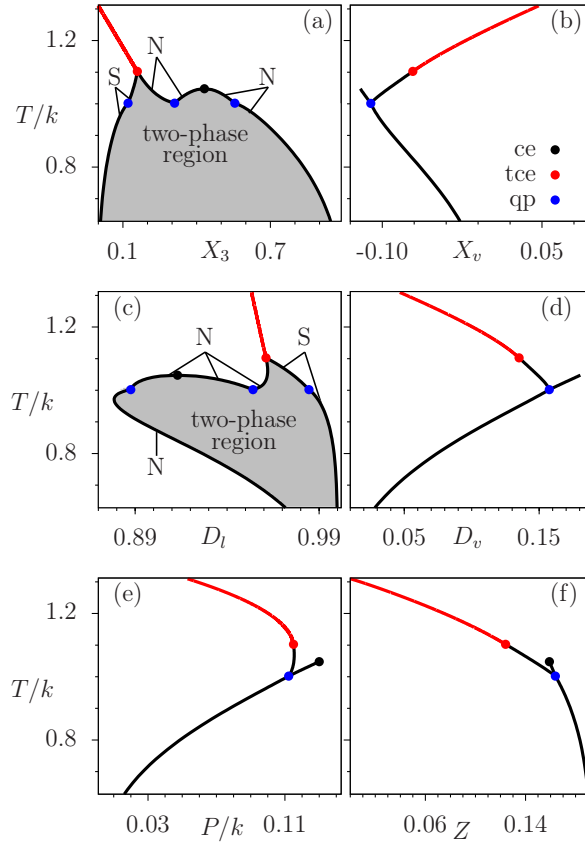


**Figure 4.8.** The same as in Fig. 4.7 but for the coupling constants  $(c/k, j/k, j_s/k) = (1, 5.714, 2.747)$  and  $H = 0$ . At tce the OPs of the liquid and the vapor phases are  $(X_l^{\text{tce}}, D_l^{\text{tce}}, M_l^{\text{tce}}) = (0.644, 0.961, 0)$  and  $(X_v^{\text{tce}}, D_v^{\text{tce}}, M_v^{\text{tce}}) = (-0.071, 0.135, 0)$ , respectively, and  $T_{\text{tce}}/k = 1.101$ . Again, ce remains as in the case of  $j_s = 0$ . N and S denote normal liquid and superfluid, respectively. The four co-existing states at the quadruple point 'qp' are given by  $(X^{\text{qp}}, D^{\text{qp}}, M^{\text{qp}}) = (-0.222, 0.888, 0), (0.334, 0.954, 0), (0.742, 0.984, 0.456),$  and  $(0.110, 0.157, 0)$  at the temperature  $T_{\text{qp}}/k = 1.001$ . The long black lines in (b) and (d) and the ones in (e) and (f) ending at 'ce' are expected to exhibit a break in slope at 'qp'; on the present scales this is not visible.

value  $j_s/k = 3.674$  is chosen in this chapter (see Fig. 4.9).

As can be inferred from Fig. 4.9(f), upon increasing the temperature, the line of second-order phase transitions to the superfluid phase (red line) approaches the plane  $Z = 0$ , where the liquid becomes pure  $^4\text{He}$ . In order to explore the phase diagram in the plane  $Z = 0$ , in Eqs. (4.17) - (4.21) one has to take the limit  $\mu_3 \rightarrow -\infty$ . In this limit  $\mu_- \rightarrow +\infty$  and  $\mu_+ \rightarrow -\infty$  so that  $W$  and  $R$  turn into

$$\lim_{\mu_3 \rightarrow -\infty} W(\mu_-, \mu_+, H, T) = 0, \quad (4.43)$$

#### 4. Phase diagram of fluid phases in $^3\text{He}$ - $^4\text{He}$ mixtures

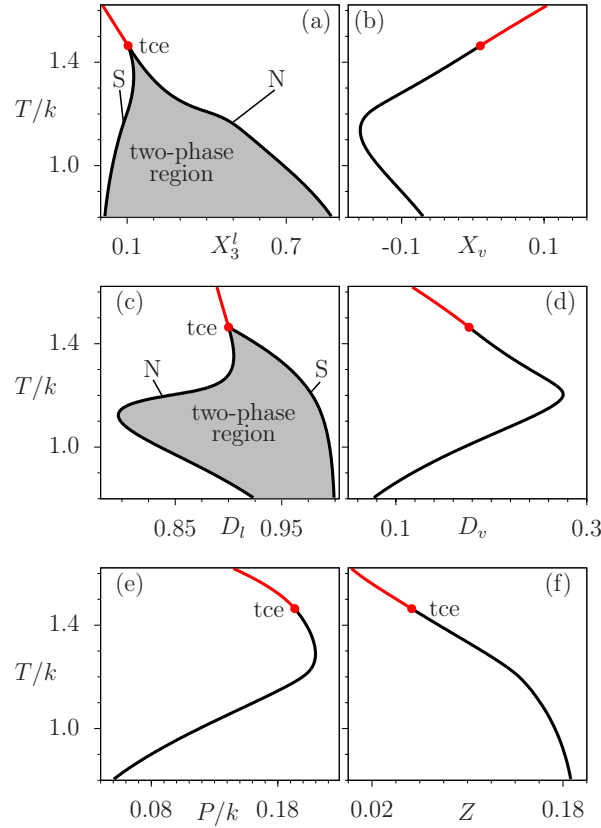


**Figure 4.9.** Phase diagrams for the coupling constants  $(c/k, j/k, j_s/k) = (1, 5.714, 3.674)$  and  $H = 0$ , corresponding to Fig. 4.5. The panels show the same as in Figs. 4.7 and 4.8; however the critical end point 'ce' has disappeared. At tce the liquid state  $(X_l^{\text{tce}}, D_l^{\text{tce}}, M_l^{\text{tce}}) = (0.693, 0.900, 0)$  coexists with the vapor state  $(X_v^{\text{tce}}, D_v^{\text{tce}}, M_v^{\text{tce}}) = (0.010, 0.176, 0)$  at  $T_{\text{tce}}/k = 1.462$ . For  $T > T_{\text{tce}}$  there is only a second-order phase transition from a normal mixed liquid to a superfluid. For  $T < T_{\text{tce}}$  the phase transitions between the normal fluid and the superfluid are first order. N and S denote normal liquids and superfluids, respectively.

and due to  $\mu_- + \mu_+ = \mu_4$

$$\lim_{\mu_3 \rightarrow -\infty} R(\mu_-, \mu_+, H, T) = e^{\beta((c+k)X + (j+c)D + \mu_4)}. \quad (4.44)$$

Since  $W_{\mu_3 \rightarrow -\infty} = 0$ , due to Eqs. (4.17) and (4.18) one has  $X_{\mu_3 \rightarrow -\infty} = D_{\mu_3 \rightarrow -\infty}$ , where  $D_{\mu_3 \rightarrow -\infty}$  is given by

$$\begin{aligned} D_{\mu_3 \rightarrow -\infty} &= \lim_{\mu_3 \rightarrow -\infty} \frac{R(\mu_-, \mu_+, H, T) I_0(j_s M/T + H/T)}{1 + R(\mu_-, \mu_+, H, T) I_0(j_s M/T + H/T)} \\ &= \frac{e^{\beta((j+k+2c)D + \mu_4)} I_0(j_s M/T + H/T)}{1 + e^{\beta((j+k+2c)D + \mu_4)} I_0(j_s M/T + H/T)}, \end{aligned} \quad (4.45)$$

where, due to  $X_{\mu_3 \rightarrow -\infty} = D_{\mu_3 \rightarrow -\infty}$ , in  $R_{\mu_3 \rightarrow -\infty}$  the order parameter  $X$  is replaced by  $D$ .

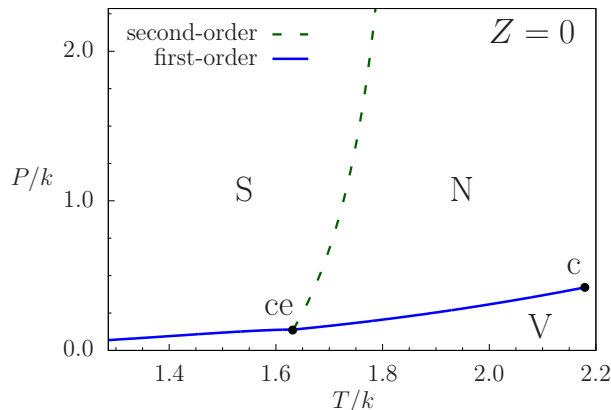


**Figure 4.10.** The  $(T, P)$  phase diagram for the coupling constants  $(c/k, j/k, j_s/k) = (1, 5.714, 3.674)$  and  $H = 0$  for pure  ${}^4\text{He}$ , i. e.,  $Z = 0$ . The dashed green line shows the  $\lambda$ -line of second-order phase transitions between normal liquids and superfluids. N, S, and V denote the normal liquid, the superfluid, and the vapor phase, respectively. The blue line of first-order liquid-vapor transitions terminates the  $\lambda$ -line at the critical end point 'ce' and ends at the critical point 'c' of the liquid-vapor coexistence line. (A set of coupling constants could not be found for which the dashed  $\lambda$ -line of second-order phase transitions exhibits a negative slope as it is the case for actual  ${}^4\text{He}$ .)

In this limit Eq. (4.29) reduces to

$$\frac{D}{M} = \frac{I_0(j_s M/T + H/T)}{I_1(j_s M/T + H/T)} \quad (4.46)$$

and the equilibrium free energy (Eq. (4.22)) reduces to

$$\phi(\mu_3 \rightarrow -\infty, \mu_4, H, T) = \mathcal{N} \left[ \frac{k + j + 2c}{2} D^2 + \frac{j_s}{2} M^2 + T \ln(1 - D) \right]. \quad (4.47)$$

In this limit the temperature of the superfluid transition is given by

$$T_s = \frac{j_s}{2} D, \quad (4.48)$$

and  $\mu_4$  follows from Eq. (4.45):

$$\mu_4(H, T) = T \ln \frac{D}{1 - D} - (j + 2c + k)D - T \ln I_0(j_s M/T + H/T). \quad (4.49)$$

For pure  ${}^4\text{He}$  (i. e.,  $Z = 0$ ) and for the choice of the coupling constants  $(c/k, j/k, j_s/k) = (1, 5.714, 3.674)$ , the phase diagram in the  $(T, P)$  plane is shown in Fig. 4.10. The dashed green line shows the  $\lambda$ -line of second-order phase transitions between normal liquids and superfluids. This line is terminated by the line of first-order liquid-vapor phase transitions (blue line) at the critical end point ce. The line of first-order liquid-vapor phase

#### 4. Phase diagram of fluid phases in $^3\text{He}$ - $^4\text{He}$ mixtures

---

transitions ends at the critical point  $c$ . For high pressures the system becomes solid, (see Fig. 3.1) which, however, is not captured by the present model. Along the line of first-order liquid–vapor transitions ( $T > T_{ce}$ , blue line in Fig. 4.10), the difference between the number densities of the liquid and the vapor phase decreases upon increasing the temperature and vanishes at  $T = T_c$ . Accordingly, the two phases merge into a single phase at the critical point ‘ $c$ ’ given by

$$\left. \frac{d\mu_4}{dD} \right|_T = \left. \frac{d^2\mu_4}{dD^2} \right|_T = 0, \quad \left. \frac{d^3\mu_4}{dD^3} \right|_T > 0, \quad (4.50)$$

where  $\mu_4$  is given by Eq. (4.49). These conditions reduce to (note that  $I_0(0) = 1$ )

$$D_c = 0.5, \quad T_c = 0.25(2c + j + k). \quad (4.51)$$

For nonzero values of  $Z$ , i.e., in the presence of  $^3\text{He}$  atoms, the critical points of the phase transitions between vapor and normal liquids ( $M = 0$ ) are given by (see Eqs. (4.5) and (4.27))

$$\left. \frac{d\mu_+}{dD} \right|_{\mu_-, T} = \left. \frac{d^2\mu_+}{dD^2} \right|_{\mu_-, T} = 0, \quad \left. \frac{d^3\mu_+}{dD^3} \right|_{\mu_-, T} > 0, \quad (4.52)$$

where in Eq. (4.27) also the partial derivatives of  $X$  with respect to  $D$  must be taken into account.

Having determined various features of the phase diagram of the present model for a set of coupling constants for which the topology of the phase diagram is that of the experimental one, it is possible to illustrate quantitatively the phase diagram in the  $(P, Z, T)$  space. The phase diagram, which — for a suitable set of coupling constants — resembles the schematic phase diagram proposed in Ref. [20] and exhibits all relevant fluid phases, is given in Fig. 4.11 (compare Fig. 3.3). Accordingly, Fig. 4.11 shows where the vapor phase (V), the normal liquid phase (N), and the superfluid phase are thermodynamically stable and where first- or second-order phase transitions among each other occur. The transitions between the vapor and the liquid phases are given by the two surfaces  $o$ - $ce$ - $tce$ - $b$ - $b''$ - $o$  and  $ce$ - $c'$ - $b$ - $tce$ - $ce$  (the union of which corresponds to  $A_2$  in Fig. 3.3), while the loci of the phase transitions between the superfluid and the normal fluid form the two surfaces  $b$ - $tce$ - $t$ - $b'$ - $b$  and  $tce$ - $ce$ - $c''$ - $t$ - $tce$  which in Fig. 3.3, correspond to  $A_4$  and  $A_3$ , respectively. The points  $o$ ,  $ce$ ,  $c$ , and  $c''$  lie in the zero fugacity plane ( $Z = 0$ ) whereas  $b'$ ,  $t$ , and  $c''$  lie in the plane of constant pressure  $P/k = 0.560$ . The points  $b''$  and  $o$  are located in the plane of constant temperature  $T/k = 1.071$ , while  $b$ ,  $b'$ ,  $b''$ , and  $c'$  share the same value of fugacity  $Z = 0.139$ . The black line  $b$ - $tce$  and the light red line  $tce$ - $ce$  indicate first- and second-order liquid–liquid phase transitions, respectively, at coexistence with the vapor phase. These two lines are connected at the tricritical end point  $tce$ . The dark red solid line ( $tce$ - $t$ ) connects the surfaces  $A_4$  and

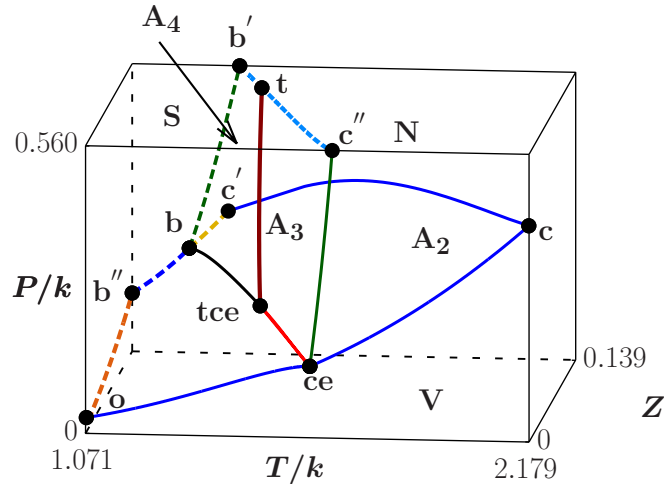


**Figure 4.11.** Numerical results for the fluid parts of the phase diagram for the choice of the coupling constants  $(c/k, j/k, j_s/k) = (1, 5.714, 3.674)$  and  $H = 0$  in  $(P, Z, T)$  space. The points  $o$ ,  $ce$ ,  $c$ , and  $c''$  lie in the zero fugacity plane ( $Z = 0$ ) and the points  $c''$ ,  $t$ , and  $b'$  lie in the constant pressure plane  $P/k = 0.560$ . The points  $o$  and  $b''$  have the same temperature  $T/k = 1.071$ , while  $b$ ,  $b'$ , and  $c'$  share the same value of the fugacity  $Z = 0.139$ . The surface  $(o-ce-tce-b-b''-o)$  corresponds to first-order phase transitions between the vapor phase (V) and the superfluid phase (S), whereas  $(ce-c-c'-b-tce-ce)$  is the surface of first-order phase transitions between the vapor phase and the normal liquid phase (N); their union corresponds to  $A_2$  in Fig. 3.3. The surface  $(b-tce-t-b'-b)$  is the surface of first-order phase transitions between the superfluid and the normal liquid phase corresponding to  $A_4$  in Fig. 3.3 and  $(tce-ce-c''-t-tce)$  is the surface of second-order phase transitions between the superfluid and the normal liquid phase corresponding to  $A_3$  in Fig. 3.3. The black line  $b-tce$  and the light red line  $tce-ce$  are the lines of first- and second-order liquid-liquid transitions at coexistence with the vapor phase, respectively, which meet at the tricritical end point  $tce$ . The solid blue line  $c-c'$  is the line of critical points of the liquid-vapor phase transitions and the dark red curve  $(tce-t)$  is the line of tricritical points. The lowest pressure is  $p/k = 0$  whereas the highest temperature is  $T/k = 2.179$ . The line  $o-b''$  is the intersection of  $A_2$  and the plane  $T/k = 1.071$ , the line  $c'-b-b''$  is the intersection of  $A_2$  and the plane  $Z = 0.139$ ; the line  $b-b'$  is the intersection of  $A_4$  with the plane  $Z = 0.139$ ; the line  $b'-t$  and  $t-c''$  are the intersection of  $A_4$  and  $A_3$ , respectively, with the plane  $P/k = 0.560$ . Note that at ' $ce$ ' the line  $o-ce-c$  does not exhibit a break in slope (see Fig. 4.10).

$A_3$  of first- and second-order liquid-liquid phase transitions  $((b-b'-t-tce-b)$  and  $(t-tce-ce-c''-t)$ ), respectively. The coexisting states along the two lines  $(b-tce, T < T_{tce})$  and  $(tce-ce, T > T_{tce})$  are the ones shown in Fig. 4.9. The solid blue line  $(c-c')$  is the line of critical points of the liquid-vapor phase transitions and the dark red curve  $(tce-t)$  is the line of tricritical points with the tricritical end point  $tce$ .

By moving along the line  $b-b''$  towards  $b''$  the number density in the liquid phase

#### 4. Phase diagram of fluid phases in $^3\text{He}$ - $^4\text{He}$ mixtures

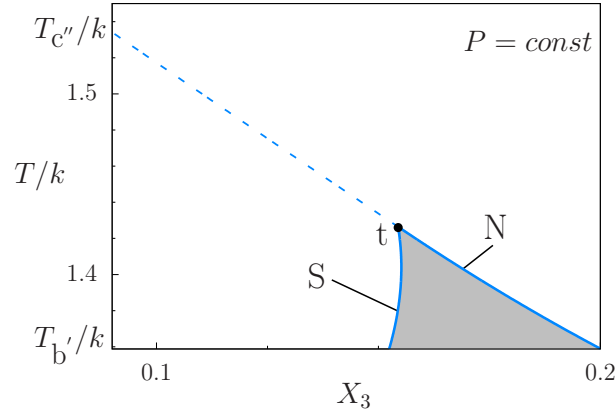


**Figure 4.12.** Liquid–liquid phase transitions at fixed pressure  $P/k = 0.560$  in the  $(X_3, T)$  plane for the choice of the coupling constants  $(c/k, j/k, j_s/k) = (1, 5.714, 3.674)$  and  $H = 0$ . The figure provides the temperature dependence of  $X_3$  along the line  $b'-t-c''$  in Fig. 4.11. For  $T_t < T < T_{c''}$  the light blue dashed line represents continuous phase transitions whereas for  $T_{b'} < T < T_t$  the lines indicate the coexisting superfluid (S) and normal liquid (N) states at first–order phase transitions. The two–phase region is shaded in grey. The point  $t$  corresponds to a tricritical point.

increases. This implies that the larger the number density of the liquid phase at  $b$  is, the shorter is the line  $b-b''$  (note that  $D < 1$ ). This means that, by lowering the temperature along the line of first–order liquid–liquid phase transitions at coexistence with the vapor phase ( $tce-b$ ), the point  $b$  shifts towards the point  $b''$ .

The liquid–liquid phase transitions at constant pressure are given by the curve  $b'-t-c''$ . The curve  $(b'-t)$  is a line of first–order liquid–liquid phase transitions at constant pressure, which is connected to the line of second–order liquid transitions ( $t-c''$ ) at the tricritical point  $t$ . The coexisting states along these two lines are shown in Fig. 4.12. For even higher pressures the system solidifies, and the two surfaces  $(A_4, b-tce-t-b'-b)$  and  $(A_3, tce-ce-c''-t-tce)$  should continue towards a surface of first–order liquid–solid phase transitions (see  $A_1$  in Fig. 3.3) which is not supported by the present model.

## 5. Tricritical Casimir forces in $^3\text{He}$ - $^4\text{He}$ wetting films

The goal of this chapter is to calculate tricritical Casimir forces (TCFs) in wetting films of  $^3\text{He}$  -  $^4\text{He}$  mixtures. As discussed in Introduction, previous corresponding theoretical analysis [24, 25] do not consider a self-consistent formation of wetting film and replace it by fiat with a slab of constant thickness. In the present chapter it is aimed to improve this description and to provide a theoretical framework which describes the actual experimental conditions of the corresponding measurements as carried out in Ref. [17]. In these measurements TCF has been determined indirectly by monitoring the wetting film thickness. Accordingly, a  $^3\text{He}$  -  $^4\text{He}$  mixture was prepared in a thermodynamic state at liquid-vapor coexistence such that a complete wetting film was grown at the plates of a capacitor. Then, the equilibrium thickness of this wetting film was determined very accurately from capacitance measurements. Finally, from the balance of the effective forces acting on the liquid-vapor interface the universal scaling function of the TCF was determined. The difference between the actual experimental condition and the approach in Refs. [24, 25] is borne out in Fig. 5.1. Therein the surface of constant total density  $D(P, T, Z) = \text{const.}$  is shown in blue. The analyses in Refs. [24, 25] have been carried out within such a surface, whereas the experiment in Ref. [17] has been carried out along the surface  $A_2$  of liquid-vapor coexistence. Note that, although in the experiments the thermodynamic states have been tuned to their values at liquid-vapor coexistence such that complete wetting occurred, due to gravity the wetting films have remained finite which means that, the actual thermodynamic paths lie on a surface, which is located slightly in the vapor phase (brown surface in Fig. 5.1). Figures 5.2 and 5.3 show these thermodynamic paths.

In order to pave the way for providing a more realistic description of the experimental setup reported in Ref. [17], in the previous chapter a model has been proposed such that the vapor phase is incorporated into the phase diagram. In the present chapter this model is modified and a semi-infinite lattice gas model is proposed. The model proposed

---

This chapter is reprinted with permission from [N. Farahmand Bafi, A. Maciolek, and S. Dietrich, Phys. Rev. E **95**, 032802 (2017).] Copyright 2017 by the American Physical Society.

## 5. Tricritical Casimir forces in $^3\text{He}$ - $^4\text{He}$ wetting films

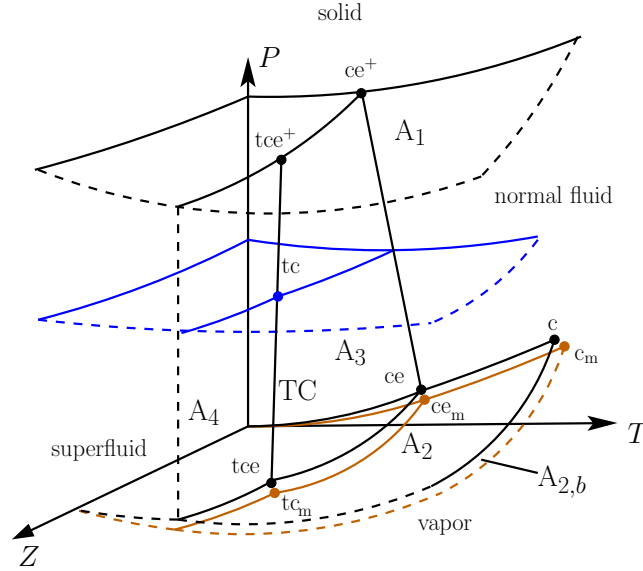


**Figure 5.1.** Schematic phase diagram of  $^3\text{He}$  -  $^4\text{He}$  mixtures as in Fig. 3.3 [20] (black curves and surfaces) and two specific surfaces (blue and brown) in the  $(T, Z, P)$  space, where  $P$  is the pressure and  $Z = \exp(\mu_3/T)$  is the fugacity of  $^3\text{He}$ , with  $\mu_3$  being the chemical potential of  $^3\text{He}$  atoms. See the caption of Fig. 3.3 for the details of the bulk phase diagram. On the blue surface the total density is constant, which corresponds to the situation studied in Refs. [24, 25]. The brown surface  $A_{2,b}$  lies in the vapor phase slightly below the liquid–vapor coexistence surface  $A_2$ . Although the thermodynamic fields along the thermodynamic paths taken in the experiment in Ref. [17] have been tuned to their values at the liquid–vapor coexistence surface, due to gravity the actual measurements have been carried out for thermodynamic states which lie on a surface resembling the brown one. At the thermodynamic states on the brown surface, in addition to the stable vapor phase, there are metastable liquid phases. These metastable liquid phases undergo transitions similar to the liquid–liquid phase transitions tied to  $A_2$ . Therefore, for each point  $tce$ ,  $ce$ , and  $c$ , there is a metastable counterpart  $tc_m$ ,  $ce_m$ , and  $c_m$ , respectively, on the brown surface.

here includes two surface fields, which couple to the number densities of  $^3\text{He}$  and  $^4\text{He}$ . These fields enable the model to exhibit wetting and thus provide a proper framework for studying TCFs in wetting films of  $^3\text{He}$  -  $^4\text{He}$  mixtures. In the present analysis the effect of gravity on the wetting films is mimicked by an offset from the liquid–vapor coexistence such that the thermodynamic paths lie on a surface similar to the brown one in Fig. 5.1.

In the next section the model is proposed and mean field approximation is applied to it (Sec. 5.1). Then the bulk limiting case of the model is studied, which renders the model in chapter 4. As will be discussed in Subsec. 5.1.2, although in the previous chapter the set of coupling constants has been identified for which the bulk phase diagram has the same topology as in  $^3\text{He}$  -  $^4\text{He}$  mixtures, in the following chapter one has

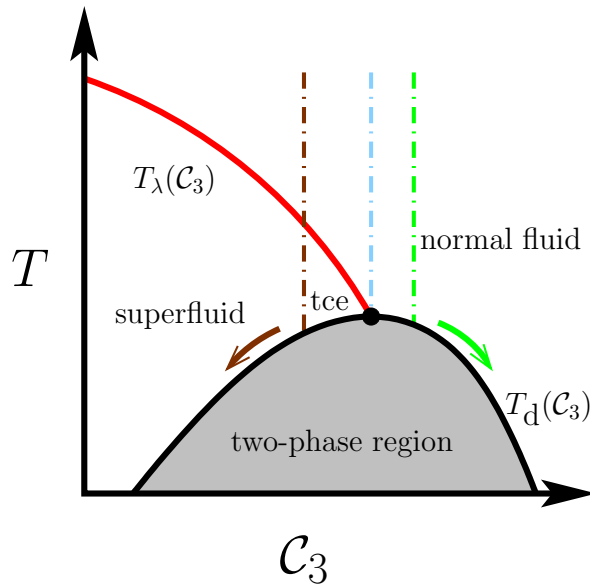


**Figure 5.2.** Liquid–liquid bulk phase transitions at coexistence with the vapor phase for  ${}^3\text{He}$ - ${}^4\text{He}$  mixtures [20] and the thermodynamic paths taken in the experiments reported in Ref. [17]. The black curves denote the first–order phase transitions between the normal fluid phase and the superfluid phase, which terminate at the tricritical end point tce. The red curve shows the second–order  $\lambda$ -transitions between the normal fluid phase and the superfluid phase. The dashed dotted lines indicate three distinct thermodynamic paths corresponding to three fixed values of the concentration  $\mathcal{C}_3 = X_3/(X_3 + X_4)$  (see, cf., Eq. (5.17)) of the  ${}^3\text{He}$  atoms as done experimentally.  $X_3$  and  $X_4$  are the bulk number densities of  ${}^3\text{He}$  and  ${}^4\text{He}$ , respectively. Upon decreasing the temperature, the bulk liquid undergoes a first–order phase separation at some demixing temperature  $T_d(\mathcal{C}_3)$ . Upon further decrease of the temperature the thermodynamic paths follow that branch of the coexistence curve, which they hit (see the brown and the green arrows).

to consider slightly different coupling constants. In Sec. 5.2 short–ranged surface fields are considered and the wetting behavior of the model is studied for the case of classical binary liquid mixtures. Then, by considering the proper set of coupling constants the experimental results of the thickness measurements of  ${}^3\text{He}$ - ${}^4\text{He}$  wetting films are reproduced and finally, the TCF and its scaling function is calculated. Note that the mean field approximation used here captures the universal behavior of the TCF near the tricritical point of  ${}^4\text{He}$ - ${}^4\text{He}$  mixtures in the film up to the logarithmic corrections because for the tricritical phenomena the upper critical dimension  $d^* = 3$ . However, this description is not sufficient at the critical points of the  $\lambda$ -transition because the upper critical dimension for critical phenomena  $d^* = 4$ .



responding interaction strength (see, cf., Eq. (5.4)). The effective interactions between pairs of helium isotopes are represented by  $J_{33}$ ,  $J_{44}$ , and  $J_{34}$ . As discussed in the previous chapter, the three effective pair potentials between the two types of isotopes are not identical due to their distinct statistics and the slight differences in their electronic states. The surface fields, which represent the effective interaction between the surface and the  $^4\text{He}$  and  $^3\text{He}$  atoms, are denoted as  $f_4(l)$  and  $f_3(l)$ , respectively. In general these surface fields depend on the distance  $l$  from the surface, which is located at  $l = 0$ , and vanish for large  $l$ . The chemical potential of species  $^m\text{He}$  is denoted as  $\mu_m$ . (The Hamiltonian in Eq. (5.1)) with  $J_s = 0$  describes a classical binary liquid mixture of species  $m$  and  $n$ .)

In order to proceed, one can associate an occupation variable  $s_i$  with each lattice site  $\{i\}$ , which can take the three values  $+1$ ,  $-1$ , or  $0$ , where  $+1$  denotes that the lattice site is occupied by  $^4\text{He}$ ,  $-1$  denotes that the lattice site is occupied by  $^3\text{He}$ , and  $0$  denotes that the lattice site is unoccupied.  $N_m$  and  $N_{mn}$  can be expressed in terms of  $\{s_i\}$  as follows:

$$\begin{aligned}
 N_4 &= \frac{1}{2} \sum_i s_i(s_i + 1) \equiv \sum_i p_i, \\
 N_3 &= \frac{1}{2} \sum_i s_i(s_i - 1), \\
 N_{44} &= \frac{1}{4} \sum_{\langle i,j \rangle} (s_i(s_i + 1)s_j(s_j + 1)) \equiv \sum_{\langle i,j \rangle} p_i p_j, \\
 N_{33} &= \frac{1}{4} \sum_{\langle i,j \rangle} (s_i(s_i - 1)s_j(s_j - 1)), \\
 N_{34} &= \frac{1}{4} \sum_{\langle i,j \rangle} (s_i(s_i + 1)s_j(s_j - 1) + s_i(s_i - 1)s_j(s_j + 1)),
 \end{aligned} \tag{5.2}$$

where  $\sum_{\langle i,j \rangle}$  denotes the sum over nearest neighbors. Using the above definitions one obtains

$$\begin{aligned}
 \mathcal{H} &= -K \sum_{\langle i,j \rangle} s_i s_j - J \sum_{\langle i,j \rangle} q_i q_j - C \sum_{\langle i,j \rangle} (s_i q_j + q_i s_j) \\
 &\quad - \mu_- \sum_i s_i - \mu_+ \sum_i q_i - \sum_i f_-(l) s_i - \sum_i f_+(l) q_i \\
 &\quad - J_s \sum_{\langle i,j \rangle} p_i p_j \cos(\Theta_i - \Theta_j),
 \end{aligned} \tag{5.3}$$

where

$$\sum_{\langle i,j \rangle} p_i p_j \cos(\Theta_i - \Theta_j) = \tilde{N}_{44} = \sum_{\langle i,j \rangle} p_i p_j \begin{pmatrix} \cos \Theta_i \\ \sin \Theta_i \end{pmatrix} \cdot \begin{pmatrix} \cos \Theta_j \\ \sin \Theta_j \end{pmatrix}, \tag{5.4}$$

## 5. Tricritical Casimir forces in $^3\text{He}$ - $^4\text{He}$ wetting films

---

and

$$\begin{aligned}
q_i &= s_i^2, \\
p_i &= \frac{1}{2}s_i(s_i + 1), \\
K &= \frac{1}{4}(J_{44} + J_{33} - 2J_{34}), \\
J &= \frac{1}{4}(J_{44} + J_{33} + 2J_{34}), \\
C &= \frac{1}{4}(J_{44} - J_{33}), \\
\mu_- &= \frac{1}{2}(\mu_4 - \mu_3), \\
\mu_+ &= \frac{1}{2}(\mu_4 + \mu_3), \\
f_+(l) &= \frac{1}{2}(f_4(l) + f_3(l)), \\
f_-(l) &= \frac{1}{2}(f_4(l) - f_3(l)).
\end{aligned} \tag{5.5}$$

$\Theta_i \in [0, 2\pi]$  represents the superfluid degree of freedom at the lattice site  $i$ , provided it is occupied by  $^4\text{He}$ .

### 5.1.1. Mean field approximation

In this section a mean field approximation for the present model is carried out (for details of the calculations see Appendix B). The symmetry of the problem implies that all statistical quantities exhibit the same mean values for all lattice sites within a layer, in particular the same mean field generated by their neighborhood. Therefore all quantities depend only on the distance  $l$  of a layer from the surface. (Note that  $l$  is an integer which not only represents the position of the layer but also marks the corresponding layer.) Accordingly, the dimensionless OPs are:

$$\begin{aligned}
X_l &:= \langle s_{(l,v_l)} \rangle, \\
D_l &:= \langle q_{(l,v_l)} \rangle, \\
M_l^2 &:= \langle p_{(l,v_l)} \sin \Theta_{(l,v_l)} \rangle^2 + \langle p_{(l,v_l)} \cos \Theta_{(l,v_l)} \rangle^2,
\end{aligned} \tag{5.6}$$

which are coupled by the following self-consistent equations:

$$X_l = \frac{-W_l + R_l I_0(\beta J_s \tilde{M}_l)}{1 + W_l + R_l I_0(\beta J_s \tilde{M}_l)}, \tag{5.7}$$

$$D_l = \frac{W_l + R_l I_0(\beta J_s \tilde{M}_l)}{1 + W_l + R_l I_0(\beta J_s \tilde{M}_l)}, \tag{5.8}$$

and

$$M_l = \frac{R_l I_1(\beta J_s \tilde{M}_l)}{1 + W_l + R_l I_0(\beta J_s \tilde{M}_l)}, \quad (5.9)$$

where  $\beta = 1/T$  with  $T$  as temperature times  $k_B$ ,  $I_0(\beta J_s \tilde{M}_l)$  and  $I_1(\beta J_s \tilde{M}_l)$  are modified Bessel functions, and

$$\tilde{M}_l = (1 - \delta_{l,0})M_{l-1} + 4M_l + M_{l+1}. \quad (5.10)$$

The dimensionless functions  $W_l$  and  $R_l$  depend on the following set of parameters:  $(X_l, D_l; \mu_-, \mu_+, f_+(l), f_-(l), T)$ . They are given by

$$\begin{aligned} W_l(X_l, D_l; \mu_-, \mu_+, f_+(l), f_-(l), T) = \exp \left[ \beta \{ (J - C)(D_{l-1}(1 - \delta_{l,0}) + 4D_l + D_{l+1}) \right. \\ \left. + (C - K)(X_{l-1}(1 - \delta_{l,0}) + 4X_l + X_{l+1}) \right. \\ \left. + \mu_+ + f_+(l) - \mu_- - f_-(l) \} \right] \end{aligned} \quad (5.11)$$

and

$$\begin{aligned} R_l(X_l, D_l; \mu_-, \mu_+, f_+(l), f_-(l), T) = \exp \left[ \beta \{ (J + C)(D_{l-1}(1 - \delta_{l,0}) + 4D_l + D_{l+1}) \right. \\ \left. + (C + K)(X_{l-1}(1 - \delta_{l,0}) + 4X_l + X_{l+1}) \right. \\ \left. + \mu_+ + f_+(l) + \mu_- + f_-(l) \} \right]. \end{aligned} \quad (5.12)$$

Accordingly, the equilibrium free energy per number of lattice sites in a single layer is given by

$$\begin{aligned} \phi/\mathcal{N} = \sum_{l=0}^{L-1} \left[ \frac{K}{2} X_l (4X_l + X_{l+1} + X_{l-1}(1 - \delta_{l,0})) \right. \\ \left. + \frac{J}{2} D_l (4D_l + D_{l+1} + D_{l-1}(1 - \delta_{l,0})) \right. \\ \left. + \frac{C}{2} X_l (4D_l + D_{l+1} + D_{l-1}(1 - \delta_{l,0})) \right. \\ \left. + \frac{C}{2} D_l (4X_l + X_{l+1} + X_{l-1}(1 - \delta_{l,0})) \right. \\ \left. + \frac{J_s}{2} M_l (4M_l + M_{l+1} + M_{l-1}(1 - \delta_{l,0})) \right. \\ \left. + (1/\beta) \ln(1 - D_l) \right]. \end{aligned} \quad (5.13)$$

Within the grand-canonical ensemble the pressure is  $P = -\phi/V$ , where here the volume is  $V = L\mathcal{N}a$ , with  $a = 1$ . The functional form of the expressions for the chemical

## 5. Tricritical Casimir forces in $^3\text{He}$ - $^4\text{He}$ wetting films

---

potentials are obtained by solving Eqs. (5.7) and (5.8) for them (see Appendix B):

$$\begin{aligned} \mu_+ = & \frac{T}{2} \ln(D_l^2 - X_l^2) - T \ln 2 - T \ln(1 - D_l) - \frac{T}{2} \ln(I_0(\beta J_s \tilde{M}_l)) \\ & - J(D_{l-1}(1 - \delta_{l,0}) + 4D_l + D_{l+1}) - C(X_{l-1}(1 - \delta_{l,0}) + 4X_l + X_{l+1}) - f_+(l), \end{aligned} \quad (5.14)$$

and

$$\begin{aligned} \mu_- = & \frac{T}{2} \ln \frac{D_l + X_l}{D_l - X_l} - \frac{T}{2} \ln(I_0(\beta J_s \tilde{M}_l)) \\ & - C(D_{l-1}(1 - \delta_{l,0}) + 4D_l + D_{l+1}) - K(X_{l-1}(1 - \delta_{l,0}) + 4X_l + X_{l+1}) - f_-(l). \end{aligned} \quad (5.15)$$

Finally, one can express the magnetization  $M_l$  in terms of  $X_l$  and  $D_l$  by using Eqs. (5.7) - (5.9):

$$\frac{X_l + D_l}{2} = \frac{M_l I_0(\beta J_s \tilde{M}_l)}{I_1(\beta J_s \tilde{M}_l)}. \quad (5.16)$$

According to the definition of the OPs in Eq. (5.6) and by using Eqs. (5.2) and (B.7) one can express the number densities of species  $^4\text{He}$  and  $^3\text{He}$  in the  $l^{\text{th}}$  layer as

$$\begin{aligned} X_{4,l} = & \frac{\langle N_{4,l} \rangle}{\mathcal{N}} = \langle p_l \rangle = \frac{1}{2} \langle s_l(s_l + 1) \rangle = \frac{D_l + X_l}{2}, \\ X_{3,l} = & \frac{\langle N_{3,l} \rangle}{\mathcal{N}} = \frac{1}{2} \langle s_l(s_l - 1) \rangle = \frac{D_l - X_l}{2}, \end{aligned} \quad (5.17)$$

so that  $D_l = X_{4,l} + X_{3,l} = \langle s_l^2 \rangle$  and  $X_l = X_{4,l} - X_{3,l} = \langle s_l \rangle$ , where  $s_l \equiv s_{(l,v_l)}$  is the occupation variable of a single lattice site within the  $l^{\text{th}}$  layer; its thermal average is independent of  $v_l$  (see Appendix B). Accordingly, the concentration of the two species in the  $l^{\text{th}}$  layer is given by  $\mathcal{C}_{4,l} \equiv \frac{X_{4,l}}{X_{4,l} + X_{3,l}} = \frac{D_l + X_l}{2D_l}$  and  $\mathcal{C}_{3,l} \equiv \frac{X_{3,l}}{X_{4,l} + X_{3,l}} = \frac{D_l - X_l}{2D_l}$ .

In order to study wetting films at given values of  $(T, \mu_+, \mu_-)$ , one has to solve the set of equations given by Eqs. (5.14) - (5.16) for the set of OPs  $\{(X_l, D_l, M_l) | l = 0, \dots, L - 1\}$ . This has been done numerically by using the GSL library [118, 119] and Mathematica software [116, 117]. Since for the last layer  $l = L - 1$  Eqs. (5.14) - (5.16) request OP values at  $l = L$ , one has to assign values to  $(X_L, D_L, M_L)$ . If the system size  $L$  is sufficiently large one expects that far away from the surface the OP profiles attain their bulk values. This implies  $(X_L, D_L, M_L) = (X_{\text{bulk}}, D_{\text{bulk}}, M_{\text{bulk}})$ . The system size  $L$  can be considered to be large enough if the OP profiles  $(X_l, D_l, M_l)$  remain de facto unchanged upon increasing  $L$  (which mimics a semi-infinite system). The minimization procedure, which leads to Eqs. (5.14) - (5.16) does not involve the second derivative of  $\phi$  with respect to the trial density matrix  $\rho_l$  (see Appendix B). Therefore, depending on the initial profile  $\{(X_l, D_l, M_l) | l = 0, \dots, L - 1\}$ , with which one starts the iteration algorithm, the solution of Eqs. (5.14) - (5.16) might correspond to a local minimum, a local maximum, or a saddle point.

### 5.1.2. Limiting case: bulk phase diagram

Taking the OPs to be independent of  $l$  and omitting the surface fields, i.e.,  $f_+(l) = f_-(l) = 0$ , Eqs. (5.7) - (5.9), and Eqs. (5.14) - (5.16), together with the expression for the equilibrium free energy given by Eq. (5.13), render the bulk phase diagram of the system as studied in the previous chapter. There it has been demonstrated (see also Ref. [113]) that various coupling constants lead to diverse topologies of the phase diagram for the bulk liquid–liquid demixing transitions. The topologies discussed in the previous chapter range from the phase diagram of a classical binary mixture (Fig. 5.4(a)) to a phase diagram which to a large extent resembles the actual one of  $^3\text{He}$ – $^4\text{He}$  mixtures (Fig. 5.4(b)). In chapter 4 it has also been discussed how within the proposed model, for a suitable value of  $J_s$  the bulk phase diagram of a classical binary mixture with specific values of  $(C_0/K_0, J_0/K_0)$  and for  $J_s = 0$  (dotted curve in Fig. 5.5) transforms into that of the  $^3\text{He}$ – $^4\text{He}$  mixture. Figure 5.5 illustrates schematically this transformation. One has to find and to adopt a nonzero value of  $J_s = J_s^0$  such that the critical end point ce of the phase diagram for  $(C_0/K_0, J_0/K_0, J_s = 0)$  is in thermodynamic coexistence with a superfluid phase. This locates the critical end point ce on the right shoulder of the transformed phase diagram. Thus for  $J_s > J_s^0$ , the initial phase diagram for  $(C_0/K_0, J_0/K_0, J_s = 0)$  (including its critical end point ce), lies in the two–phase region of the phase diagram for  $(C_0/K_0, J_0/K_0, J_s > J_s^0)$  [120]. Although the phase diagram in Fig. 5.4 (b) satisfies the above condition and captures the main features of the bulk phase diagram of  $^3\text{He}$ – $^4\text{He}$  mixtures, its shape near the tricritical end point tce differs from the experimental one (see Fig. 5.2). In particular, in the phase diagram in Fig. 5.4 (b), upon lowering the temperature below  $T_{tce}$  along the path  $X_3 = X_3^{tce}$ , the model mixture does not enter the two–phase region, as it is the case for the actual  $^3\text{He}$ – $^4\text{He}$  mixture. Note that the experimental phase diagram in Fig. 5.2 is drawn in the  $(T, C_3)$  plane (The model phase diagram in the same  $(T, C_3)$  plane is shown in the inset of Fig. 5.4(b).) Furthermore, although the condition  $J_s > J_s^0$  places the critical end point ce of the phase diagram with  $(C_0/K_0, J_0/K_0, J_s = 0)$  into the two–phase region of the phase diagram with  $(C_0/K_0, J_0/K_0, J_s > J_s^0)$ , a certain residual, distorting influence of this critical end point ce on the wetting films may still be present, especially if ce lies near any of the two binodals of the demixing transitions of the transformed phase diagram (solid black lines in Figs. 5.4(b) and (c)). In order to address this issue, after finding the necessary conditions for the coupling parameters leading to the desired topology, one can modify the values of  $(C_0/K_0, J_0/K_0)$  with  $J_s = J_s^0$  such, that the critical end point ce (which starts to shift into metastability for  $J_s = J_s^0$ ) moves deeply into the two–phase region of the transformed phase diagram. These considerations have led to the following choice for the coupling constants:  $(C/K, J/K, J_s/K) = (1, 9.10714, 3.70107)$ . The corresponding phase diagram is shown in Fig. 5.4(c).

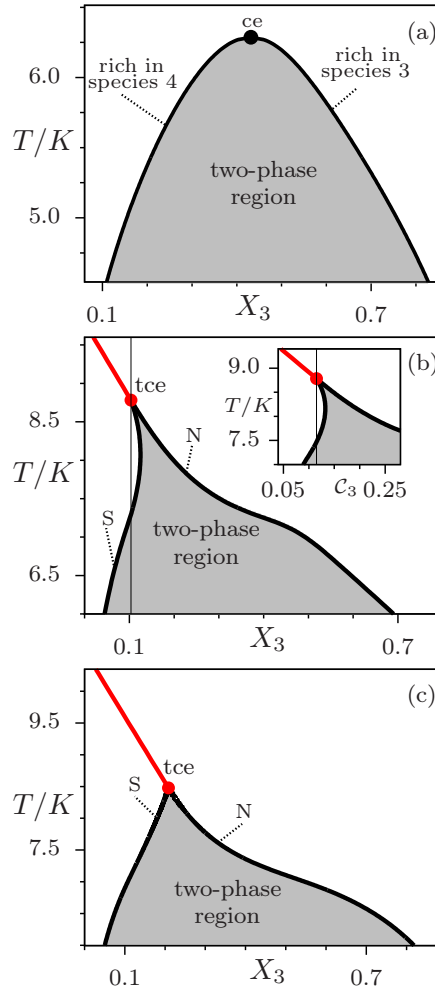


**Figure 5.4.** Liquid–liquid demixing phase transitions in the bulk at coexistence with the vapor phase (the vapor phase is not shown here) in the  $(X_3, T)$  plane, with  $X_3 = \langle N_3 \rangle / (LN) = D - X$  for (a)  $(C/K, J/K, J_s/K) = (1, 5.714, 0)$ , (b)  $(C/K, J/K, J_s/K) = (1, 5.714, 3.674)$ , and (c)  $(C/K, J/K, J_s/K) = (1, 9.107, 3.701)$ . The inset of panel (b) shows the same phase diagram in the  $(T, C_3)$  plane, where  $C_3 = X_3/D$  denotes the concentration of  $^3\text{He}$ . The phase diagrams in (a) and (b) have been discussed in detail in the previous chapter. Note that there the coupling constants are rescaled by a factor of 6 and the total number of lattice sites are denoted as  $\mathcal{N}$ , whereas here the total number of lattice sites is given by  $LN$ . In (b) and (c) the black curves denote the binodals of the first–order phase transitions between the normal fluid (N) and the superfluid (S). The lines of first–order phase transitions in (a) terminate at the critical end point  $ce$  with  $T_{ce}/K = 6.286$ , whereas in (b) and (c) the lines of first–order phase transitions terminate at a tricritical end point  $tce$ . In (b) and (c) the red curve denotes the  $\lambda$ -line of second–order phase transitions between the normal fluid and the superfluid. The temperature of the tricritical end point in panels (b) and (c) are  $T_{tce}/K = 8.782$  and  $T_{tce}/K = 8.47974$ , respectively. In (b) the thin vertical line indicates  $X_3 = X_3^{tce}$ , whereas in the inset of this figure the thin vertical line indicates  $C_3 = C_3^{tce}$ . The short dotted strokes indicate the character (S, N, rich in species 4, or rich in species 3) of the corresponding binodal.

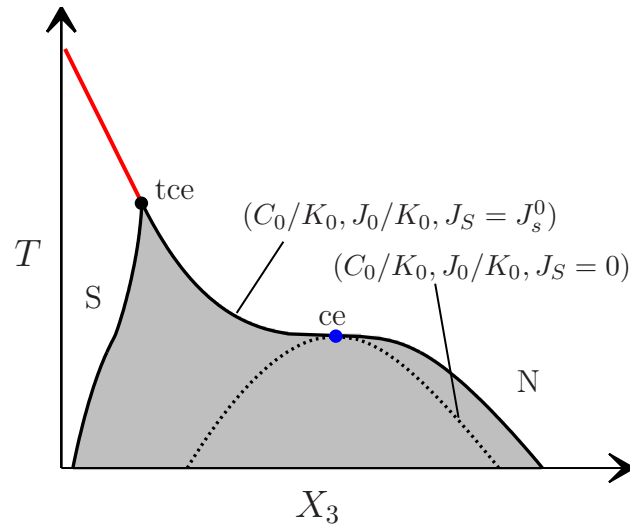


**Figure 5.5.** Schematic representation of the transformation of the bulk phase diagram of a classical binary liquid mixture for fixed values of  $(C_0/K_0, J_0/K_0)$  and  $J_s = 0$  (the dotted curve) into that of  ${}^3\text{He}$ - ${}^4\text{He}$  mixtures with  $J_s = J_s^0 \neq 0$  (solid curves). In a first step, for suitable, fixed values of  $(C_0/K_0, J_0/K_0)$  and  $J_s = 0$  one has the phase diagram of a classical binary mixture with ce as in Fig 5.4(a). In a second step, one has to find a nonzero value of  $J_s = J_s^0$  (which produces the superfluid phase) such, that the critical end point ce of the phase diagram for  $(C_0/K_0, J_0/K_0, J_s = 0)$ , is in thermodynamic coexistence with a superfluid phase. For this new set of coupling constants  $(C_0/K_0, J_0/K_0, J_s > J_s^0)$ , the phase diagram with  $(C_0/K_0, J_0/K_0, J_s = 0)$  lies in the two phase region of the phase diagram with  $(C_0/K_0, J_0/K_0, J_s > J_s^0)$  [120].

## 5.2. Layering and wetting for short-ranged surface fields

In this section the layering and wetting behavior [67] of the present model with short-ranged surface fields  $f_+(l) = \tilde{f}_+ \delta_{l,0}$  and  $f_-(l) = \tilde{f}_- \delta_{l,0}$  are studied. The field  $f_+(l)$  describes the enhancement of the fluid density near the wall, whereas  $f_-(l)$  expresses the preference of the wall for  ${}^4\text{He}$  over  ${}^3\text{He}$ .

Within the present model  $\mu_+$  is the field conjugate to the number density order parameter  $D_l$ . By changing  $\mu_+$  from its value  $\mu_+^{\text{co}}(P, T)$  at liquid-vapor coexistence and at a given temperature  $T$  and pressure  $P$ , one can drive the bulk system either towards the liquid phase ( $\Delta\mu_+ = \mu_+ - \mu_+^{\text{co}} > 0$ ) or towards the vapor phase ( $\Delta\mu_+ < 0$ ). In order to realize the experimental conditions and to follow the thermodynamic paths which lie on the brown surface in Fig. 5.1 (as in the experiments), one has to choose  $\Delta\mu_+ < 0$  such that the bulk system remains thermodynamically in the vapor phase. With this constraint the OP profiles are obtained by solving Eqs. (5.14) - (5.16) for  $\{(X_l, D_l, M_l) \mid l = 0, \dots, L-1\}$ . It has been found that the occurrence of wetting films as well as their thicknesses depend on the strength of the surface fields  $\tilde{f}_+$  and  $\tilde{f}_-$ . Since

## 5. Tricritical Casimir forces in $^3\text{He}$ - $^4\text{He}$ wetting films

---

along the experimental paths taken in Ref. [17] the system is in the complete wetting regime, one has to choose such values of the surface fields for which complete wetting does occur.

Based on the number density profile  $D_l$  one can define the film thickness as [67]

$$y(\mu_-, \mu_+, \tilde{f}_+, \tilde{f}_-, T) = \frac{\varrho}{D_m - D_b}, \quad (5.18)$$

where  $D_b$  is the bulk density of the vapor phase,

$$\varrho = \sum_{l=0}^{L-1} (D_l - D_b) \quad (5.19)$$

is the excess adsorption, and  $D_m$  is the density of the metastable liquid phase at the thermodynamic state corresponding to the stable vapor phase. In Figs. 5.8, 5.10, 5.14, 5.16, and 5.17 the film thickness  $y$  is defined via Eq. (5.18). Alternatively, one can define  $y$  as the position of the inflection point of the density profile  $D_l$  at the emerging liquid–vapor interface. As an example, the film thickness  $y$  in Fig. 5.11 is defined via this latter convention. The profile  $X_l = X_{4,l} - X_{3,l}$  indicates, whether the various layers are occupied mostly by species of type 4 (positive or large values of  $X_l$ ) or by species of type 3 (negative or small values of  $X_l$ ). A nonzero magnetization profile signals that the wetting film is superfluid. In the next subsection the wetting behavior of the model with  $J_s = 0$  (classical binary mixture) is discussed. This subsection shows how within the present model the strength of the surface fields influences the formation and the thickness of the wetting films. In Subsec. 5.2.2  $^3\text{He}$  -  $^4\text{He}$  mixtures are considered ( $J_s \neq 0$ ). This subsection focuses on describing the present, experimentally relevant situation.

### 5.2.1. Layering and wetting for classical binary liquid mixtures

In this subsection a classical binary liquid mixture of species 3 and 4, described by the Hamiltonian given in Eq. (5.3) with the coupling constants  $(C/K, J/K, J_s/K) = (1, 5.714, 0)$  is considered. The bulk phase diagram of this system in the  $(T, X_3)$  plane is shown in Fig. 5.4(a). All figures in this subsection (i.e., Figs. 5.6 - 5.10) share the coupling constants  $(C/K, J/K, J_s/K) = (1, 5.714, 0)$ . In Figs. 5.6(a) and 5.7 - 5.10 the system size is  $L = 40$ , whereas in Fig. 5.6(b) it is  $L = 80$ . In the following by considering thermodynamic states with  $T > T_{ce}$  and  $\Delta\mu_+ = \mu_+ - \mu_+^{co} < 0$ , the influence of the strengths of the surface fields on the formation of the wetting films are studied. These thermodynamic states correspond to the case, in which the vapor is the bulk phase and the wetting phase is the mixed supercritical liquid phase.

Let us first keep  $\tilde{f}_- = 0$  and vary  $\tilde{f}_+$ . For weak surface fields  $\tilde{f}_+$ , high density layers near the surface cannot be stabilized, so that the model does not exhibit wetting by the

## 5.2. Layering and wetting for short-ranged surface fields

---

mixed-liquid phase. Instead, the wall prefers the vapor phase so that upon approaching the liquid-vapor coexistence from the liquid side (i.e.,  $\Delta\mu_+ \rightarrow 0^+$ ) a vapor film forms close to the wall corresponding to drying of the interface between the wall and the mixed liquid.

Covering the case of weak surface fields, Fig. 5.6(a) shows the number density profiles for  $(\tilde{f}_+, \tilde{f}_-)/K = (0.857, 0)$  at  $\Delta\mu_+/K = (\mu_+ - \mu_+^{\text{co}})/K = -8.57 \times 10^{-4}$ , i.e., on the vapor side for several temperatures above  $T_{\text{ce}}$  and at fixed  $X_3 = X_3^{\text{ce}}$ . Figure. 5.6(b) shows the number density profiles for the same bulk system with the same surface fields but for  $\Delta\mu_+/K = (\mu_+ - \mu_+^{\text{co}})/K = +8.57 \times 10^{-4}$  so that the stable bulk phase is liquid. Since the wall prefers the vapor phase, upon increasing  $T$  a drying film forms at the surface of the solid substrate.

For larger values of  $\tilde{f}_+$  (see Fig. 5.7), i.e., for  $(\tilde{f}_+, \tilde{f}_-)/K = (5.143, 0)$ , at lower temperatures  $T$  one finds monotonically decaying density profiles without shoulder formation whereas at higher temperatures the density profiles tend to exhibit plateaus characteristic of wetting (see Fig. 5.7(a)). Note that in Figs. 5.7(a) and (b) the number density in the first layer as part of the wetting film decreases upon increasing  $T$ . This is in accordance with the fact that the density of the bulk liquid phase as the wetting phase decreases upon heating, whereas the bulk vapor density increases. The profiles  $X_l = X_{4,l} - X_{3,l}$  shown in red and blue in Fig. 5.7(b) have local minima at  $l = 5$  and  $l = 9$ , respectively. These minima occur approximately at the position of the emerging liquid-vapor interface (see the corresponding curves in panel (a)) and indicate that species of type 3 preferentially accumulate at the liquid-vapor interface. Figures 5.7 (c) and (d) show the OP profiles for  $(\tilde{f}_+, \tilde{f}_-)/K = (5.143, 0.857)$  and  $\Delta\mu_+/K = -8.57 \times 10^{-4}$  at several values of the temperature. One can see that for positive values of  $\tilde{f}_-$  both  $D_l$  and  $X_l$  are enhanced in the first layer. This corresponds to the preferential adsorption of species of type 4 at the wall.

In order to see how the wetting films grow upon approaching the liquid-vapor coexistence surface, one can fix  $T$  and vary  $\Delta\mu_+$ . Figure 5.8 shows the film thickness  $y/a$  versus  $\Delta\mu_+$  for  $(\tilde{f}_+, \tilde{f}_-)/K = (8.571, 0)$  and for several temperatures;  $y$  is calculated according to Eq. (5.18). For low temperatures, upon approaching the liquid-vapor coexistence surface the film thickness increases smoothly and reaches a plateau. This corresponds to incomplete wetting. The height of this plateau increases gradually upon increasing  $T$  towards  $7.097 < T_w/K < 7.123$ , which corresponds to a critical wetting transition between incomplete and complete wetting [67]. The corresponding line of wetting transitions lies on the surface of the liquid-vapor transitions ( $S_1$  in Fig. 2.5) between the critical end point  $\text{ce}$  and the line of critical points of the liquid-vapor transitions ( $L_c$  in Fig. 2.5). Note that Fig. 5.8 provides a semi-logarithmic plot so that the linear growth of the film thickness on this scale confirms the theoretically expected logarithmic growth of the film

## 5. Tricritical Casimir forces in $^3\text{He}$ - $^4\text{He}$ wetting films

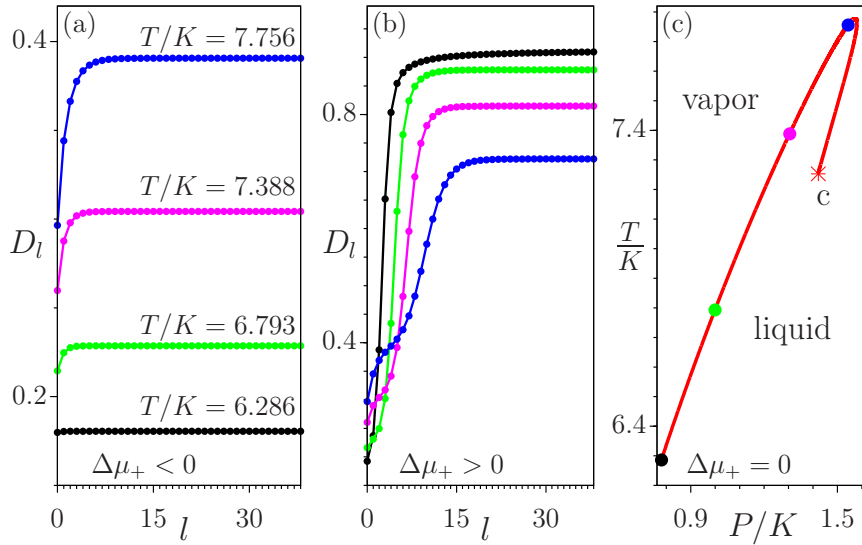


**Figure 5.6.** Number density profiles for weak surface fields  $(\tilde{f}_+, \tilde{f}_-)/K = (0.857, 0)$  and for several values of temperature  $T$  (same color code in all panels) above  $T_{ce}/K = 6.286$  and at  $X_3 = X_3^{ce} = 0.431$  in the liquid phase, with (a)  $\Delta\mu_+/K = -8.57 \times 10^{-4}$  and (b)  $\Delta\mu_+/K = +8.57 \times 10^{-4}$ . In (a) the bulk phase is the vapor phase whereas in (b) it is the coexisting liquid phase with slight offsets. Panel (c) shows the liquid–vapor coexistence line (red curve) in the  $(P, T)$  plane, emerging under the constraint  $X_3 = X_3^{ce}$  in the liquid phase. The colored dots in panel (c) indicate the thermodynamic states with the same temperature values as in panels (a) and (b), which, unlike in these two panels, lie at liquid–vapor coexistence. The star denotes the liquid–vapor critical point  $(P_c/K, T_c/K) = (1.422, 7.230)$ . The thermodynamic paths in panels (a) and (b) follow the red curve in panel (c) but with the corresponding offset values  $\Delta\mu_+$ . In panel (a) the corresponding thermodynamic states are:  $(T/K, D = X_4 + X_3, X = X_4 - X_3, M) = \{(6.286, 0.181, -0.121, 0), (6.793, 0.229, -0.137, 0), (7.388, 0.304, -0.155, 0), (7.756, 0.391, -0.174, 0)\}$ . The vapor bulk phase in (a) is preferred by the wall. Accordingly, there are no liquidlike wetting films. In panel (a) near  $T_c$  critical adsorption (see Fig. 8 in Ref. [66]) of the preferred vapor phase occurs, which is indicated by the increased depth and range of the minimum in  $D_l$ . In panel (b), due to  $\Delta\mu_+ > 0$  the stable bulk phase is the liquid. Since the vapor phase is preferred by the wall drying films form there upon increasing the temperature. The corresponding thermodynamic states are:  $(T/K, D, X, M) = \{(6.286, 0.913, 0.050, 0), (6.793, 0.878, 0.015, 0), (7.388, 0.815, -0.048, 0), (7.756, 0.722, -0.141, 0)\}$ . The value of  $\mu_-$  can be obtained from Eq. (5.15) using the values of  $(T, D, X, M)$  for the corresponding thermodynamic states as provided above. Note that the nonmonotonic behavior of the red curve in (c) is caused by the constraint  $X_3 = X_3^{ce}$ . For (c), in order to identify the vapor and liquid phases, in addition to  $T$  and  $P$  also the value of the chemical potential  $\mu_-$  is required, which is not shown.

thickness  $y \sim \ln(|\Delta\mu_+|/K)$  for short-ranged surface fields [67]. At higher temperatures  $T$  the film thickness does not increase smoothly anymore but rather exhibits jumps due

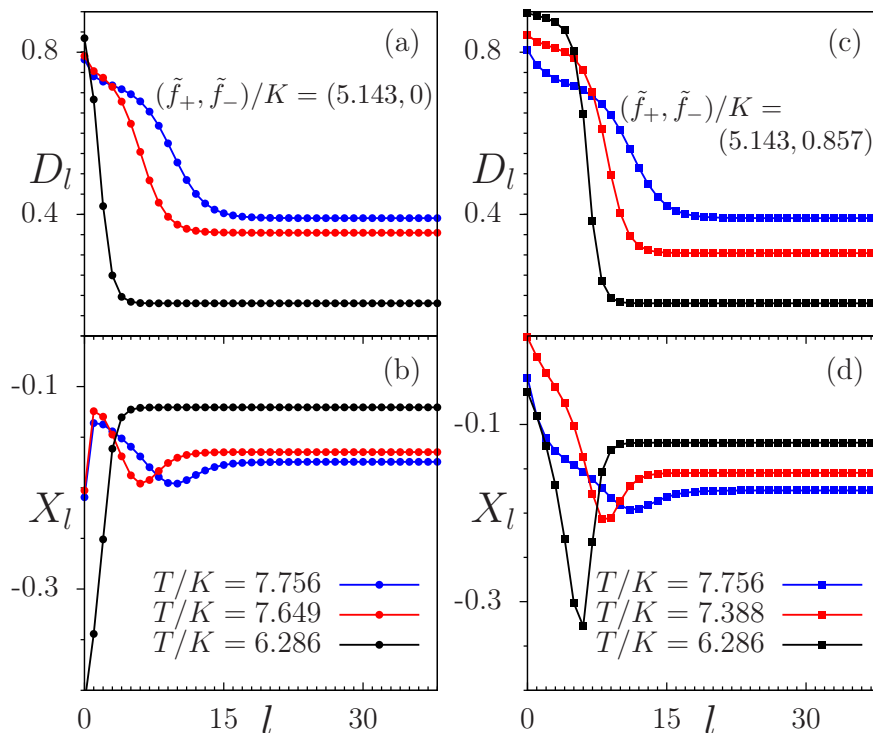


**Figure 5.7.** Order parameter profiles  $D_l$  and  $X_l$  at  $X_3 = X_3^{\text{ce}} = 0.431$  and for  $\Delta\mu_+/K = -8.57 \times 10^{-4}$  for several temperatures and for two sets of surfaces fields. In panels (a) and (b) the surface fields are  $(\tilde{f}_+, \tilde{f}_-)/K = (5.143, 0)$ , whereas panels (c) and (d) correspond to  $(\tilde{f}_+, \tilde{f}_-)/K = (5.143, 0.857)$ . The bulk phase is the vapor phase and the wall prefers the liquid phase, giving rise to wetting films. The positive value of  $\tilde{f}_-$  not only results in the increase of the number density  $X_{4,l}$  of species 4 and hence also of  $X_l$  in the first layer (see panel (d)), but also increases the total number density  $D_l$  in the first layer (see panel (c)). The stable thermodynamic states of the vapor phase in the bulk are  $(T/K, D, X, M) = \{(6.286, 0.180, -0.121, 0), (7.388, 0.304, -0.155, 0), (7.649, 0.355, -0.165, 0), (7.756, 0.391, -0.174, 0)\}$ . All three bulk states lie in the vapor phase close to liquid–vapor coexistence on the left side of the red line shown Fig. 5.6(c). The value of  $\mu_-$  can be obtained from Eq. (5.15) using the values of  $(T, D, X, M)$  for the corresponding thermodynamic states as provided above.

to layering transition. Figure 5.9 shows the location of these layering transitions in the  $(\mu_+, T)$  plane for  $(\tilde{f}_+, \tilde{f}_-)/K = (8.571, 0)$ . If a thermodynamic path passes through any of these lines the film thickness undergoes a small jump of the size  $l \simeq 1$ . Each line of the layering transitions ends at a critical point. Along thermodynamic paths, which pass by these critical points the jumps of the film thickness become rounded as for the green and red curves in Fig. 5.8. The color code in Fig. 5.9 does not carry a particular meaning; the lines are colored differently so that it is easier to distinguish them. The closer the system is to the liquid–vapor coexistence surface, i.e., the smaller  $|\Delta\mu_+|$  is, the

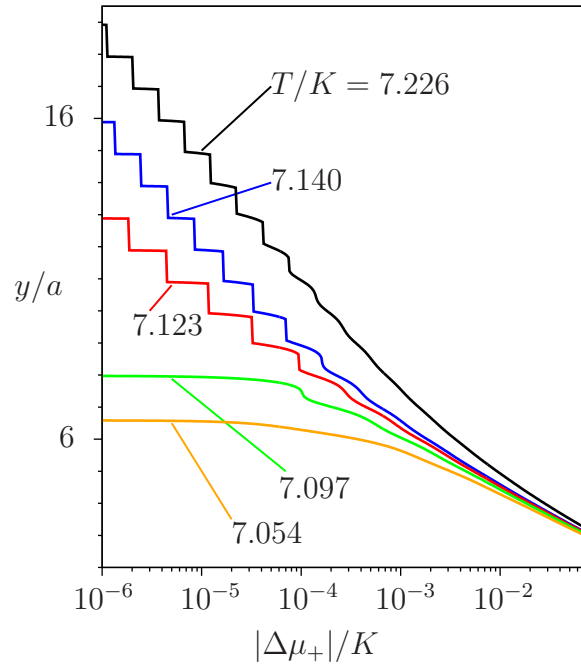


**Figure 5.8.** Equilibrium film thickness  $y$  over lattice constant  $a$  versus  $|\Delta\mu_+|/K$  for  $(\tilde{f}_+, \tilde{f}_-)/K = (8.571, 0)$  at  $X_3 = X_3^{\text{ce}}$ , and for several temperatures. Upon approaching the liquid–vapor coexistence surface at low temperatures, the film thickness increases smoothly and reaches a plateau. The height of this plateau increases gradually by increasing  $T$ , indicating  $7.097 < T_w/K < 7.123$ . The jumps are due to first–order layering transitions induced by the lattice model. Above the roughening transition they are an artifact of mean field theory [67]. For  $T > T_w$  one has  $y(\Delta\mu_+ \rightarrow 0^-) \sim \kappa \ln \frac{1}{|\Delta\mu_+|/K}$  with a slight increase of  $\kappa(T)$  as a function of  $T$ .

closer are the lines of layering transitions. Figure 5.10 shows how the increasing density of the layering transition lines affects the film thickness while varying the temperature at fixed values of  $\Delta\mu_+/K = -8.57 \times 10^{-8}$  and  $X_3 = X_3^{\text{ce}} = 0.431$ .

### 5.2.2. Layering and wetting for $^3\text{He}$ - $^4\text{He}$ mixtures

In this subsection the results of the wetting film thickness measurements, as carried out for  $^3\text{He}$  -  $^4\text{He}$  mixtures in Ref. [17], are reproduced numerically. Here the coupling constants are chosen to be  $(C/K, J/K, J_s/K) = (1, 9.10714, 3.70107)$ , which describe a system with the phase diagram resembling that of  $^3\text{He}$  -  $^4\text{He}$  mixtures. The bulk phase diagram for these coupling constants is shown in Fig. 5.4(c). All figures in this subsection (i.e., Figs. 5.11 - 5.16) share these coupling constants with the surface fields  $(\tilde{f}_+, \tilde{f}_-)/K = (10.714, 16.071)$ , and the system size  $L = 60$ . For these values of the surface fields complete wetting occurs. This is shown by the growth of wetting films

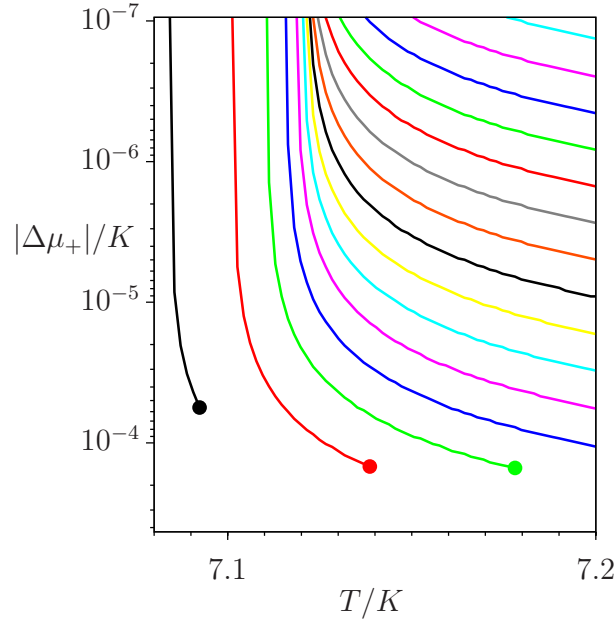


**Figure 5.9.** Layering transitions in the  $(\mu_+, T)$  plane for  $(\tilde{f}_+, \tilde{f}_-)/K = (8.571, 0)$ . Each line of first-order layering transition ends at a critical point. The color code does not carry a specific meaning. The lines are colored differently so that it is easier to distinguish them.

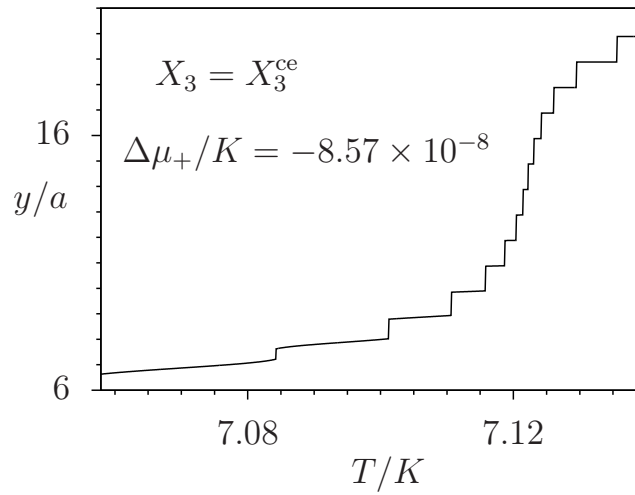


**Figure 5.10.** Equilibrium film thickness  $y$  over lattice constant  $a$  as a function of temperature for  $\Delta\mu_+/K = -8.57 \times 10^{-8}$  and  $X_3 = X_3^{\text{ce}}$ . Since  $\Delta\mu_+$  is nonzero,  $y(T)$  does not diverge but attains a maximum upon passing by  $T_w$ . This maximum diverges for  $\Delta\mu_+ \rightarrow 0$ . The jumps are bunched together around  $T/K \simeq 7.125$  and spread-out otherwise.

## 5. Tricritical Casimir forces in $^3\text{He}$ - $^4\text{He}$ wetting films

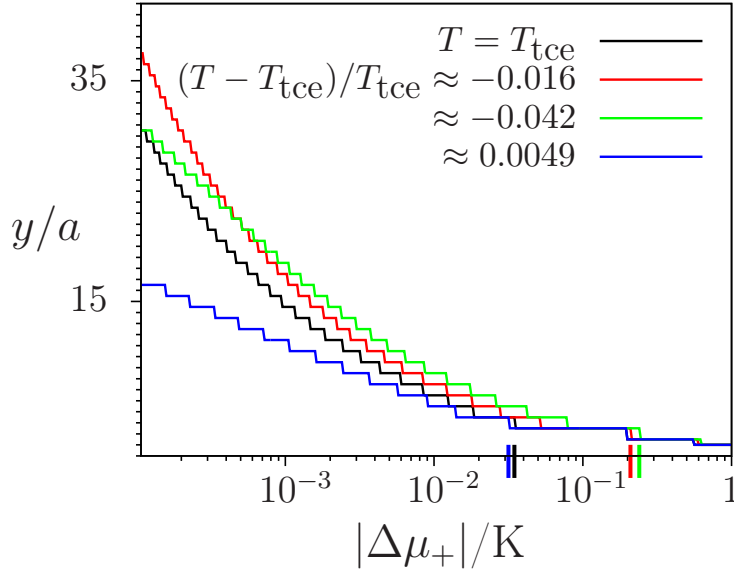


**Figure 5.11.** Equilibrium film thickness  $y$  over lattice constant  $a$  versus  $|\Delta\mu_+|/K$  for  $(\tilde{f}_+, \tilde{f}_-)/K = (10.714, 16.071)$  and for four temperatures. Unlike the situation in Fig. 5.8 with  $J_s = 0$ , the thickness of the wetting films as a function of  $|\Delta\mu_+|$  is a nonmonotonic function of  $T$ . The most rapid increase occurs at  $(T - T_{\text{tce}})/T_{\text{tce}} \approx -0.016$ , whereas for lower and higher temperatures the growth of the wetting film as a function of  $\Delta\mu_+$  is slower. Upon approaching the liquid–vapor coexistence surface, the  $^4\text{He}$ -rich layers within the wetting films become superfluid. At each temperature, the continuous surface transition to superfluidity occurs for values of the offset  $|\Delta\mu_+|$  smaller than the one indicated by the corresponding tick on the abscissa with the same color. For  $(T - T_{\text{tce}})/T_{\text{tce}} = -0.016$  and  $(T - T_{\text{tce}})/T_{\text{tce}} = -0.042$ , the number density of  $^3\text{He}$  on the superfluid branch of the binodal (Fig. 5.4(c)) is  $X_3 = 0.201$  and  $X_3 = 0.188$ , respectively, whereas for  $T \geq T_{\text{tce}}$  the number density of  $^3\text{He}$  is fixed at  $X_3 = X_3^{\text{tce}} = 0.20845$ .

upon approaching the liquid–vapor coexistence surface as illustrated in Fig. 5.11. For all temperatures considered, upon approaching liquid–vapor coexistence the wetting films become thicker:  $y(\Delta\mu_+ \rightarrow 0^-) \sim \kappa \ln \frac{1}{|\Delta\mu_+|/K}$  with a significant temperature dependence of the amplitude  $\kappa$ , which means that in Fig. 5.11 the wetting temperature  $T_w$  is below the considered temperature interval. This is different from the situation in Fig. 5.8 with  $J_s = 0$ , where only for sufficiently high temperatures (i.e.,  $T > T_w$ ) complete wetting occurs. Interestingly, in Fig. 5.11 at the reduced temperature  $(T - T_{\text{tce}})/T_{\text{tce}} \approx -0.016$  the film thickness exhibits the most rapid increase upon approaching the liquid–vapor coexistence surface (see the red curve), whereas for higher and lower temperatures the growth of the film thickness is reduced, i.e., the amplitude  $\kappa(T)$  introduced above has a maximum at  $(T - T_{\text{tce}})/T_{\text{tce}} \approx -0.016$ . This is different from what one observes in Fig. 5.8, where the thickness of the wetting film is, via  $\kappa(T)$ , a monotonically increasing

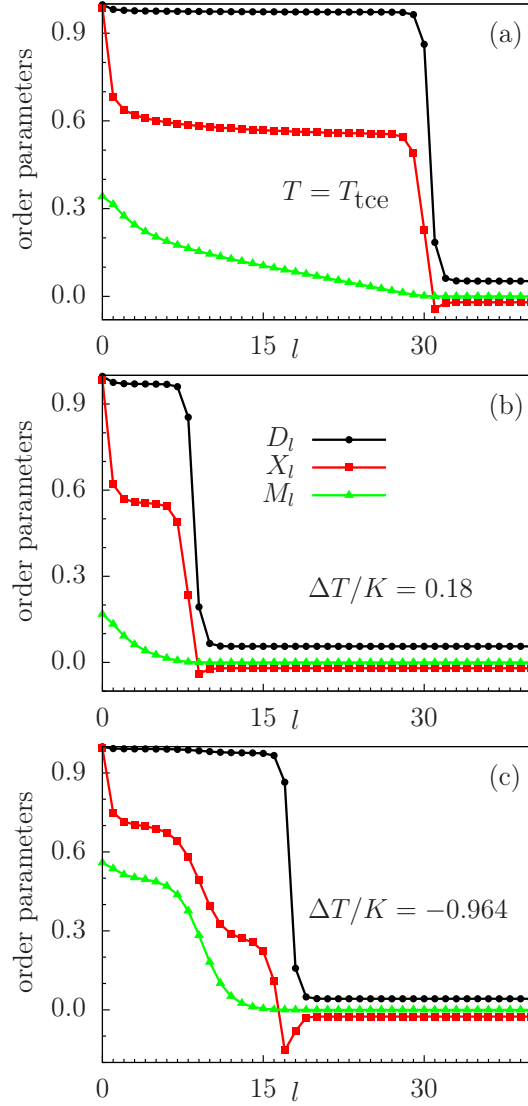


**Figure 5.12.** Order parameter profiles  $D_l$ ,  $X_l$ , and  $M_l$  for  $(\tilde{f}_+, \tilde{f}_-)/K = (10.714, 16.071)$  at  $\Delta\mu_+/K = -1.07 \times 10^{-4}$  for the bulk states (a)  $T = T_{\text{tce}}$ ,  $X_3 = X_3^{\text{tce}}$ , (b)  $\Delta T/K = (T - T_{\text{tce}})/K = 0.18$ ,  $X_3 = X_3^{\text{tce}}$ , and (c)  $\Delta T/K = (T - T_{\text{tce}})/K = -0.964$ ,  $X_3 = 0.1461$  (which is on the superfluid branch of the binodal (Fig. 5.4(c))). For these bulk states, in panels (a) - (c) the stable vapor phase (i.e.,  $l \rightarrow \infty$ ) exhibits the order parameters  $(D = X_4 + X_3, X = X_4 - X_3, M) = \{(0.0523, -0.0206, 0), (0.0559, -0.0204, 0), (0.0422, -0.0255, 0)\}$ , respectively. The bulk parameters of the system are those for Fig. 5.4(c). The keys for the OP profiles are the same for all panels. The value of  $\mu_-$  can be obtained from Eq. (5.15) using the values of  $(T, D, X, M)$  for the corresponding thermodynamic states as provided above.

function of  $T$ . Note that in Fig. 5.11 for the curves with  $T \geq T_{\text{tce}}$  the number density of  $^3\text{He}$  is fixed at  $X_3 = X_3^{\text{tce}} = 0.20845$ . However, for  $T < T_{\text{tce}}$  the system phase separates and the number density of  $^3\text{He}$  changes. Accordingly, in Fig. 5.11 for  $(T - T_{\text{tce}})/T_{\text{tce}} =$

## 5. Tricritical Casimir forces in ${}^3\text{He}$ - ${}^4\text{He}$ wetting films

---

$-0.016$  and  $(T - T_{\text{tce}})/T_{\text{tce}} = -0.042$ , the number density of  ${}^3\text{He}$  on the superfluid branch of the binodal (Fig. 5.4(c)) is  $X_3 = 0.201$  and  $X_3 = 0.188$ , respectively. The OP profiles for three temperatures at  $\Delta\mu_+/K = -1.07 \times 10^{-4}$  are shown in Fig. 5.12. Due to the large value of  $\tilde{f}_-$ , the number density  $X_{4,l}$  of  ${}^4\text{He}$  is enhanced near the wall and hence  $X_l = X_{4,l} - X_{3,l}$  is large there. If the bulk liquid is in the normal fluid phase but close to either the  $\lambda$ -line for  $T > T_{\text{tce}}$ , or to the normal branch of the binodal (Fig. 5.4(c)) for  $T < T_{\text{tce}}$ , this enhancement induces symmetry breaking of the superfluid OP near the wall. At the liquid–vapor coexistence surface, this surface transition occurs at temperatures  $T_s(X_3)$ , which depend on the bulk number density  $X_3$  of  ${}^3\text{He}$  atoms or, equivalently, on the bulk concentration  $\mathcal{C}_3$  of  ${}^3\text{He}$  as  $T_s(\mathcal{C}_3)$  (see Fig. 5.13). With the bulk being in the vapor phase, the continuous surface transition occurs within the wetting film for offsets  $\Delta\mu_+$  from the liquid–vapor coexistence surface smaller than a certain temperature dependent value, which is marked in Fig. 5.11 by the tick along the abscissa colored accordingly. Upon crossing the continuous surface transition one observes a nonzero profile  $M_l$  in the wetting film (see Figs. 5.12(a) and (b)). For  $T < T_{\text{tce}}$ , for which the bulk liquid phase separates into a superfluid and a normal fluid phase, the OP profiles within the wetting films exhibit two plateaus, one corresponding to the superfluid phase (note the left plateau of  $M_l$  in Fig. 5.12(c)) and the other one (on the right side) corresponding to the normal fluid phase. The minimum of the profile  $X_l$  occurs at the emerging liquid–vapor interface at around (a)  $l = 31$ , (b)  $l = 9$ , and (c)  $l = 17$ . This demonstrates the effective attraction of  ${}^3\text{He}$  towards the emerging liquid–vapor interface, which suppresses the superfluid OP at the liquid–vapor interface. On the other hand the preference of the wall for  ${}^4\text{He}$  enhances the superfluid OP there as if there would be a surface field acting on the superfluid OP, which is , however, not the case.

The experimental data [17], reproduced in Fig. 3.4, have been obtained at liquid–vapor coexistence along the paths of fixed concentration  $\mathcal{C}_3$  of  ${}^3\text{He}$  as shown in the inset of Fig. 5.13 by the vertical dotted lines. (Note that  $X$  in Fig. 3.4 corresponds to the concentration of  ${}^3\text{He}$ , which here is denoted by  $\mathcal{C}_3 = (D - X)/(2D) = X_3/(X_3 + X_4)$ . The subscript  $l$  has been ignored because the quantities are referring to the bulk values.) The thermodynamic paths of fixed  ${}^3\text{He}$  concentration followed in our calculations are parallel to the experimental ones but are located in the vapor phase close to the liquid–vapor coexistence surface (like the brown surface in Fig. 5.1).

The film thickness versus temperature along a path with an offset  $\Delta\mu_+/K = -1.07 \times 10^{-4}$  parallel to the vertical black dashed line in Fig. 5.13 is shown in Fig. 5.14. Within the considered temperature range the system is above the wetting temperature  $T_w$  (not shown in the figure). It has been found that at fixed  $\mathcal{C}_3$  the variation of the film thickness with temperature is nonmonotonic. Upon increasing the temperature, for  $T > T_s$ , the

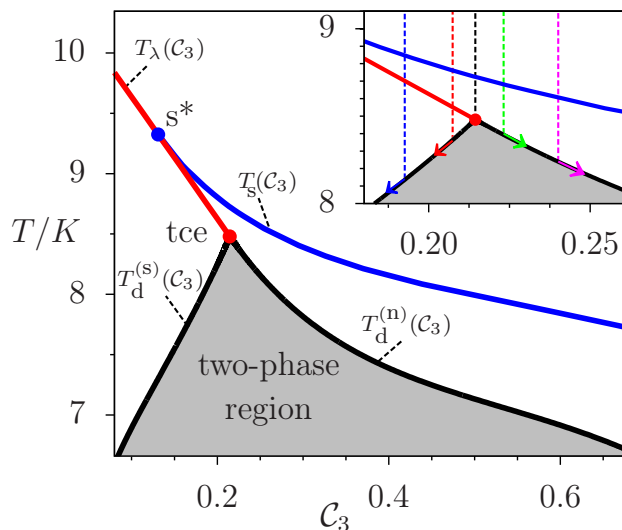


**Figure 5.13.** The bulk liquid–liquid phase transitions at coexistence with the vapor phase as in Fig. 5.4 (c) plotted in the  $(T, \mathcal{C}_3)$  plane, with  $\mathcal{C}_3 = (D - X)/2D$  as the concentration of  $^3\text{He}$  (the vapor phase is not shown here). The blue line  $T_s(\mathcal{C}_3)$  represents the continuous surface transition. Upon crossing this transition line a thin film near the wall becomes superfluid although the bulk remains a normal fluid. This line merges with the  $\lambda$ -line (red line denoted as  $T_\lambda(\mathcal{C}_3)$ ) at the special point  $S^*$ . The inset shows the vertical thermodynamic paths (at liquid–vapor coexistence) taken experimentally. The numerical paths in our calculations are located in the vapor phase parallel to the ones in the inset.  $T_d^{(s)}(\mathcal{C}_3)$  [ $T_d^{(n)}(\mathcal{C}_3)$ ] denotes the superfluid [normal fluid] binodal of the two–phase region. The arrows indicate how the vertical thermodynamic paths continue after encountering the demixing curve. The path shown by the black dotted line can follow both binodals.

film thickness increases. A much steeper increase of the film thickness, associated with a break in slope, occurs between  $T_s$  and  $T_{tce}$ , where the TCFs emerge. (Note that due to the offset from liquid–vapor coexistence the sharp drop of  $y/a$  occurs slightly below  $T_{tce}$  (see Fig. 5.13).)

As discussed in the Introduction, due to the surface transition close to  $T_{tce}$  the superfluid OP becomes nonzero near the wall. This profile vanishes at the emerging liquid–vapor interface, where the  $^3\text{He}$  atoms accumulate. This behavior corresponds to the non-symmetric, effective  $(+, O)$  BCs for the superfluid order parameter  $M_l$  in the wetting film. Therefore, the resulting TCF acting on the liquid–vapor interface is repulsive and leads to an increase of the film thickness. The maximum film thickness occurs at  $T_{\text{peak}}/K \approx 8.3346$ , which lies below  $T_{tce}$  — in agreement with the experimental results (see Fig. 3.4) ( $T_{\text{peak}}$  is defined as the mid point of the temperature range enclosing the maximum film thickness).  $T_s$  denotes the temperature of the surface transition. Fig-

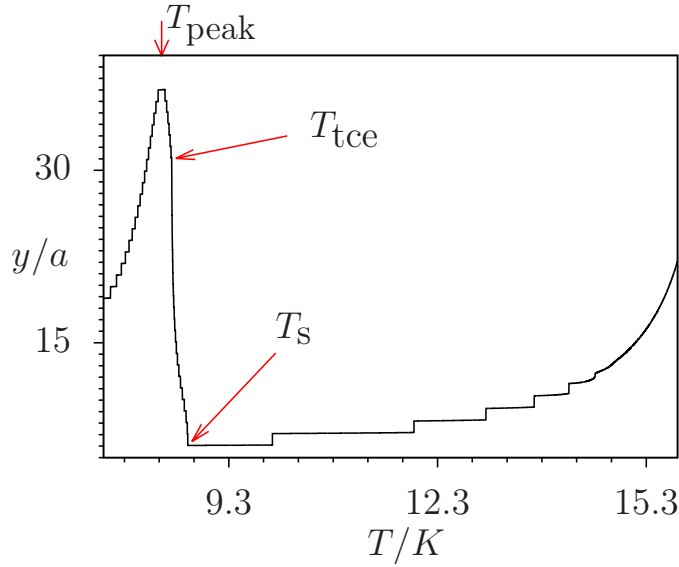


**Figure 5.14.** Numerical results for the equilibrium film thickness  $y$  over lattice constant  $a$  as function of temperature  $T$  corresponding to the thermodynamic path at fixed  $\mathcal{C}_3 = \mathcal{C}_3^{\text{tce}}$  and  $\Delta\mu_+/K = -1.07 \times 10^{-4}$  (i.e., slightly shifted thermodynamic path shown by the vertical black dashed line in Fig. 5.13). The arrows indicate the tricritical end point  $T_{\text{tce}}$  and the onset temperature  $T_s \simeq T_s(\mathcal{C}_3)$  for superfluidity at the surface transition. (The deviation of  $T_s$  from  $T_s(\mathcal{C}_3)$  (see Fig. 5.13) is due to the offset from liquid–vapor coexistence.) Below the tricritical temperature the thermodynamic path follows  $T_d^{(s)}(\mathcal{C}_3)$  indicated in Fig. 5.13 (infinitesimally on the superfluid side). For further discussions see the main text. The bulk parameters of the system are those belonging to Fig. 5.4(c) and Fig. 5.13.  $T_{\text{peak}}/K = 8.3346$  is the position of the peak.

ure 5.15 shows how the offset value  $\Delta\mu_+$  affects the equilibrium film thickness  $y$ . As expected, upon increasing the offset value, the film thickness decreases. Moreover  $T_{\text{peak}}$  shifts towards lower temperatures.

Following the other thermodynamic paths indicated in Fig. 5.13 renders a distinct scenario. Figure 5.16 shows the film thickness  $y$  over lattice constant  $a$  versus temperature  $T$  for two values of  $\mathcal{C}_3 > \mathcal{C}_3^{\text{tce}}$  (green curve and violet curve) at  $\Delta\mu_+/K = -1.07 \times 10^{-4}$ . (As a reference, the results for  $\mathcal{C}_3 = \mathcal{C}_3^{\text{tce}}$  are also plotted (black curve)). The maximum of each of these two curves occurs at a temperature close to the corresponding bulk demixing temperature denoted as  $T_d^{(n)}(\mathcal{C}_3)$ . (This slight deviation from  $T_d(\mathcal{C}_3)$  is due to the offset  $\Delta\mu_+$  from the liquid–vapor coexistence surface.) The green curve corresponding to  $\Delta\mathcal{C}_3 = \mathcal{C}_3 - \mathcal{C}_3^{\text{tce}} = 0.0087$  joins the black one at  $T/K \simeq T_d^{(n)}(\mathcal{C}_3)/K = 8.3925$ ; for lower temperatures both curves merge. Since for the green curve  $T_d^{(n)}(\mathcal{C}_3) > T_{\text{peak}} = 8.3346$ , the maximum of this curve is the same as the maximum of the black curve. However, for  $\Delta\mathcal{C}_3 = 0.0257$  the violet curve joins the black curve at the corresponding demixing temperature  $T_d^{(n)}(\mathcal{C}_3)/K = 8.2392$ , which is below the temperature  $T_{\text{peak}}$  of the peak.

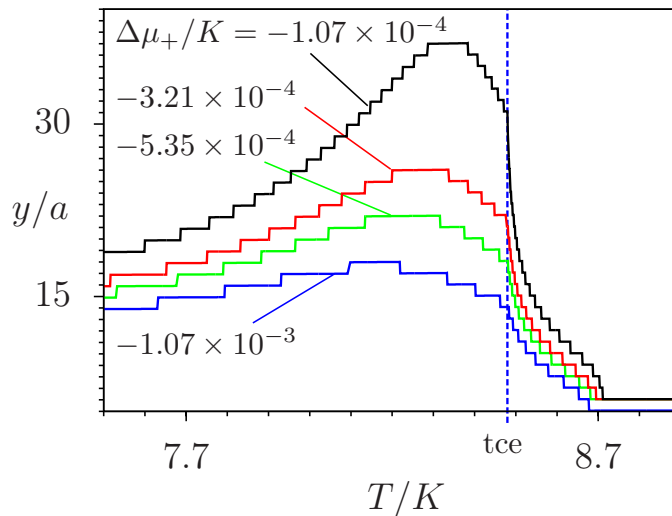


**Figure 5.15.** Equilibrium film thickness  $y$  over lattice constant  $a$  versus temperature  $T$  at  $\mathcal{C}_3 = \mathcal{C}_3^{\text{tce}}$  for four values of  $\Delta\mu_+/K$ . By increasing the offset value  $|\Delta\mu_+|$  the tricritical Casimir effect and complete wetting become less pronounced.

Therefore, the maximum of the violet curve differs from the maximum of the black curve. Figure 5.16 corresponds to panel (a) in Fig. 3.4. Note that  $X_t$  in Fig. 3.4 corresponds to  $\mathcal{C}_3^{\text{tce}}$  in the present notation.

Figure 5.17 shows the film thickness  $y$  over lattice constant  $a$  as function of temperature  $T$  for two values of  $\mathcal{C}_3 < \mathcal{C}_3^{\text{tce}}$  (red curve and blue curve; compare the inset in Fig. 5.13 with the same color code) and for  $\mathcal{C}_3^{\text{tce}}$  (black curve) at  $\Delta\mu_+/K = -1.07 \times 10^{-4}$ . The blue curve and the red curve merge with the black one at  $T_d$  close to the demixing temperature denoted as  $T_d^{(s)}(\mathcal{C}_3)$  in Fig. 5.13 (there is a slight deviation due to the offset from the liquid–vapor coexistence). Whereas for  $\mathcal{C}_3 \geq \mathcal{C}_3^{\text{tce}}$  the sudden drop of the film thickness occurs near  $T_d^{(n)}(\mathcal{C}_3)$  (note that  $T_d^{(s,n)}(\mathcal{C}_3^{\text{tce}}) = T_{\text{tce}}$ ), for  $\mathcal{C}_3 < \mathcal{C}_3^{\text{tce}}$  it takes place close to the bulk  $\lambda$ -transition temperature  $T_\lambda(\mathcal{C}_3) \geq T_{\text{tce}}$ . (Again, there is a slight deviation due to the offset from the liquid–vapor coexistence surface.) This sudden drop is associated with a break in slope in the curves  $y(T)$  and leads to the formation of characteristic shoulders. This agrees with the experimental observations (see panel (b) in Fig. 3.4). Note that because  $T_\lambda(\mathcal{C}_3)$  is a decreasing function of  $\mathcal{C}_3$ , for lower concentrations of  $^3\text{He}$ , the break in slope occurs at higher temperatures. For the red curve in Fig. 5.17, this shoulder is due to the emerging of the CCFs close to the  $\lambda$ -line. For even lower values of  $\mathcal{C}_3$  the films encounter only the CCFs due to the  $\lambda$ -transition and the TCFs due to the tricritical point do not influence them (see the blue curve). In Fig. 5.17 all curves attain their lowest value at the surface transition temperature  $T_s(\mathcal{C}_3) > T_\lambda(\mathcal{C}_3)$ .

The vertical paths at  $\mathcal{C}_3 < \mathcal{C}_3^{s*}$  (see Fig. 5.13) have not been studied in the present

## 5. Tricritical Casimir forces in $^3\text{He}$ - $^4\text{He}$ wetting films

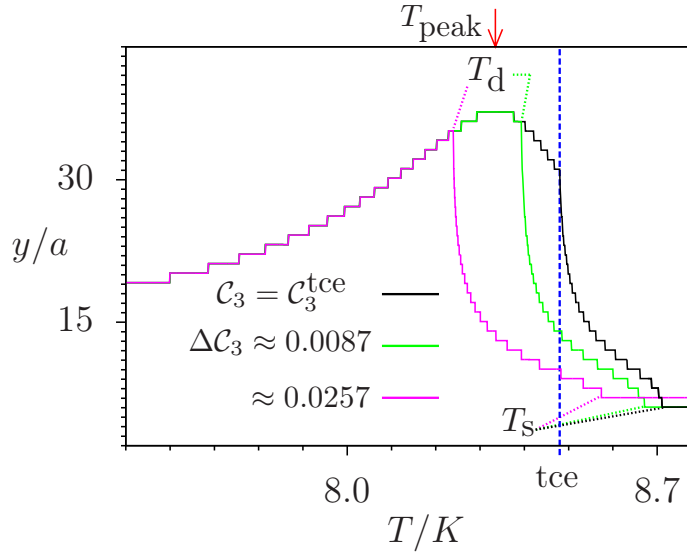


**Figure 5.16.** Equilibrium film thickness  $y$  over lattice constant  $a$  as function of temperature  $T$  for three values of  $\mathcal{C}_3 \geq \mathcal{C}_3^{\text{tce}}$ , i.e.,  $\Delta\mathcal{C}_3 = \mathcal{C}_3 - \mathcal{C}_3^{\text{tce}} \geq 0$ , and at  $\Delta\mu_+/K = -1.07 \times 10^{-4}$ . The sudden drop in the green and in the violet curve occurs at  $T_d$  close to the demixing temperature  $T_d^{(n)}(\mathcal{C}_3)$  (see Fig. 5.13 with the same color code). Below  $T_d^{(n)}(\mathcal{C}_3)$  the violet and the green curve merge with the black curve and follow the binodal denoted by  $T_d^{(n)}(\mathcal{C}_3)$  in Fig. 5.13. The black curve is similar to the one in Fig. 5.14 except that below  $T_{\text{tce}}$  it follows the normal branch of the binodal (see Fig. 5.4(c)). The jumps are due to first-order layering transitions. This figure corresponds to panel (a) in Fig. 3.4. Note that  $X$  and  $X_t$  in Fig. 3.4 correspond to  $\mathcal{C}_3$  and  $\mathcal{C}_3^{\text{tce}}$  here, respectively. Due to the offset from liquid-vapor coexistence the values of  $T_d$  and  $T_s$  differ slightly from  $T_d^{(n)}(\mathcal{C}_3)$  and  $T_s(\mathcal{C}_3)$  as shown in Fig. 5.13. The bulk parameters of the system are the same as in Fig. 5.4(c) and Fig. 5.13. At the peak the temperature is  $T_{\text{peak}}/K = 8.3346$ .

thesis. For these thermodynamic paths, due to the symmetric  $(O, O)$  BCs for the superfluid OP (i.e.,  $M = 0$  at the wall and at the emerging liquid-vapor interface) one expects the occurrence of an *attractive* CCF; however, above the bulk critical temperature this cannot be captured within the present mean field approximation because for Dirichlet-Dirichlet BCs the resulting CCF is solely due to fluctuations beyond mean field theory [21, 22]. Although both black curves in Fig. 5.16 and 5.17 correspond to  $\mathcal{C}_3 = \mathcal{C}_3^{\text{tce}}$ , they differ slightly due to the infinitesimal difference of the thermodynamic paths for  $T < T_{\text{tce}}$ . In Fig. 5.16, for  $T < T_{\text{tce}}$  the thermodynamic paths follow the demixing line  $T_d^{(n)}(\mathcal{C}_3)$  infinitesimally on the normal fluid side, whereas in Fig. 5.17 for  $T < T_{\text{tce}}$  the thermodynamic paths run along the superfluid binodal  $T_d^{(s)}(\mathcal{C}_3)$ .

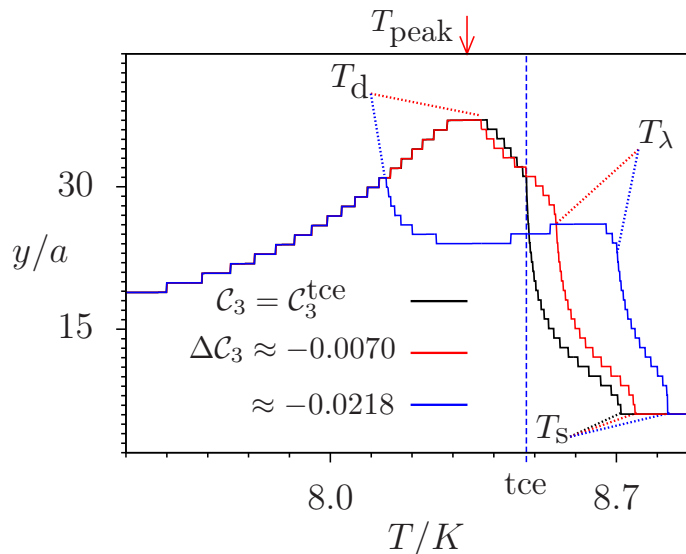


**Figure 5.17.** Equilibrium film thickness  $y$  over lattice constant  $a$  as function of temperature  $T$  for three values of  $C_3 \leq C_3^{\text{tce}}$  with  $\Delta C_3 = C_3 - C_3^{\text{tce}} \leq 0$  and at  $\Delta\mu_+/K = -1.07 \times 10^{-4}$ . The black curve is the same as the one in Fig. 5.14. The sudden drop in the blue and in the red curve occurs at  $T_\lambda$  close to the temperature of the  $\lambda$ -transition  $T_\lambda(C_3)$  (see Fig. 5.13). The red and the blue curve merge with the black curve at  $T_d$  and follow the binodal denoted by  $T_d^{(s)}(C_3)$  in Fig. 5.13. This figure corresponds to panel (b) in Fig. 3.4. Note that  $X$  and  $X_t$  in Fig. 3.4 correspond to  $C_3$  and  $C_3^{\text{tce}}$  here, respectively. Due to the offset from liquid–vapor coexistence the value of  $T_d$ ,  $T_s$ , and  $T_\lambda$  differ slightly from  $T_d^{(s)}(C_3)$ ,  $T_s(C_3)$ , and  $T_\lambda(C_3)$  as introduced in Fig. 5.13. The bulk parameters of the system are the same as in Fig. 5.4(c) and Fig. 5.13. At the peak the temperature is  $T_{\text{peak}}/K = 8.3346$ .

### 5.2.3. Tricritical Casimir forces

As discussed in Sec. 2.6, a fluid film exerts an effective force on its confining walls. For two parallel, planar walls a distance  $L$  apart this fluid mediated force  $F_s$  is given by [5]

$$F_s = - \left( \frac{\partial \mathcal{F}^{\text{ex}}}{\partial L} \right)_{T, \mu} = - \left( \frac{\partial (\mathcal{F} - V f_{\text{bulk}})}{\partial L} \right)_{T, \mu}, \quad (5.20)$$

where  $\mathcal{F}^{\text{ex}}$  is the excess free energy,  $f_{\text{bulk}}$  is the grand canonical bulk free energy density (per volume) of a one–component fluid at temperature  $T$  and chemical potential  $\mu$ , and  $\mathcal{F}$  is the free energy of the film of volume  $V = \mathcal{A}L$  where  $\mathcal{A}$  is the macroscopically large surface area of one wall. Since  $\mathcal{F} - V f_{\text{bulk}}$  is proportional to  $\mathcal{A}$ ,  $f_s = F_s/\mathcal{A}$  is the pressure in excess over its bulk value. Upon approaching the bulk critical point of the confined fluid,  $F_s$  acquires a *universal* long–ranged contribution  $F_C$ , known as the critical Casimir force [10, 73, 74].

Extending this concept to binary liquid mixtures, here one can focus on that contribution to  $F_s$  which arises near a tricritical point of  $^3\text{He}$ – $^4\text{He}$  mixtures. Let us call this

## 5. Tricritical Casimir forces in $^3\text{He}$ - $^4\text{He}$ wetting films

---

contribution tricritical Casimir force  $F_{\text{TCF}}$  (TCF) and express it in units of  $k_{\text{B}}T_{\text{tc}}$ , where  $T_{\text{tc}}$  is the temperature of a tricritical point on the line TC in Fig. 5.1.

As discussed in the Introduction, concerning wetting by a critical fluid, the critical fluctuations of the OP are confined by the solid substrate surface on one side and by the emerging liquid–vapor interface on the other side. Accordingly, the TCF is the derivative of the corresponding excess free energy with respect to the film thickness  $y$  at constant temperature and chemical potentials. In contrast to the slab geometry with two fixed walls as discussed above (see Eq. (5.20)), varying the equilibrium wetting film thickness requires to change the thermodynamic state of the fluid. Moreover, in the present microscopic approach the film thickness is not an input parameter of a model; hence, the excess free energy is not an explicit function of  $y$ . (Note that  $y$  is uniquely defined in terms of the equilibrium density profile  $D_l(T, \mu_+, \mu_-)$  via Eq. (5.18).) In order to calculate the TCF, let us consider a system at fixed  $T, \mu_+$ , and  $\mu_-$ , for which the film thickness is fixed to a specific value  $\ell$  by an externally imposed constraint. (For simplicity in the following the dependence of different quantities on the thermodynamic variables is not mentioned; only their dependence on the film thickness is considered.) Suppose that the thermodynamic variables are tuned such that the bulk phase is the vapor with the free energy density (per volume)  $f_{\text{b}}$ . The total free energy  $\mathcal{F}_{\text{cstr}}$  of such a constraint system of large size  $L$  can be written as [20, 22, 121]

$$\mathcal{F}_{\text{cstr}}(\ell)/A = f_{\text{m}}\ell + f_{\text{b}}(L - \ell) + \sigma_{\text{w,l}} + \sigma_{\text{l,v}} + f_{\text{ex}}(\ell), \quad (5.21)$$

where  $\sigma_{\text{w,l}}$  and  $\sigma_{\text{l,v}}$  are the wall–liquid and vapor–liquid surface tensions, respectively,  $f_{\text{m}}$  is the free energy density (per volume) of the metastable liquid at the same thermodynamic state ( $f_{\text{m}} > f_{\text{b}}$ ), and  $A := \mathcal{N}a^2$  is the cross section area of a layer. The  $\ell$ -dependent excess free energy density (per area)  $f_{\text{ex}}(\ell)$  is the sum of two contributions: the free energy density (per area)  $f_0(\ell)$  due to the effective interaction of the emerging liquid–vapor interface with the substrate wall and the singular contribution (per area)  $f_{\text{sing}}(\ell)$  due to the critical finite–size effects within the wetting film of thickness  $\ell$ . For short–ranged surface fields, the effective potential between the wall and the emerging liquid–vapor interface is an exponentially decaying function of the film thickness  $\ell$ . To leading order one has [122]

$$f_0(\ell) \approx \alpha \frac{T - T_{\text{w}}}{T_{\text{w}}} \exp(-p\ell), \quad (5.22)$$

where  $T_{\text{w}}$  is the wetting transition temperature and  $\alpha > 0$  is an amplitude such that in accordance with complete wetting (i.e., for  $T > T_{\text{w}}$ )  $f_0(\ell) > 0$ . The decay length  $1/p$  is the bulk correlation length of the liquid at  $T_{\text{w}}$  and at liquid–vapor coexistence. With the knowledge of  $f_{\text{ex}}(\ell)$  and  $f_0(\ell)$  one can determine the TCF via the negative derivative of

## 5.2. Layering and wetting for short-ranged surface fields

$f_{\text{ex}}(\ell) - f_0(\ell)$  with respect to  $\ell$ . Since  $y(T, \mu_+, \mu_-)$  is the equilibrium film thickness, the total free energy  $\mathcal{F}_{\text{cstr}}$  has a global minimum at  $y$ , so that  $\frac{\partial \mathcal{F}_{\text{cstr}}}{\partial \ell} \Big|_{\ell=y} = 0$ . Thus taking the derivative of both sides of Eq. (5.21) with respect to  $\ell$  at  $\ell = y$  yields

$$0 = f_{\text{m}} - f_{\text{b}} + \left. \frac{\partial f_0}{\partial \ell} \right|_{\ell=y} + \left. \frac{\partial f_{\text{sing}}}{\partial \ell} \right|_{\ell=y}. \quad (5.23)$$

With Eq. (5.22) this implies for the TCF

$$F_{\text{TCF}}(y)/A = \mathfrak{f}_{\text{TCF}}(y) = - \left. \frac{\partial f_{\text{sing}}}{\partial \ell} \right|_{\ell=y} \approx f_{\text{m}} - f_{\text{b}} - \alpha p \frac{T - T_{\text{w}}}{T_{\text{w}}} e^{-py}. \quad (5.24)$$

The parameters  $\alpha$ ,  $T_{\text{w}}$ , and  $p$  can be determined by studying the growth of the equilibrium film thickness as a function of the chemical potential sufficiently far above the critical demixing region, where  $F_{\text{TCF}}(y)$  is negligible. Using Eq. (5.24) and calculating  $f_{\text{m}}$  and  $f_{\text{b}}$  within the present model, it has been found that for the surface fields  $(\tilde{f}_+, \tilde{f}_-)/K = (10.714, 16.071)$  and the coupling constants  $(C/K, J/K, J_s/K) = (1, 9.107, 3.701)$ , one has  $T_{\text{w}}/K \simeq 3.704$ , whereas  $\alpha \simeq 1.146$ , and  $p \simeq 1.997$ . Note that the value of the bulk correlation length  $1/p$  agrees with the one following from the decay of the OP profiles.

In the slab geometry considered in Refs. [24, 25], the total number density of the  $^3\text{He}$ - $^4\text{He}$  mixtures is fixed and the properties of the system near the bulk tricritical point can be expressed in terms of the experimentally accessible thermodynamic fields  $T - T_{\text{tc}}$  and  $\mu_- - \mu_-^{\text{tc}}$ , where  $\mu_-^{\text{tc}}$  is the value of  $\mu_-$  at the tricritical point. (The thermodynamic field conjugate to the superfluid OP is experimentally not accessible and is omitted here.) As discussed in detail in Refs. [24, 25, 47], the proper dimensionless scaling fields are  $t \equiv (T - T_{\text{tc}})/T_{\text{tc}}$  and  $g \equiv (\mu_- - \mu_-^{\text{tc}})/(k_{\text{B}}T_{\text{tc}}) + a't$ , where  $a'$  is the slope of the line tangential to the phase boundary curve at  $T_{\text{tc}}$  within the blue surface in Fig. 5.1 (i.e., parallel to the intersection of the blue surface and  $A_4$  at tc which is the full blue horizontal line through tc). For such a choice of the scaling fields, for  $t \rightarrow 0$  with  $g = 0$  the tricritical point is approached tangentially to the phase boundary. According to finite-size scaling [8] the TCF for the slab of width  $L$  is governed by a universal scaling function defined as  $\tilde{\vartheta}_{+,O} \simeq L^3 \mathfrak{f}_{\text{TCF}}/(k_{\text{B}}T_{\text{tc}})$ , where the subscript  $\{+, O\}$  denotes the surface universality classes of the confining surfaces (the symbol “ $\simeq$ ” indicates asymptotic equality). The scaling function  $\tilde{\vartheta}_{+,O}$  depends on the two scaling fields  $c_1 t L^{1/\nu}$  and  $c_2 g L^{\Delta/\nu}$ , where  $c_1$  and  $c_2$  are nonuniversal metric factors and  $\nu = 1$  and  $\Delta = 2$  are tricritical exponents for the  $XY$  model in  $d = 3$  [43]. In order to facilitate a comparison with experimental data, the results for the TCF obtained in Refs. [24, 25] have been presented in terms of  $\tilde{\vartheta}_{+,O}$  only as a function of the single scaling variable  $c_1 t L^{1/\nu}$ , with  $c_1 = \xi_0^+/a$ ;  $\xi_0^+$  (in units of  $a$ ) is the amplitude of the superfluid OP correlation length  $\xi = \xi_0^+ t^{-\nu}$  above  $T_{\text{tc}}$ . In Refs. [24, 25], for thermodynamic paths of constant concentration, the influence

## 5. Tricritical Casimir forces in $^3\text{He}$ - $^4\text{He}$ wetting films

---

of the variation of the second scaling variable  $g$  upon changing temperature has been neglected.

In the present case of TCF emerging in wetting films of thickness  $y$ , the TCF per area is given by the universal scaling function  $\vartheta_{+,O}$  as

$$F_{\text{TCF}}/(Ak_{\text{B}}T_{\text{tc}}) = \mathfrak{f}_{\text{TCF}}/(k_{\text{B}}T_{\text{tc}}) \simeq y^{-d}\vartheta_{+,O}(c_1yt^\nu), \quad (5.25)$$

with  $t = (T - T_{\text{tce}})/T_{\text{tce}}$  and the spatial dimension  $d = 3$ , where again the dependence of  $\vartheta_{+,O}$  on the scaling variables associated with  $\mu_- - \mu_-^{\text{tce}}$  and  $\mu_+ - \mu_+^{\text{tce}}$  (which is conjugate to the total number density of the  $^3\text{He}$  -  $^4\text{He}$  mixture) has been neglected. In order to retrieve, however, the full information stored in the scaling function, in principle one has to plot the scaling function as a function of a single scaling variable, while keeping all the other scaling variables fixed. In practice this is difficult to realize. Along the thermodynamic paths taken experimentally in Ref. [17], none of the scaling variables were fixed. Instead the scaling functions have been plotted versus the single scaling variable  $td$ , where in Ref. [17]  $d$  denotes the film thickness. Here, this experimentally inspired approach is followed and  $y^3\mathfrak{f}_{\text{TCF}}/(k_{\text{B}}T_{\text{tce}})$  is plotted as a function of  $(y/a)t$ , ignoring the nonuniversal metric factor  $c_1$ . Since the surface fields chosen for our calculation of the TCF are strong, the dependence of the scaling function on the corresponding scaling variables can be neglected, assuming that for  $(\tilde{f}_+, \tilde{f}_-)/K = (10.714, 16.071)$  the system is close to the fixed point (+) BC.

Figures 5.18(a) and 5.19(a) show the scaling functions calculated from the data in Figs. 5.16 and 5.17, respectively. In order to eliminate the nonuniversal features arising from the jumps in the wetting films due to the layering transitions, these curves have been smoothed. Figure 5.20(a) shows the scaling functions for various values of  $\Delta\mu_+$  corresponding to the various curves in Fig. 5.15. The vertical blue dotted line in Figs. 5.18 - 5.20 represents the tricritical end point ( $t = 0$ ). Away from the tricritical temperature the scaling functions decay to zero. This decay is faster for temperatures higher than the tricritical temperature, i.e., for  $t > 0$ . For  $t > 0$  the dashed section of the blue curve in Fig. 5.19 shows that part, which is multivalued. This indicates that in this range of the scaling variable the scaling hypothesis is not applicable. The same holds also for the red curve in this figure, where the sudden drop exhibits a slightly positive slope.

In order to compare the present wetting results for the TCF with those obtained in the slab geometry as studied in Refs. [24,25], in the following a suitable slab approximation is employed for the wetting data. To this end, a slab of width  $L_0$  is considered, where  $L_0$  is defined as the equilibrium position of the emerging liquid-vapor interface of the wetting film  $L_0(T, \mu_+, \mu_-) = \lfloor y(T, \mu_+, \mu_-) \rfloor$ , at a certain value of the offset  $\Delta\mu_+$ . Since within the present lattice model the system size  $L_0$  must be an integer, the above assignment

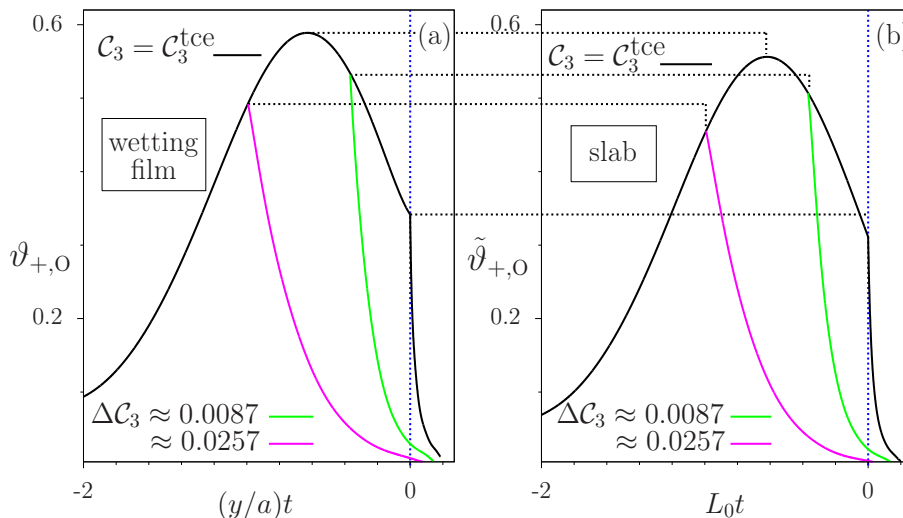


**Figure 5.18.** Scaling functions of the TCF calculated from the data in Fig. 5.16 within (a) the wetting film geometry and (b) the slab approximation. Concerning the definition of the slab thickness  $L_0$  see the main text. The violet curve and the green curve merge with the black curve at their corresponding demixing point indicated by  $T_d$  in Fig. 5.16, using the same color code. The corresponding curves in the two panels agree qualitatively but differ in detail, e.g., in height (see the horizontal lines). In panel (a) the thermodynamic states are off the liquid–vapor coexistence surface, whereas in panel (b) the thermodynamic states lie on the liquid–vapor coexistence surface. The reduced temperature is  $t = (T - T_{\text{tce}})/T_{\text{tce}}$ , where  $T_{\text{tce}}$  is the temperature of the tricritical end point. Due to the smoothing procedure and within the presently available numerical accuracy, the small difference between the positions of the maxima in (a) and (b) cannot be resolved reliably.

for  $L_0$  involves the floor function  $\lfloor \cdot \rfloor$ . ( $\lfloor x \rfloor$  is the largest integer number smaller than  $x$ .)

Within the slab approximation, the emerging liquid–vapor interface is replaced by a wall (denoted by ‘2’) with the short-ranged surface fields  $\tilde{f}_{+,2}$  and  $\tilde{f}_{-,2}$ . These surface fields are chosen such that the OP profiles calculated for the slab *at* liquid–vapor coexistence (i.e.,  $\Delta\mu_+ = 0$ ) resembles the ones within the wetting film geometry calculated for the semi-infinite system with an offset  $\Delta\mu_+ < 0$ . In order to obtain a perfect match, one would have to allow these surface fields to vary along the thermodynamic paths taken. Insisting, however, on fixed values of  $(\tilde{f}_{+,2}, \tilde{f}_{-,2})$ , it has been found that for  $(\tilde{f}_{+,2}, \tilde{f}_{-,2})/K = (1.607, 0.214)$  the profiles in the slab geometry agree rather well with their counterparts in the wetting film geometry. For  $(\tilde{f}_{+,2}, \tilde{f}_{-,2})/K = (1.607, 0.214)$  the number density  $X_{4,l}$  of  $^4\text{He}$  at the right boundary is not high enough for the spontaneous symmetry breaking of the superfluid OP to occur there. On the contrary, for  $(\tilde{f}_+, \tilde{f}_-)/K = (10.714, 16.071)$  at the left boundary  $M_l$  is nonzero. Accordingly, the two sets of surface fields induce  $(+, O)$  and thus non-symmetric BCs on the superfluid OP

## 5. Tricritical Casimir forces in ${}^3\text{He}$ - ${}^4\text{He}$ wetting films

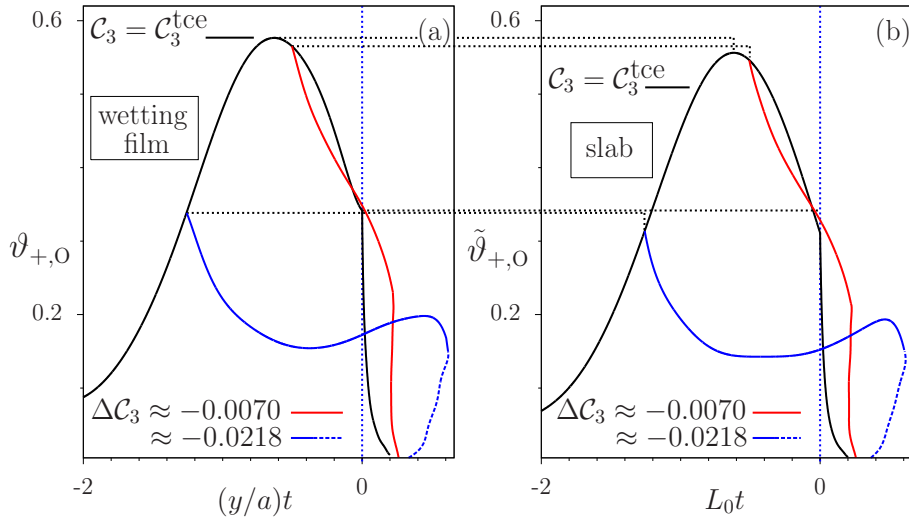


**Figure 5.19.** Scaling functions of the TCF calculated from the data in Fig. 5.17 within (a) the wetting film geometry and (b) the slab approximation. Concerning the definition of the slab thickness  $L_0$  see the main text. The blue curve and the red curve merge with the black curve at their corresponding demixing point, indicated by  $T_d$  in Fig. 5.17. The corresponding curves in the two panels agree qualitatively but differ in detail, e.g., in height (see the horizontal lines). The dashed blue curve shows the region, where the blue curve is multivalued and scaling does not hold anymore. The same holds also for the right parts of the red curves, because the drops of the curves exhibit a slightly positive slope. In panel (a) the thermodynamic states are off the liquid–vapor coexistence surface, whereas in panel (b) the thermodynamic states lie on the liquid–vapor coexistence surface. The reduced temperature is  $t = (T - T_{\text{tce}})/T_{\text{tce}}$ , where  $T_{\text{tce}}$  is the temperature of the tricritical end point. Due to the smoothing procedure and within the presently available numerical accuracy, the small difference between the positions of the maxima in (a) and (b) cannot be resolved reliably.

within the slab, giving rise to repulsive TCFs. For such a slab, by using Eq. (5.20) the TCF is calculated for that bulk thermodynamic state which is associated with the wetting film, but taken *at* bulk liquid–vapor coexistence (i.e.,  $\Delta\mu_+ = 0$ ). In this way one can mimic the actual experimental wetting situation and stay consistent with the calculations for the slab geometry as carried out in Refs. [24, 25]. Within lattice models, the smallest change in the system size amounts to one layer ( $\min(\Delta L_0) = 1$ ). Therefore, on the lattice the derivative in Eq. (5.20) has to be approximated by the finite difference

$$\mathfrak{f}_{\text{TCF}} = -\frac{\Delta f^{\text{ex}}(L_0)}{\Delta L_0} = -(f^{\text{ex}}(L_0 + 1) - f^{\text{ex}}(L_0)) \quad (5.26)$$

where  $f^{\text{ex}} = \mathcal{F}^{\text{ex}}/A$ . In order to determine  $f^{\text{ex}}(L_0)$ , one can write the total free energy  $\phi$  of the slab within thickness  $L_0$  as

$$\phi(L_0, T, \mu_+, \mu_-)/A = f_b L_0 + \sigma_{s,1}^{(1)} + \sigma_{s,1}^{(2)} + f^{\text{ex}}(L_0), \quad (5.27)$$

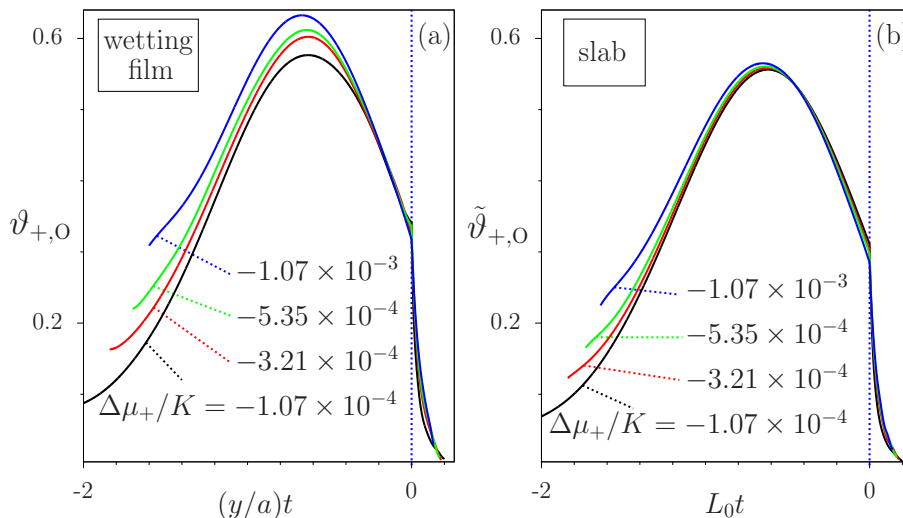


**Figure 5.20.** Scaling functions of the TCF calculated from the data in Fig. 5.15 within (a) the wetting film geometry and (b) the slab approximation. Concerning the definition of the slab thickness  $L_0$  see the main text. The maxima of the scaling functions in panel (a) differ from each other, whereas the ones in panel (b) are almost equal. The reduced temperature is  $t = (T - T_{\text{tce}})/T_{\text{tce}}$ , where  $T_{\text{tce}}$  is the temperature of the tricritical end point.

where  $\sigma_{\text{s},1}^{(1)}$  and  $\sigma_{\text{s},1}^{(2)}$  are the surface tensions between the liquid and surface (1) and surface (2), respectively. The surface tensions are functions of  $T, \mu_+$ , and  $\mu_-$  only and do not depend on the system size  $L_0$ . Using Eq. (5.27), Eq. (5.26) can be expressed as

$$\mathfrak{f}_{\text{TCF}} = (\phi(L_0) - \phi(L_0 + 1))/A + f_{\text{b}}. \quad (5.28)$$

Figures 5.18(b), 5.19(b), and 5.20(b) show the scaling functions  $\tilde{v}_{+,0}$  within the slab approximation, corresponding to the cases in panel (a) of each figure. Also here curves have been smoothed out in order to eliminate the discontinuities due to the layering transitions. The approximation of the derivative in Eq. (5.26) by a finite difference and a slight mismatch between the OP profiles in the slab and in the wetting film produce deviations in amplitude of the scaling functions comparable to the ones in panel (a) of each figure. In addition, these deviations might be caused by the difference between the thermodynamic paths taken in the two panels. In Fig. 5.19(b) the dashed section of the blue curve (with  $t > 0$ ) shows that part, for which the scaling hypothesis breaks down. This occurs for very small values of  $L_0$ , in particular above the tricritical end point, where the wetting film thickness is small, . This is in line with the general rule that universal scaling functions only hold in the scaling limit  $L_0 \gg a$ .



## 6. Summary

The present thesis is devoted to the study of the tricritical Casimir forces (TCFs) in wetting films of  $^3\text{He}$ - $^4\text{He}$  mixtures. Here a model has been proposed which enables one to provide a self-consistent description of wetting films and TCFs. The presently available, corresponding theoretical studies [24, 25] replace by fiat the wetting film with a slab of constant thickness, thereby losing certain important aspects of the problem. For example, so far the experimental data [17] for wetting film thicknesses as a function of temperature could not be addressed theoretically. This is possible within the present model. Moreover, the approach used in this thesis allows one to judge the quality of the commonly used slab approximation for wetting films in order to determine the universal scaling functions of critical and tricritical Casimir forces. The model proposed here is a vectorized three-dimensional spin-1 lattice model (vectorized Blume–Emery–Griffiths model [34–36]), which allows for the occurrence of vacant sites in addition to the lattice sites occupied by  $^3\text{He}$  and  $^4\text{He}$ . This enables the model to exhibit a vapor phase and thus allows for the occurrence of wetting films. Moreover, the proposed model incorporates vectorial degrees of freedom associated with the  $^4\text{He}$  atoms which covers the more complex behavior of the superfluid order parameter. The model has been studied within mean field theory.

The thesis starts with a brief review of the theoretical background (chapter 2). There by considering a ferromagnetic system as an example, critical phenomena, scaling hypotheses, universality, surface effects, and finite-size scaling have been reviewed. Moreover, tricritical scaling, wetting phenomena, the critical Casimir effect, and the effect of critical Casimir forces on wetting films have been discussed in separate sections.

Chapter 3 focuses on helium. In this chapter the bulk phase diagram of  $^4\text{He}$  and  $^3\text{He}$ - $^4\text{He}$  mixtures have been reviewed. This chapter includes a brief historical review about the discovery of superfluidity and its theoretical explanation. In this chapter a proper order parameter is introduced which describes the superfluid transitions of  $^4\text{He}$ ,

---

Parts of this chapter are reprinted with permission from [N. Farahmand Bafi, A. Maciołek, and S. Dietrich, *Phys. Rev. E* **95**, 032802 (2017).] Copyright 2017 by the American Physical Society and [N. Farahmand Bafi, A. Maciołek, and S. Dietrich, *Phys. Rev. E* **91**, 022138 (2015).] Copyright 2015 by the American Physical Society.

## 6. Summary

---

belonging to the bulk  $XY$  universality class. At the end of this chapter the experimental results [17] of the film thickness measurements in  $^3\text{He}$ - $^4\text{He}$  wetting films have been discussed.

The results of this thesis are presented in chapters 4 and 5. In chapter 4 the model has been proposed and the possible topologies of the bulk phase diagrams within the proposed model have been studied. These topologies depend on the choice of the coupling constants. Here the focus has been on those topologies of the phase diagram which are associated with liquid–liquid phase transitions at coexistence with the vapor phase. The knowledge of the bulk phase diagram is a prerequisite for studying tricritical Casimir forces in  $^3\text{He}$ - $^4\text{He}$  wetting films. The model exhibits a liquid phase, which can be either a superfluid or a normal liquid, and a vapor phase. If the coupling constant which facilitates the occurrence of the superfluid phase (the superfluid coupling constant) is turned off, the phase diagram is that of a normal binary liquid mixture (see Figs. 4.1 and 4.2). For nonzero but small values of the superfluid coupling constant the transitions to the superfluid phase are second order only (Figs. 4.3 and 4.6). For larger values of this coupling constant, the transition to the superfluid phase can also be of first order (Figs. 4.4, 4.7, and 4.8); the liquid–liquid phase transitions can be either between two normal liquids or between superfluid and normal liquids. For even larger values of the superfluid coupling constant, the first–order liquid–liquid phase transitions occur only between the superfluid and the normal fluid (Figs. 4.5 and 4.9), as it is the case for actual  $^3\text{He}$ - $^4\text{He}$  mixtures (see Figs. 3.1 - 3.3). It is interesting to note that the sequence of the phase diagrams (Fig. 4.6(a), 4.7(a), 4.8(a), 4.9(a)) exhibits the identical topologies as the phase diagrams of one–component dipolar fluids upon increasing the dipole strength with the isotropic and ferromagnetic liquid corresponding to the normal liquid and the superfluid, respectively [123, 124]. For dipolar fluids the solid phase can be captured by off-lattice density functional theory [125]. Similar topologies have been observed in off-lattice symmetrical binary fluid mixtures [126, 127].

In Chapter 5 the layering transitions, wetting films, and TCFs in  $^3\text{He}$ - $^4\text{He}$  mixtures have been studied within mean field approximation of the model proposed in chapter 4 but on a semi-infinite three-dimensional lattice. Furthermore, short–ranged surface fields  $f_+$  and  $f_-$  have been added to the model, which couple to the sum and the difference of the number densities of the  $^3\text{He}$  and  $^4\text{He}$  atoms, respectively; these surface fields facilitate the occurrence of wetting phenomena and can control the preference of the surface for the species.

The effect of the surface fields on wetting films has been studied for zero values of the superfluid coupling constant (i.e., for classical binary liquid mixture). Depending on the values of  $f_+$  and  $f_-$ , in the vapor phase very close to liquid–vapor coexistence the model exhibits incomplete or complete wetting (Figs. 5.6 - 5.8). Due to the lattice character of

---

the present model, one observes also first-order layering transitions (Figs. 5.9 and 5.10).

For suitable values of the surface fields and for the coupling constants, which determine the bulk phase diagram of the  $^3\text{He}$ - $^4\text{He}$  mixtures, it is possible to reproduce qualitatively the experimental results (see Fig. 3.4) for the thickness of  $^3\text{He}$ - $^4\text{He}$  wetting films near the tricritical end point [17]. Although the measurements in Refs. [17] have been performed in the regime of complete wetting, due to gravity the thickness of the wetting films remained finite. In the present study this has been achieved by applying an offset to the experimental thermodynamic paths (Fig. 5.2) and shifting them into the vapor phase so that the resulting wetting films remain finite (Figs. 5.1 and 5.3). Within the present mean field approach the order parameter profiles at a given thermodynamic state provide all equilibrium properties of the wetting films (Fig. 5.12). The closer the system to liquid-vapor coexistence is, the thicker the wetting films are (Fig. 5.11). Depending on the thermodynamic state, the wetting films can be superfluid. For the bulk phase corresponding to the normal fluid, the onset of superfluidity occurs by crossing a line of continuous surface transitions (Fig. 5.13).

Taking thermodynamic paths (Fig. 5.13) equivalent to the experimental ones taken in Ref. [17], it is possible to reproduce qualitatively the experimental results for the variation of the film thickness upon approaching the tricritical end point. Since the tricritical end point lies between the wetting temperature and the critical point of the liquid-vapor phase transitions, there is a pronounced change in the thickness of the wetting film due to repulsive TCFs (Figs. 5.14, 5.15, 5.16, and 5.17). The repulsive nature of the TCF is due to the effectively non-symmetric boundary conditions for the superfluid order parameter. The non-symmetric boundary conditions arise due to the formation of a  $^4\text{He}$ -rich layer near the solid-liquid interface, which can become superfluid even at temperatures above the  $\lambda$ -transition; at the liquid-vapor interface such a superfluid layer does not form because the  $^4\text{He}$  concentration is too low there. This leads to  $(+, O)$  boundary conditions. Such boundary conditions hold below the line  $T_s(\mathcal{C}_3)$  of continuous surface transitions (blue curve in Fig. 5.13) up to the special point  $s^*$  (i.e., for  $\mathcal{C}_3 > \mathcal{C}_3^{s^*}$ ). Like the experimental data, upon decreasing the temperature along the thermodynamic paths at fixed  $\mathcal{C}_3$  in the region  $\mathcal{C}_3^{s^*} < \mathcal{C}_3 < \mathcal{C}_3^{\text{tce}}$ , in addition to the repulsive TCFs close to tce, the wetting films are also influenced by the repulsive critical Casimir forces (CCFs) close to the  $\lambda$ -line  $T_\lambda(\mathcal{C}_3)$  (red line in Fig. 5.13). This gives rise to the formation of a shoulderlike curve in Figs. 5.17 and 3.4(b) between the tricritical end point and the  $\lambda$ -transition temperature. The thermodynamic paths at  $\mathcal{C}_3 < \mathcal{C}_3^{s^*}$  have not been explored in the present thesis. For  $\mathcal{C}_3 < \mathcal{C}_3^{s^*}$  the wetting film resembles that of pure  $^4\text{He}$ , for which the superfluid order parameter vanishes both at the solid substrate and at the liquid-vapor interface. Such symmetric  $(O, O)$  boundary conditions lead to an attractive CCF, which results in the decrease of the wetting film thickness close to

## 6. Summary

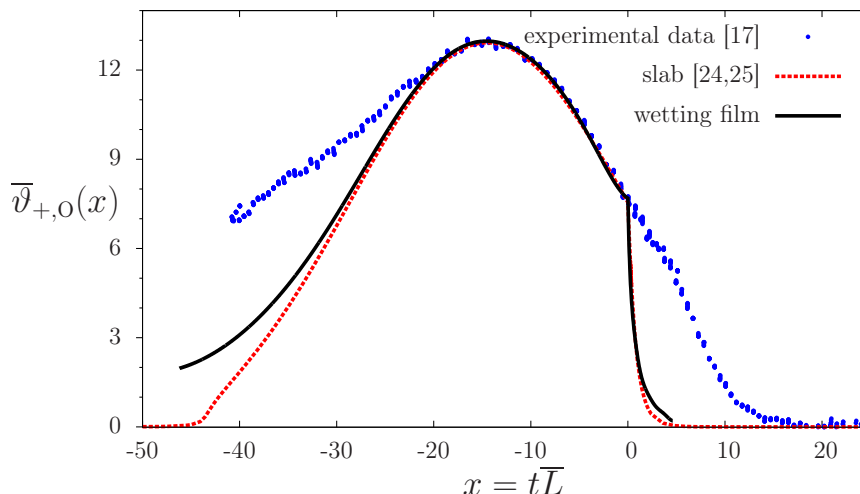


**Figure 6.1.** Adjusted scaling functions (see the main text) obtained for the slab geometry as in Refs. [24, 25] and inferred from the wetting films compared with the corresponding experimental curve [17]. All data correspond to the tricritical concentration of  ${}^3\text{He}$ .  $\bar{L}$  is the film thickness of the wetting films, whereas in Refs. [24, 25] it denotes the width of the slab. The reduced temperature  $t = (T - T_{\text{tc}})/T_{\text{tc}}$  is relative to tricritical point in Refs. [24, 25] and relative to the tricritical end point for the wetting film. (The experimental data [17] and the data from the slab geometry [24, 25], as well as the permission for reprinting them have been obtained from the authors of the corresponding references.)

the  $\lambda$ -transition temperature  $T_\lambda(\mathcal{C}_3)$  (see the dip in Fig. 3.4(c)). Above the bulk critical temperature, however, because the attractive CCF due to  $(O, O)$  boundary conditions is generated by fluctuations only [22] it cannot be captured within the present mean field approach.

Using the various contributions to the total free energy, one can calculate the TCFs and their scaling function by extracting the excess free energy from the total free energy (Figs. 5.18(a), 5.19(a), and 5.20(a)). Moreover, the slab approximation for the wetting films has been adapted to the present system and the corresponding slab scaling function of the TCF have been calculated (Figs. 5.18(b), 5.19(b), and 5.20(b)). It has been found that the slab approximation, with fixed surface fields at the second wall mimicking the emerging liquid–vapor interface, captures rather well the qualitative behavior of the scaling functions inferred from the wetting film thickness (see the comparison between the panels (a) and (b) in Figs. 5.18 - 5.20).

In order to conclude, the scaling function inferred from the wetting film thickness and the one calculated within the slab geometry as in Refs. [24, 25] are compared with the experimental data [17], specifically at the tricritical concentrations  $\mathcal{C}_3^{\text{tce}}$  of  ${}^3\text{He}$ . Figure 6.1 illustrates this comparison.  $\bar{L}$  refers to the wetting film thickness taken from the

---

experimental data or calculated within the present model. In Refs. [24, 25]  $\bar{L}$  refers to the slab width. In the reduced temperature  $t = (T - T_{\text{tc}})/T_{\text{tc}}$ ,  $T_{\text{tc}}$  refers to the temperature of the tricritical end point both in the present calculation and in the experimental studies, whereas it denotes the tricritical temperature in Refs. [24, 25]. The theoretical scaling functions are rescaled such that their values at  $t = 0$  match the experimental one. Moreover, the scaling variable  $x = t\bar{L}$  for the theoretical results is multiplied by a suitable factor such that the positions of the maxima of the theoretical curves match the experimental one. This factor is  $b_{\text{wf}} \simeq 23.10$  for the wetting film, whereas for the slab geometry it is  $b_{\text{slab}} \simeq 15.38$ . The resulting adjusted scaling functions  $\bar{\vartheta}_{+,O}(x)$  agree with each other and reproduce rather well the experimental data, especially near the maximum. In contrast, if these two adjustments of the scaling function are enforced for the one obtained within the slab approximation inferred from the wetting films (i.e., the black curve in panel (b) of Fig. 5.19), there is no satisfactory agreement with the experimental data as a whole (this adjusted scaling function is not shown in Fig. 6.1).

The present model lends itself to further investigations based on Monte Carlo simulations. They would capture the effects of fluctuations beyond the present mean field theory. Since the upper critical dimension for tricritical phenomena is  $d^* = 3$ , this would shed additional light on the reliability of the present mean field analysis. Moreover, in view of the ubiquity of van der Waals interactions it will be rewarding to extend the present model by incorporating long-ranged surface fields.



## 7. Zusammenfassung

Die vorliegende Arbeit widmet sich der Untersuchung der trikritischen Casimir-Kräfte, die in Benetzungsfilmen von  $^3\text{He}$ - $^4\text{He}$ -Mischungen beobachtet wurden. Hier wird ein Modell vorgeschlagen, welches eine selbstkonsistente Beschreibung von Benetzungsfilmen und trikritischen Casimir-Kräften ermöglicht. Die derzeit verfügbaren entsprechenden theoretischen Arbeiten [24, 25] ersetzen die Benetzungsschicht durch planparallele Platten konstanten Abstandes, wodurch gewisse wichtige Aspekte des Problems verloren gehen. Zum Beispiel konnten die experimentellen Daten für die Benetzungsfilmstärke als Funktion der Temperatur bislang theoretisch nicht reproduziert werden. Dies ist mit dem Modell in der vorliegenden Arbeit möglich. Außerdem ist es mit dem Ansatz aus dieser Arbeit möglich, die Qualität der häufig verwendeten Spalt-Näherung für Benetzungsfilme zu beurteilen. Das in dieser Arbeit vorgeschlagene Modell ist ein dreidimensionales Spin-1-Gittergasmodell (general vectorized Blume-Emery-Griffiths model [34–36]), welches neben durch  $^3\text{He}$  und  $^4\text{He}$  besetzte Gitterplätze auch unbesetzte Gitterplätze erlaubt. Dies erweitert das Modell um die Dampfphase und erlaubt somit das Auftreten von Benetzungsfilmen. Außerdem enthält das Modell vektorielle Freiheitsgrade, die das komplexe Verhalten des superfluiden Ordnungsparameters berücksichtigen. Das Modell wurde in Molekularfeldnäherung behandelt.

Die Arbeit beginnt mit einem kurzem Überblick über den theoretischen Hintergrund (Kapitel 2). Dort wurden am Beispiel eines Ferromagneten kritische Phänomene, die Skalierungshypothesen, Universalität, Oberflächen-Effekte und das Finite-Size-Skalenverhalten diskutiert. Darüber hinaus wurden die trikritische Skalierung, Benetzungsphänomene, der kritische Casimir-Effekt, und die Wirkung der kritischen Casimir-Kräfte auf Benetzungsfilme diskutiert.

Kapitel 3 konzentriert sich auf Helium. In diesem Kapitel werden das Phasendiagramm von  $^4\text{He}$  und  $^3\text{He}$ - $^4\text{He}$ -Mischung vorgestellt. Dieses Kapitel enthält einen kurzen geschichtlichen Überblick über die Entdeckung der Superfluidität und ihrer theoretischen Erklärung. In diesem Kapitel wird ein Ordnungsparameter eingeführt, der die superfluiden Übergänge von  $^4\text{He}$ , die zur  $XY$  Universalitätsklasse gehören, beschreibt. Am Ende dieses Kapitels werden die experimentellen Ergebnisse [17] der Schichtdickenmessungen in  $^3\text{He}$ - $^4\text{He}$ -Benetzungsfilmen diskutiert.

Die Ergebnisse dieser Arbeit werden in den Kapiteln 4 und 5 diskutiert. Im Kapitel 4

## 7. Zusammenfassung

---

wird das Modell vorgeschlagen und die möglichen Topologien der Bulk-Phasendiagramme untersucht. Diese Topologien hängen von den Kopplungskonstanten ab. Hierbei liegt der Fokus auf jenen Topologien, welche sich auf Flüssig-Flüssig-Phasenübergänge bei gleichzeitiger Koexistenz mit der Dampfphase beziehen. Ihre Kenntnis ist eine Voraussetzung für das Studium der trikritischen Casimir-Kräfte in  $^3\text{He}$ - $^4\text{He}$ -Benetzungsfilmen. Das Modell weist eine superfluide Phase und eine normale flüssige Phase auf. Darüber hinaus existiert eine Dampfphase. Wenn die Kopplungskonstante, welche das Auftreten der superfluiden Phase ermöglicht (superfluide Kopplungskonstante), ausgeschaltet wird, ist das Phasenverhalten identisch zu einer klassischen binären Mischung (siehe Abb. 4.1 und 4.2). Für kleine Werte der superfluiden Kopplungskonstante sind die Übergänge zur superfluiden Phase von zweiter Ordnung (Abb. 4.3 und 4.6). Für größere Werte kann der Übergang auch von erster Ordnung sein (Abb. 4.4, 4.7, und 4.8). Die flüssig-flüssig-Phasenübergänge können entweder zwischen zwei normalen Flüssigkeiten oder zwischen einer superfluiden und einer normalen Flüssigkeiten stattfinden. Für noch größere Werte der superfluiden Kopplungskonstanten treten die flüssig-flüssig-Phasenübergänge erster Ordnung nur zwischen dem Superfluid und dem Normalfluid auf (Abb. 4.5 und 4.9), wie es auch in realen  $^3\text{He}$ - $^4\text{He}$ -Mischungen der Fall ist (siehe Abb. 3.1 - 3.3). Interessanterweise zeigen die Phasendiagramme (Abb. 4.6(a), 4.7(a), 4.8(a) und 4.9(a)) die gleichen Topologien wie die Phasendiagramme von einkomponentigen dipolaren Flüssigkeiten bei Erhöhung der Dipolstärke. Hier entsprechen dann die isotrope und ferromagnetische Phase den Phasen flüssig und superfluid [123, 124]. Für dipolare Flüssigkeiten kann die feste Phase durch eine Kontinuums-Dichtefunktionaltheorie beschrieben werden [125]. Ähnliche Topologien wurden in Kontinuumsmodellen von symmetrischen binären Flüssigkeiten beobachtet [126, 127].

Im Kapitel 5 wurden die Layering-Übergänge, die Benetzungsfilme und die trikritischen Casimir-Kräfte in  $^3\text{He}$ - $^4\text{He}$ -Mischungen innerhalb der Molekularfeldnäherung untersucht. Das vorgeschlagene Modell in diesem Kapitel ist ähnlich wie das im Kapitel 4, außer dass hier das Modell in einem halb-unendlichen dreidimensionalen Gitter untersucht wurde. Darüber hinaus wurden dem Modell kurzreichweitige Oberflächenfelder  $f_+$  und  $f_-$  hinzugefügt, die an die Summe und die Differenz der Teilchenanzahldichten der  $^3\text{He}$  und  $^4\text{He}$  koppeln; diese Felder ermöglichen das Auftreten von Benetzungsphänomenen und darüber hinaus kann durch sie die von der Oberfläche bevorzugte Spezies kontrolliert werden.

Die Wirkung der Oberflächenfelder auf die Benetzungsfilme wurde für verschiedene Werte der superfluiden Kopplungskonstante untersucht (d.h. für klassische binäre Mischungen). In der Dampfphase zeigt das Modell in der Nähe der Flüssig-Dampf-Koexistenz sowohl eine partielle, als auch eine vollständige Benetzung des Substrates, je nach Wahl der Werte für die Feldstärken  $f_+$  und  $f_-$  (Abb. 5.6 - 5.8). Aufgrund des Git-

---

tercharakters des hier verwendeten Modells wird auch sogenanntes Layering beobachtet, welches aber keine Einschränkung in der Interpretation der Ergebnisse darstellt (siehe Abb. 5.9 und 5.10).

Für geeignete Werte der Oberflächenfelder und der Kopplungskonstanten, welche das Phasendiagramm der  $^3\text{He}$  -  $^4\text{He}$ -Mischungen bestimmen, konnten die experimentellen Ergebnisse [17] für die Filmdicke nahe des trikritischen Endpunktes (siehe Abb. 3.4) qualitativ reproduziert werden. Obwohl die Messungen in Ref. [17] bei vollständiger Benetzung durchgeführt wurden, bleibt die Filmdicke aufgrund der Schwerkraft endlich. In der vorliegenden Studie wird dies durch die Verwendung eines verschobenen thermodynamischen Pfades erreicht (Abb. 5.2), sodass die resultierenden Benetzungsfilme endlich bleiben (Abb. 5.1 und 5.3). Innerhalb der Molekularfeldnäherung beinhalten die Profile der Ordnungsparameter alle Gleichgewichtseigenschaften der Benetzungsfilme (Abb. 5.12). Je näher das System an der Flüssig-Dampf-Koexistenz ist, desto dicker sind die Benetzungsfilme (Abb. 5.11). In Abhängigkeit vom thermodynamischen Zustand können die Benetzungsfilme superfluid sein. Das Einsetzen der Superfluidität tritt durch Überqueren einer Linie von kontinuierlichen Oberflächenübergängen auf (Abb. 5.13).

Beim Verfolgen thermodynamischer Pfade (Abb. 5.13), welche äquivalent zu den experimentellen Messungen in Ref. [17] sind, ist es möglich die experimentellen Ergebnisse für die Veränderung der Filmdicke bei Annäherung an den trikritischen Endpunkt qualitativ zu reproduzieren. Der trikritische Endpunkt liegt zwischen der Benetzungstemperatur und dem kritischen Punkt der Dampf-Flüssigübergänge und daher ergibt sich eine ausgeprägte Änderung der Filmdicke aufgrund der abstoßenden trikritischen Casimir-Kraft (Abb. 5.14, 5.15, 5.16, und 5.17). Die repulsive Natur der trikritischen Casimir-Kraft ergibt sich aufgrund der effektiven nicht-symmetrischen Randbedingungen für den superfluiden Ordnungsparameter. Die nicht-symmetrischen Randbedingungen entstehen durch die Bildung einer  $^4\text{He}$ -reichen Schicht in der Nähe der Substrat-Flüssig-Grenzfläche, die schon bei Temperaturen oberhalb des  $\lambda$ -Übergangs superfluide werden kann; an der Flüssigkeits-Dampf-Grenzfläche bildet sich keine solche superfluide Schicht, weil die  $^4\text{He}$ -Konzentration dort zu niedrig ist. Dies führt zu  $(+, O)$  Randbedingungen. Solche Randbedingungen gelten unterhalb der Linie der kontinuierlichen Oberflächenübergänge (blaue Kurve in Abb. 5.13) bis zum *special point*  $s^*$  (d.h. für  $\mathcal{C}_3 > \mathcal{C}_3^{s^*}$ ).

Wie in den Experimenten, werden bei Abnahme der Temperatur entlang der thermodynamischen Pfade bei festem  $\mathcal{C}_3$  in der Region  $\mathcal{C}_3^{s^*} < \mathcal{C}_3 < \mathcal{C}_3^{\text{tce}}$  die Benetzungsfilme, zusätzlich zu den abstoßenden trikritischen Casimir-Kräften in der Nähe des trikritischen Endpunktes, auch durch die abstoßenden kritischen Casimir-Kräfte nahe der  $\lambda$ -Linie (rote Linie in Abb. 5.13) beeinflusst. Dadurch entsteht eine sattelförmige Kurve in den Abb. 5.17 und 3.4(b) zwischen dem trikritischen Endpunkt und der  $\lambda$ -

## 7. Zusammenfassung

---

Übergangstemperatur. Die thermodynamischen Pfade mit Konzentrationen  $\mathcal{C}_3 < \mathcal{C}_3^{s*}$  wurden in dieser Arbeit nicht untersucht. Für  $\mathcal{C}_3 < \mathcal{C}_3^{s*}$  ähnelt der Benetzungsfilm einem reinen  $^4\text{He}$ -Benetzungsfilm, für welches der superfluid Ordnungsparameter am festen Substrat und an der Flüssigkeit–Dampf–Grenzfläche verschwindet. Solche symmetrischen  $(O, O)$  Randbedingungen ergeben eine attraktive kritische Casimir–Kraft, die nahe der Temperatur des  $\lambda$ -Übergangs zu einer Verminderung der Benetzungsfilmstärke führt (siehe Abb. 3.4(c)). Allerdings kann wegen des in dieser Arbeit gewählten Molekularfeldansatzes diese attraktive kritische Casimir–Kraft oberhalb der kritischen Temperatur nicht erfasst werden.

Unter Verwendung der verschiedenen Beiträge zur gesamten freien Energie kann man die trikritischen Casimir Kräfte und deren Skalenfunktionen durch Extraktion der freien Exzessenergie aus der gesamten freien Energie berechnen (Abb. 5.18(a), 5.19(a) und 5.20(a)). Darüber hinaus wurde die Spalt–Näherung für die Benetzungsfilme an das neue System angepasst und die entsprechende Spalt–Skalenfunktion der kritischen Casimir Kraft berechnet (Abb. 5.18(b), 5.19(b) und 5.20(b)). Es stellt sich heraus, dass die Spalt–Näherung mit festen Oberflächenfeldern an der zweiten Wand, die die Flüssigkeit–Dampf–Grenzfläche imitiert, das qualitative Verhalten der von der Benetzungsschichtdicke abgeleiteten Skalenfunktion gut erfasst (siehe Abb. 5.18 - 5.20).

Abschließend wurden die von der Benetzungsschichtdicke abgeleiteten Skalenfunktion und die von Ref. [24, 25] mit den experimentellen Daten [17] verglichen, insbesondere für die trikritischen Konzentrationen  $\mathcal{C}_3^{\text{tcc}}$  von  $^3\text{He}$ . Abbildung 6.1 illustriert diesen Vergleich.  $\bar{L}$  bezieht sich auf die gemessene Benetzungsfilmstärke aus den experimentellen Daten oder die im vorliegenden Modell berechnete Benetzungsfilmstärke. In Ref. [24, 25] bezieht sich  $\bar{L}$  auf die Spaltbreite. In der reduzierten Temperatur  $t = (T - T_{\text{tc}})/T_{\text{tc}}$ , bezieht sich  $T_{\text{tc}}$  sowohl in der vorliegenden Arbeit als auch in den experimentellen Daten auf die Temperatur des trikritischen Endpunktes, während es in Ref. [24, 25] die trikritische Temperatur bezeichnet. Die theoretischen Skalierungsfunktionen wurden so skaliert, dass ihre Werte bei  $t = 0$  den experimentellen entsprechen. Außerdem wurde die Skalierungsvariable  $x = t\bar{L}$  für die theoretischen Ergebnisse mit einem geeigneten Faktor multipliziert, sodass die Positionen der Maxima der theoretischen Kurven denen der experimentellen entsprechen. Dieser Faktor ist  $b_{\text{wf}} \simeq 23.10$  für den Benetzungsfilm, während er für die Spalt–Geometrie  $b_{\text{slab}} \simeq 15.38$  beträgt. Die resultierenden, angepassten Skalierungsfunktionen  $\bar{\vartheta}_{+,O}(x)$  stimmen miteinander überein und reproduzieren die experimentellen Daten, insbesondere in der Nähe des Maximums sehr gut. Werden im Gegensatz dazu die beiden Anpassungen auf die aus der Benetzungsschicht erhaltenen Skalierungsfunktion (d.h. die von der schwarzen Kurve in der Tafel (b) von Abb. 5.19 erhaltenen Skalierungsfunktion) angewandt, ergibt sich keine befriedigende Übereinstimmung mit den experimentellen Daten als Ganzes (diese angepasste

---

Skalierungsfunktion ist in Abb. 6.1 nicht dargestellt).

Das vorliegende Modell eignet sich für weitere Untersuchungen auf der Grundlage von Monte-Carlo-Simulationen. Diese würden die Auswirkungen von Fluktuationen jenseits der gegenwärtigen Molekularfeldtheorie erfassen. Da die obere kritische Dimension für trikritische Phänomene  $d^* = 3$  ist, würde dies weiteren Aufschluss über die Zuverlässigkeit der vorliegenden Molekularfeldanalyse geben. Darüber hinaus wird es angesichts der Allgegenwart von van-der-Waals Wechselwirkungen lohnend sein, das vorliegende Modell durch die Einbeziehung langreichwertiger Oberflächenfelder zu erweitern.



# Acknowledgments

Foremost, I am very grateful to Prof. Dr. Siegfried Dietrich for giving me the opportunity to work in his group at the Max Planck Institute for Intelligent Systems. He not only guided me throughout my studies with his inspiring and insightful discussions, but also supported my parallel studies at the Musikhochschule Stuttgart.

I would like to thank Prof. Dr. Udo Seifert and Prof. Dr. Clemens Bechinger for the time they devoted as referee and examiner.

I am grateful to Dr. habil. Anna Maciołek for co-supervising this thesis. The discussions with her have always been very educative.

Special thanks are attributed to Dr. Markus Bier and Dr. Piotr Nowakowski for their great help and instructive discussions.

I would also like to express my gratitude to all my friends and my colleagues, among them Hendrik Bartsch, Dr. Zahra Eskandari, Irina Kistner, Marcel Labbé-Laurent, Dr. Adam Law, Dr. Paolo Margaretti, Dr. Pouya Moghimian, Dr. Thomas F. Mohry, Maximilian Mußotter, Dr. Mihail Popsecu, Dr. Faezeh Pousaneh, Andreas Reindl, Dr. Christian Rohwer, Dr. Lothar Schimmele, Dr. Swarn Lata Singh, Dr. Mykola Tasinkevych, Dr. Matthias Tröndle, and Dr. Thomas Weig. I also thank Anke Geigle for the administrative help which she provided during my studies.

Finally, I would like to thank my parents for their lasting love and support. I love to dedicate this thesis to them. Without them I could not have achieved anything of what I have.



# Appendices

## A. Scaling form of the Gibbs free energy

In this appendix the scaling form of the Gibbs free energy density in Eq. (2.12) is derived and some of the relations between the critical exponents are obtained. The starting point is the scaling hypothesis as discussed in Sec. 2.1. One way to implement the scaling hypothesis is to assume that the correlation function in Eq. (2.8) is expressed near the critical point as [4]

$$\Gamma(\mathbf{r} - \mathbf{r}')|_{t \rightarrow 0^\pm} \longrightarrow \left| \frac{1}{\mathbf{r} - \mathbf{r}'} \right|^{d-2+\eta} \mathcal{S}_\pm \left( \frac{|\mathbf{r} - \mathbf{r}'|}{\xi} \right), \quad (\text{A.1})$$

where  $\mathcal{S}_\pm$  is the scaling function and  $\pm$  indicates the regions above and under the critical point. Equation (A.1) is the scaling form of the correlation function for  $H = 0$  in terms of the scaling variable  $|\mathbf{r} - \mathbf{r}'|/\xi$ . In order to find the scaling form of the correlation function in the case of nonzero magnetic field one can argue that, since in the limit  $t \rightarrow 0$  the correlation length diverges, the effect of the nonzero magnetic field  $H$  is expected to be magnified by a power of the correlation length as  $H\xi^w$ . In this case the two relevant scaling variables are  $(|\mathbf{r} - \mathbf{r}'|/\xi, H\xi^w)$  or alternatively, by replacing  $\xi$  by  $t$  in  $H\xi^w$  (using Eq. (2.9)) the relevant scaling variables are  $(|\mathbf{r} - \mathbf{r}'|/\xi, H/|t|^\Delta)$ , where  $\Delta = \nu w$ . Therefore, in the presence of  $H$  one has

$$\Gamma(\mathbf{r} - \mathbf{r}', H)|_{t \rightarrow 0^\pm} \longrightarrow \left| \frac{1}{\mathbf{r} - \mathbf{r}'} \right|^{d-2+\eta} \mathcal{Q}_\pm (|\mathbf{r} - \mathbf{r}'|/\xi, H/|t|^\Delta), \quad (\text{A.2})$$

where  $\mathcal{Q}_\pm$  is the scaling function.

In order to find the scaling form of  $\chi$ , first one can rewrite Eq. (2.6) for  $d$  dimensions as

$$M/V = 1/V \left\langle \int d^d r m(\mathbf{r}) \right\rangle = 1/V \int d^3 r \frac{\text{Tr} [m(\mathbf{r}) e^{-\mathcal{H}/(k_B T)}]}{\text{Tr} [e^{-\mathcal{H}/(k_B T)}]}, \quad (\text{A.3})$$

where  $\text{Tr}$  denotes the trace over all possible states, and  $\mathcal{H}$  is the Hamiltonian of the system and  $e^{-\mathcal{H}/(k_B T)}/\text{Tr} [e^{-\mathcal{H}/(k_B T)}]$  is the Boltzmann distribution. For small values of the magnetic field  $H$  it can be assumed that  $H$  couples to the magnetic moments

linearly, so that the Hamiltonian can be written as [4]

$$\mathcal{H} = \mathcal{H}_0 - H \int d^d r' m(\mathbf{r}'), \quad (\text{A.4})$$

with  $\mathcal{H}_0$  being the Hamiltonian in the absence of the magnetic field  $H$ . Now taking the derivative of the left most and the right most expressions in Eq. (A.3) with respect to  $H$  and using Eqs.(2.3) and (2.7) one obtains

$$\chi = \frac{1}{k_B T} \int d^d r \Gamma(\mathbf{r} - \mathbf{r}'). \quad (\text{A.5})$$

Using Eqs. (A.2) and (A.5) one gets

$$\chi = \frac{1}{k_B T} \int d^d r \left| \frac{1}{\mathbf{r} - \mathbf{r}'} \right|^{d-2+\eta} \mathcal{Q}_{\pm}(|\mathbf{r} - \mathbf{r}'|/\xi, H/|t|^\Delta). \quad (\text{A.6})$$

By changing the integral variable to  $y := |\mathbf{r} - \mathbf{r}'|/\xi$  in the above equation, it follows that<sup>1</sup>

$$\chi = \frac{1}{k_B T} \int \xi^d d^d y |1/(y\xi)|^{d-2+\eta} \mathcal{Q}_{\pm}(y, H/|t|^\Delta). \quad (\text{A.7})$$

Therefore,  $\chi$  can be expressed via a scaling function  $\mathcal{R}_{\pm}$  as

$$\chi \sim \xi^{2-\eta} \mathcal{R}_{\pm}(H/|t|^\Delta). \quad (\text{A.8})$$

Replacing  $\xi$  by  $t$  in the above equation (by using Eq. (2.9)) and comparing it with the power-law for  $\chi$  in Eq. (2.5), results in the following relation between the critical exponents

$$\gamma = \nu(2 - \eta). \quad (\text{A.9})$$

According to this relation the scaling form of  $\chi$  can also be written as

$$\chi \sim |t|^{-\gamma} \mathcal{R}_{\pm}(H/|t|^\Delta). \quad (\text{A.10})$$

Due to Eq. (2.3) integrating the expression in Eq. (A.10) with respect to  $H$  renders the scaling form of  $M$  as<sup>2</sup>

$$\frac{M}{V} \sim |t|^{\Delta-\gamma} \mathcal{M}_{\pm}(H/|t|^\Delta), \quad (\text{A.11})$$

where  $\mathcal{M}_{\pm}$  is the scaling function. Comparing the above equation at  $H = 0$  with the power law of  $M$  as in Eq. (2.5) results in the relation

$$\Delta = \beta + \gamma. \quad (\text{A.12})$$

---

<sup>1</sup>Note that  $d^d y := d^d r / (\xi)^d$

<sup>2</sup>It is supposed that  $V$  is constant. Existence of  $V$  does not changes the power-laws in the following equations; it changes the scaling functions by a factor  $V$ .

## A. Scaling form of the Gibbs free energy

---

Integrating the expression in Eq. (A.11) with respect to  $H$  results in the scaling form of the Gibbs free energy  $G$  in terms of a scaling function  $\mathcal{P}_\pm$  as

$$\frac{G}{V} \sim |t|^{2\Delta-\gamma} \mathcal{P}_\pm(H/|t|^\Delta), \quad (\text{A.13})$$

which for  $H = 0$  leads to

$$G \sim |t|^{2\Delta-\gamma}. \quad (\text{A.14})$$

Using the definition of the heat capacity  $C_V$  (see Eq. (2.3)) along with Eqs. (2.4) and (A.14) it follows that

$$C_V \sim |t|^{2\Delta-\gamma-2}. \quad (\text{A.15})$$

According to the power-law for  $C_V$  as in Eq. (2.5) one has

$$\alpha + 2\beta + \gamma = 2. \quad (\text{A.16})$$

Using the relations between the critical exponents one obtains the following expression of the Gibbs free energy density  $g$

$$g = \frac{G}{V} \sim |t|^{2-\alpha} \mathcal{P}_\pm(H/|t|^\Delta), \quad (\text{A.17})$$

which is the Widom's scaling form for the Gibbs free energy [42].

The order parameter  $M$  is assumed to be finite at  $t = 0$  for nonzero  $H$ . In the limit  $t \rightarrow 0$  the expression on the right hand side of Eq. (A.11) remains finite only if the functionality of  $t$  in  $\mathcal{M}_\pm$  cancels the term  $|t|^{\Delta-\gamma}$ , which means that in the limit  $t \rightarrow 0$

$$\mathcal{M}_\pm(H/|t|^\Delta)|_{t \rightarrow 0} \sim (H/|t|^\Delta)^{\frac{\Delta-\gamma}{\Delta}}. \quad (\text{A.18})$$

Using Eqs. (A.11), (A.12) and (A.18) one obtains

$$M|_{t \rightarrow 0} \sim H^{\beta/\Delta}. \quad (\text{A.19})$$

Comparing Eq. (A.19) and the definition of the exponent  $\delta$  in Eq. (2.5) one gets [4]

$$\Delta = \beta\delta. \quad (\text{A.20})$$

Another relation between the exponents can be obtained by making an assumption known as *hyperscaling*, which assumes that the energy in a volume of the dimensions  $\xi$  (i. e.,  $V = \xi^d$  in  $d$  dimensions) is equal to  $k_B T$  with  $k_B$  being the Boltzmann constant [4]. Accordingly, the Gibbs free energy density  $g$  is in the order of  $k_B T / \xi^d$  and in the limit  $t \rightarrow 0$

$$g \sim \xi^{-d} \sim |t|^{d\nu}. \quad (\text{A.21})$$

Now comparing Eqs. (A.21) and (A.17) it follows that

$$2 - \alpha = d\nu. \quad (\text{A.22})$$

## B. Mean field approximation for the lattice model in section 5.1.1

In this appendix the details of the calculations outlined in Subsec. 5.1.1 are presented. The starting point is the Hamiltonian in Eq. (5.3). According to the variation principle, the equilibrium free energy  $F$  obeys the inequality [114]

$$F \leq \phi = \hat{\text{Tr}}(\rho \mathcal{H}) + (1/\beta) \hat{\text{Tr}}(\rho \ln \rho), \quad (\text{B.1})$$

where  $\rho$  is any trial density matrix fulfilling  $\hat{\text{Tr}}(\rho) = 1$ , with respect to which  $\phi$  on the right hand side of Eq. (B.1) has to be minimized in order to obtain the best approximation for  $F$ .

$$\hat{\text{Tr}} = \sum_{s_1=\pm 1,0} \int_0^{2\pi} d\Theta_1 \cdot \dots \cdot \sum_{s_{LN}=\pm 1,0} \int_0^{2\pi} d\Theta_{LN} \quad (\text{B.2})$$

denotes the trace and  $\beta = 1/T$  where  $T$  is the temperature times  $k_B$ . Within mean field theory, the total density matrix of the system factorizes as

$$\rho = \prod_{i=1}^{LN} \rho_i = \prod_{l=0}^{L-1} \prod_{v_l=1}^{\mathcal{N}} \rho_{(l,v_l)} \quad (\text{B.3})$$

with

$$\text{Tr} \rho_{(l,v_l)} = \sum_{s_{(l,v_l)}=\pm 1,0} \int_0^{2\pi} d\Theta_{(l,v_l)} \rho_{(l,v_l)}(s_{(l,v_l)}, \Theta_{(l,v_l)}) = 1, \quad (\text{B.4})$$

where  $l$  labels the  $L$  layers,  $v_l$  denotes the lattice sites within the  $l^{\text{th}}$  layer, and  $\rho_{(l,v_l)}$  denotes the density matrix of lattice site  $v_l$  within the layer  $l$ . (Note that  $\hat{\text{Tr}}$  denotes the trace over all degrees of freedom, whereas  $\text{Tr}$  refers to the trace over the degrees of freedom at a single lattice site.)

By applying mean field approximation to the sites within each layer,  $\rho_{(l,v_l)}$  is taken to be independent of  $v_l$ . Accordingly, Eq. (B.3) renders

$$\rho = \prod_{l=0}^{L-1} \rho_l^{\mathcal{N}}, \quad (\text{B.5})$$

with

$$\text{Tr} \rho_l = \sum_{s_l=\pm 1,0} \int_0^{2\pi} d\Theta_l \rho_l(s_l, \Theta_l) = 1, \quad (\text{B.6})$$

---

This appendix is reprinted with permission from [N. Farahmand Bafi, A. Maciołek, and S. Dietrich, Phys. Rev. E **95**, 032802 (2017).] Copyright 2017 by the American Physical Society.

## B. Mean field approximation for the lattice model in section 5.1.1

where  $\rho_l \equiv \rho_{(l,v_l)}$  indicates the density matrix for a single site in the  $l^{\text{th}}$  layer;  $s_l \equiv s_{(l,v_l)}$  and  $\Theta_l \equiv \Theta_{(l,v_l)}$  denote the occupation variable and the angle for a single site within this layer, respectively, independent of  $v_l$ . (Note that due to the definitions in Eq. (4.5), one has  $q_l \equiv q_{(l,v_l)}$  and  $p_l \equiv p_{(l,v_l)}$ .) The summations in Eq. (5.3) can be written as

$$\sum_{i=1}^{LN} = \sum_{l=0}^{L-1} \sum_{v_l=1}^{\mathcal{N}} = \mathcal{N} \sum_{l=0}^{L-1} \quad (\text{B.7})$$

and

$$\begin{aligned} \sum_{\langle i,j \rangle} &= \frac{1}{2} \sum_{i=1}^{\mathcal{N}} \left\{ \sum_{j \in \text{n.n.}(l)} + \sum_{j \in \text{n.n.}(l+1)} + \sum_{j \in \text{n.n.}(l-1)} (1 - \delta_{l,0}) \right\} \\ &= \frac{\mathcal{N}}{2} \sum_{l=0}^{L-1} \left\{ 4 + \sum_{j \in \text{n.n.}(l+1)} + \sum_{j \in \text{n.n.}(l-1)} (1 - \delta_{l,0}) \right\} \end{aligned} \quad (\text{B.8})$$

where  $\text{n.n.}(l)$ ,  $\text{n.n.}(l+1)$ , and  $\text{n.n.}(l-1)$  denote the nearest neighbors in the layers  $l$ ,  $l+1$ , and  $l-1$ , respectively. The factor  $1/2$  prevents double counting and the factor  $(1 - \delta_{l,0})$  appears due to the fact that layer  $l=0$  next to the surface does not have a neighboring layer at  $l=-1$ . Since the lattice sites within each layer are equivalent one has  $\sum_{j \in \text{n.n.}(l)} = 4$ .

By using Eq. (5.3) together with the above considerations, Eq. (B.1) renders

$$\begin{aligned} \phi &= -\mathcal{N} \sum_{l=0}^{L-1} \left[ \frac{K}{2} \langle s_l \rangle (4 \langle s_l \rangle + \langle s_{l+1} \rangle + \langle s_{l-1} \rangle (1 - \delta_{l,0})) \right. \\ &\quad + \frac{J}{2} \langle q_l \rangle (4 \langle q_l \rangle + \langle q_{l+1} \rangle + \langle q_{l-1} \rangle (1 - \delta_{l,0})) \\ &\quad + \frac{C}{2} \langle s_l \rangle (4 \langle q_l \rangle + \langle q_{l+1} \rangle + \langle q_{l-1} \rangle (1 - \delta_{l,0})) \\ &\quad + \frac{C}{2} \langle q_l \rangle (4 \langle s_l \rangle + \langle s_{l+1} \rangle + \langle s_{l-1} \rangle (1 - \delta_{l,0})) \\ &\quad + \frac{J_s}{2} \langle p_l \cos \Theta_l \rangle (4 \langle p_l \cos \Theta_l \rangle + \langle p_{l+1} \cos \Theta_{l+1} \rangle + \langle p_{l-1} \cos \Theta_{l-1} \rangle (1 - \delta_{l,0})) \\ &\quad + \frac{J_s}{2} \langle p_l \sin \Theta_l \rangle (4 \langle p_l \sin \Theta_l \rangle + \langle p_{l+1} \sin \Theta_{l+1} \rangle + \langle p_{l-1} \sin \Theta_{l-1} \rangle (1 - \delta_{l,0})) \\ &\quad \left. + \mu_- \langle s_l \rangle + \mu_+ \langle q_l \rangle + \langle f_-(l) s_l \rangle + \langle f_+(l) q_l \rangle \right] + (1/\beta) \langle \ln \prod_{l=0}^{L-1} \rho_l^{\mathcal{N}} \rangle, \end{aligned} \quad (\text{B.9})$$

where  $\langle \dots \rangle = \text{Tr}(\rho_l \dots)$  denotes the thermal average taken with the trial density matrix  $\rho_l$  associated with a single lattice site in layer  $l$ .

The last term in Eq. (B.9) can be written as

$$(1/\beta)\left\langle \ln \prod_{l=0}^{L-1} \rho_l^{\mathcal{N}} \right\rangle = (\mathcal{N}/\beta)\left\langle \sum_{l=0}^{L-1} \ln \rho_l \right\rangle. \quad (\text{B.10})$$

Minimizing the variational function  $\phi/\mathcal{N}$  with respect to  $\rho_l$  renders the best normalized functional form of  $\rho_l$  among the single-site, factorized density matrices. To this end, one can determine the functional derivative of  $\phi/\mathcal{N}$  in Eq. (B.9) with respect to  $\rho_l(s_l, \Theta_l)$  using  $\frac{\delta \rho_l(s_l, \Theta_l)}{\delta \rho_{l'}(s_{l'}, \Theta_{l'})} = \delta_{l,l'} \delta(\Theta_l - \Theta_{l'}) \delta_{s_l, s_{l'}}$ , and equate it to the Lagrange multiplier  $\eta$  corresponding to the constraint  $\text{Tr}(\rho_l) = 1$ :

$$\begin{aligned} \eta = \frac{\delta(\phi/\mathcal{N})}{\delta \rho_l(s_l, \Theta_l)} = & -K\{s_l(4X_l + X_{l+1} + X_{l-1}(1 - \delta_{l,0}))\} \\ & -J\{q_l(4D_l + D_{l+1} + D_{l-1}(1 - \delta_{l,0}))\} \\ & -C\{s_l(4D_l + D_{l+1} + D_{l-1}(1 - \delta_{l,0}))\} \\ & -C\{q_l(4X_l + X_{l+1} + X_{l-1}(1 - \delta_{l,0}))\} \\ & -(\mu_- + f_-(l))s_l - (\mu_+ + f_+(l))q_l \\ & -J_s\{p_l \cos \Theta_l(4M_l^x + M_{l+1}^x + M_{l-1}^x(1 - \delta_{l,0}))\} \\ & -J_s\{p_l \sin \Theta_l(4M_l^y + M_{l+1}^y + M_{l-1}^y(1 - \delta_{l,0}))\} \\ & + (1/\beta)(1 + \ln \rho_l) \end{aligned} \quad (\text{B.11})$$

where the following order parameters (OPs) are defined

$$\begin{aligned} X_l & := \langle s_l \rangle, \\ D_l & := \langle q_l \rangle, \\ M_l^x & := \langle p_l \cos \Theta_l \rangle, \\ M_l^y & := \langle p_l \sin \Theta_l \rangle. \end{aligned} \quad (\text{B.12})$$

Equation (B.11) can be solved for  $\rho_l(s_l, \Theta_l)$ :

$$\rho_l = e^{\beta\eta - 1 - \beta h_l}, \quad (\text{B.13})$$

where

$$\begin{aligned} h_l = & -s_l\{K(4X_l + X_{l+1} + X_{l-1}(1 - \delta_{l,0})) + C(4D_l + D_{l+1} + D_{l-1}(1 - \delta_{l,0})) + \mu_- + f_-(l)\} \\ & -q_l\{J(4D_l + D_{l+1} + D_{l-1}(1 - \delta_{l,0})) + C(4X_l + X_{l+1} + X_{l-1}(1 - \delta_{l,0})) + \mu_+ + f_+(l)\} \\ & -p_l \cos \Theta_l\{J_s(4M_l^x + M_{l+1}^x + M_{l-1}^x(1 - \delta_{l,0}))\} \\ & -p_l \sin \Theta_l\{J_s(4M_l^y + M_{l+1}^y + M_{l-1}^y(1 - \delta_{l,0}))\} \end{aligned} \quad (\text{B.14})$$

## B. Mean field approximation for the lattice model in section 5.1.1

---

is the effective single-site Hamiltonian for a lattice site in the  $l^{\text{th}}$  layer.

The normalization  $\text{Tr}(\rho_l) = 1$  yields

$$e^{-\beta\eta+1} = \text{Tr}(e^{-\beta h_l}) \quad (\text{B.15})$$

so that

$$\rho_l = \frac{e^{-\beta h_l}}{\text{Tr}(e^{-\beta h_l})}, \quad (\text{B.16})$$

where  $h_l$  is given by Eq. (B.14).

Within the expression for  $h_l$  given in Eq. (B.14) one has

$$\begin{aligned} \text{Tr}e^{-\beta h_l} = & 1 + W_l(X_l, D_l; \mu_-, \mu_+, f_+(l), f_-(l), T) \\ & + R_l(X_l, D_l; \mu_-, \mu_+, f_+(l), f_-(l), T)I_0(\beta J_s \tilde{M}_l), \end{aligned} \quad (\text{B.17})$$

where  $I_0$  and  $I_1$  are modified Bessel functions (see Subsec. 9.6 in Ref. [115]) and

$$\tilde{M}_l = \sqrt{(M_{l-1}^x(1 - \delta_{l,0}) + 4M_l^x + M_{l+1}^x)^2 + (M_{l-1}^y(1 - \delta_{l,0}) + 4M_l^y + M_{l+1}^y)^2}. \quad (\text{B.18})$$

The functions  $W(X_l, D_l; \mu_-, \mu_+, f_+(l), f_-(l), T)$  and  $R(X_l, D_l; \mu_-, \mu_+, f_+(l), f_-(l), T)$  are given by

$$\begin{aligned} W_l(X_l, D_l; \mu_-, \mu_+, f_+(l), f_-(l), T) = \exp \left\{ \beta \left[ (J - C)(D_{l-1}(1 - \delta_{l,0}) + 4D_l + D_{l+1}) \right. \right. \\ \left. \left. + (C - K)(X_{l-1}(1 - \delta_{l,0}) + 4X_l + X_{l+1}) \right. \right. \\ \left. \left. + \mu_+ + f_+(l) - \mu_- - f_-(l) \right] \right\} \end{aligned} \quad (\text{B.19})$$

and

$$\begin{aligned} R_l(X_l, D_l; \mu_-, \mu_+, f_+(l), f_-(l), T) = \exp \left\{ \beta \left[ (J + C)(D_{l-1}(1 - \delta_{l,0}) + 4D_l + D_{l+1}) \right. \right. \\ \left. \left. + (C + K)(X_{l-1}(1 - \delta_{l,0}) + 4X_l + X_{l+1}) \right. \right. \\ \left. \left. + \mu_+ + f_+(l) + \mu_- + f_-(l) \right] \right\}. \end{aligned} \quad (\text{B.20})$$

Using the definitions in Eq. (B.12) the OPs are given by four coupled self-consistent equations:

$$X_l = \frac{-W_l + R_l I_0(\beta J_s \tilde{M}_l)}{1 + W_l + R_l I_0(\beta J_s \tilde{M}_l)} \quad (\text{B.21})$$

and

$$D_l = \frac{W_l + R_l I_0(\beta J_s \tilde{M}_l)}{1 + W_l + R_l I_0(\beta J_s \tilde{M}_l)}; \quad (\text{B.22})$$

$M_l^x$  and  $M_l^y$  are given by

$$M_l^x = \frac{(1 - \delta_{l,0})M_{l-1}^x + 4M_l^x + M_{l+1}^x}{\tilde{M}_l} \frac{R_l I_1(\beta J_s \tilde{M}_l)}{1 + W_l + R_l I_0(\beta J_s \tilde{M}_l)} \quad (\text{B.23})$$

and

$$M_l^y = \frac{(1 - \delta_{l,0})M_{l-1}^y + 4M_l^y + M_{l+1}^y}{\tilde{M}_l} \frac{R_l I_1(\beta J_s \tilde{M}_l)}{1 + W_l + R_l I_0(\beta J_s \tilde{M}_l)} \quad (\text{B.24})$$

so that

$$M_l := \sqrt{(M_l^x)^2 + (M_l^y)^2} = \frac{R_l I_1(\beta J_s \tilde{M}_l)}{1 + W_l + R_l I_0(\beta J_s \tilde{M}_l)}. \quad (\text{B.25})$$

Since  $(M_l^x, M_l^y)$  and  $\tilde{M}_l$  are invariant under rotation around the  $z$ -axis, it is sufficient to consider only one of the two components. One can choose a rotation such that  $M_l^y = 0$  and  $M_l^x > 0$ . With this choice one has

$$\tilde{M}_l = (1 - \delta_{l,0})M_{l-1}^x + 4M_l^x + M_{l+1}^x \quad (\text{B.26})$$

and

$$M_l = \sqrt{(M_l^x)^2 + (M_l^y)^2} = M_l^x = \frac{R_l I_1(\beta J_s \tilde{M}_l)}{1 + W_l + R_l I_0(\beta J_s \tilde{M}_l)}. \quad (\text{B.27})$$

In order to determine the equilibrium free energy given in Eq. (B.9), first the term  $(1/\beta)\langle \ln \prod_{l=0}^{L-1} \rho_l^{\mathcal{N}} \rangle$  is rearranged as follows (see also Eq. (B.10))

$$\begin{aligned} (1/\beta)\left\langle \ln \prod_{l=0}^{L-1} \rho_l^{\mathcal{N}} \right\rangle &= (\mathcal{N}/\beta)\left\langle \sum_{l=0}^{L-1} \ln \rho_l \right\rangle = (\mathcal{N}/\beta) \sum_{l=0}^{L-1} \left\langle \ln \frac{e^{-\beta h_l}}{\text{Tr} e^{-\beta h_l}} \right\rangle \\ &= -\mathcal{N} \sum_{l=0}^{L-1} \langle h_l \rangle - (\mathcal{N}/\beta) \sum_{l=0}^{L-1} \left\langle \ln \text{Tr} e^{-\beta h_l} \right\rangle, \end{aligned} \quad (\text{B.28})$$

where in the last step, using Eqs. (B.17) and (B.22), one can write  $\text{Tr} e^{-\beta h_l} = (1 - D_l)^{-1}$ .

Inserting  $\rho_l$  into Eq. (B.9) with the choice  $M_l^y = 0$  and  $M_l^x > 0$  and taking into account Eq. (B.28) one obtains the following mean field expression for the equilibrium free energy:

$$\begin{aligned} \phi/\mathcal{N} &= \sum_{l=0}^{L-1} \left[ \frac{K}{2} X_l (4X_l + X_{l+1} + X_{l-1} (1 - \delta_{l,0})) \right. \\ &\quad + \frac{J}{2} D_l (4D_l + D_{l+1} + D_{l-1} (1 - \delta_{l,0})) \\ &\quad + \frac{C}{2} X_l (4D_l + D_{l+1} + D_{l-1} (1 - \delta_{l,0})) \\ &\quad + \frac{C}{2} D_l (4X_l + X_{l+1} + X_{l-1} (1 - \delta_{l,0})) \\ &\quad + \frac{J_s}{2} M_l^x (4M_l^x + M_{l+1}^x + M_{l-1}^x (1 - \delta_{l,0})) \\ &\quad \left. + (1/\beta) \ln(1 - D_l) \right]. \end{aligned} \quad (\text{B.29})$$

## B. Mean field approximation for the lattice model in section 5.1.1

---

Note that in the general case (i.e., for both  $M_l^y$  and  $M_l^x$  being nonzero) the contribution  $\sum_{l=0}^{L-1} \frac{J_s}{2} M_l^y (4M_l^y + M_{l+1}^y + M_{l-1}^y (1 - \delta_{l,0}))$  has to be added to the right hand side of Eq. (B.29).

In order to obtain the functional form of the expressions for the chemical potentials, first Eqs. (B.21) and (B.22) have to be solved for  $W_l$  and  $R_l$ . Then, by comparing these solutions with the definitions of  $W_l$  and  $R_l$  as in Eqs. (B.19) and (B.20), one finds

$$\begin{aligned} \mu_+ = & \frac{T}{2} \ln(D_l^2 - X_l^2) - T \ln 2 - T \ln(1 - D_l) - \frac{T}{2} \ln(I_0(\beta J_s \tilde{M}_l)) \\ & - J(D_{l-1}(1 - \delta_{l,0}) + 4D_l + D_{l+1}) - C(X_{l-1}(1 - \delta_{l,0}) + 4X_l + X_{l+1}) - f_+(l) \end{aligned} \quad (\text{B.30})$$

and

$$\begin{aligned} \mu_- = & \frac{T}{2} \ln \frac{D_l + X_l}{D_l - X_l} - \frac{T}{2} \ln(I_0(\beta J_s \tilde{M}_l)) \\ & - C(D_{l-1}(1 - \delta_{l,0}) + 4D_l + D_{l+1}) - K(X_{l-1}(1 - \delta_{l,0}) + 4X_l + X_{l+1}) - f_-(l). \end{aligned} \quad (\text{B.31})$$

Finally, one can implicitly express the magnetization  $M_l$  in terms of  $X_l$  and  $D_l$  by using Eqs. (B.21), (B.22), and (B.25):

$$\frac{X_l + D_l}{2} = \frac{M_l I_0(\beta J_s \tilde{M}_l)}{I_1(\beta J_s \tilde{M}_l)}. \quad (\text{B.32})$$



# Bibliography

- [1] H. Casimir, Proc. K. Ned. Akad. Wet **51**, 793 (1948).
- [2] M. E. Fisher and P. G. de Gennes, C. R. Seances Acad. Sci. Paris Ser. B **287**, 207 (1978).
- [3] K. Symanzik, Nucl. Phys. B **190**, 1 (1981).
- [4] K. Huang, *Statistical mechanics* (John Wiley and Sons, Inc., New York, second edition, 1987).
- [5] R. Evans, J. Phys.: Condens. Matter **2**, 8989 (1990).
- [6] M. Krech, *The Casimir effect in critical systems* (World Scientific, Singapore, 1994).
- [7] K. Binder, in *Phase Transitions and Critical Phenomena*, edited by C. Domb and J. L. Lebowitz (Academic, London, 1983), vol. 8, p. 1.
- [8] V. Privman, in *Finite Size Scaling and Numerical Simulation of Statistical Systems*, edited by V. Privman (World Scientific, Singapore, 1990), p. 1.
- [9] H. W. Diehl, in *Phase Transitions and Critical Phenomena*, edited by C. Domb and J. L. Lebowitz (Academic, London, 1986), vol. 10, p. 75.
- [10] J. G. Brankov, D. Danchev, and N. Tonchev, *Theory of critical phenomena in finite-size systems* (World Scientific, Singapore, 2000).
- [11] M. Fukuto, Y. F. Yano, and P. S. Pershan, Phys. Rev. Lett. **94**, 135702 (2005).
- [12] A. Mukhopadhyay and B. M. Law, Phys. Rev. Lett. **83**, 772 (1999).
- [13] A. Mukhopadhyay and B. M. Law, Phys. Rev. E **62**, 5201 (2000).
- [14] S. Rafai, D. Bonn, and M. J., Physica **386**, 31 (2007).
- [15] R. Garcia and M. H. W. Chan, Phys. Rev. Lett. **83**, 1187 (1999).

## Bibliography

---

- [16] A. Ganshin, S. Scheidemantel, R. Garcia, and M. H. W. Chan, Phys. Rev. Lett. **97**, 075301 (2006).
- [17] R. Garcia and M. H. W. Chan, Phys. Rev. Lett. **88**, 086101 (2002).
- [18] T. Ueno, S. Balibar, T. Mizusaki, F. Caupin, and E. Rolley, Phys. Rev. Lett. **90**, 116102 (2003).
- [19] M. P. Nightingale and J. O. Indekeu, Phys. Rev. Lett. **54**, 1824 (1985).
- [20] M. Krech and S. Dietrich, Phys. Rev. A **46**, 1922 (1992).
- [21] M. Krech and S. Dietrich, Phys. Rev. Lett. **66**, 345 (1991).
- [22] M. Krech and S. Dietrich, Phys. Rev. A **46**, 1886 (1992).
- [23] R. Zandi, J. Rudnick, and M. Kardar, Phys. Rev. Lett. **93**, 155302 (2004).
- [24] A. Maciołek, A. Gambassi, and S. Dietrich, Phys. Rev. E **76**, 031124 (2007).
- [25] A. Maciołek and S. Dietrich, Europhys. Lett. **74**, 22 (2006).
- [26] R. Zandi, A. Shackell, J. Rudnick, M. Kardar, and L. P. Chayes, Phys. Rev. E **76**, 030601(R) (2007).
- [27] O. Vasilyev, A. Gambassi, A. Maciołek, and S. Dietrich, EPL **80**, 60009 (2007).
- [28] O. Vasilyev, A. Gambassi, A. Maciołek, and S. Dietrich, Phys. Rev. E **79**, 041142 (2009).
- [29] D. Dantchev and M. Krech, Phys. Rev. E **69**, 046119 (2004).
- [30] A. Hucht, Phys. Rev. Lett. **99**, 185301 (2007).
- [31] M. Hasenbusch, J. Stat. Mech.: Theory and Experiment **2009**, P07031 (2009).
- [32] M. Hasenbusch, Phys. Rev. B **81**, 165412 (2010).
- [33] J. P. Romagnan, J. P. Laheurte, J. C. Noiray, and W. F. Saam, J. Low Temp. Phys. **30**, 425 (1978).
- [34] M. Blume, V. J. Emery, and R. B. Griffiths, Phys. Rev. A **4**, 1071 (1971).
- [35] A. N. Berker and D. R. Nelson, Phys. Rev. B **19**, 2488 (1979).
- [36] J. L. Cardy and D. J. Scalapino, Phys. Rev. B **19**, 1428 (1979).

- 
- [37] N. Goldenfeld, *Lectures on phase transitions and the renormalization group* (Westview press, Colorado, 1992).
- [38] H. E. Stanley, *Introduction to phase transitions and critical phenomena* (Oxford University Press, Oxford, 1971).
- [39] E. A. Guggenheim, *J. Chem. Phys.* **13**, 253 (1945).
- [40] K. G. Wilson, *Phys. Rev. B* **4**, 3174 (1971).
- [41] K. G. Wilson, *Phys. Rev. B* **4**, 3184 (1971).
- [42] B. Widom, *J. Chem. Phys.* **43**, 3898 (1965).
- [43] I. D. Lawrie and S. Sarbach, in *Phase Transitions and Critical Phenomena*, edited by C. Domb and J. L. Lebowitz (Academic, London, 1984), vol. 9, p. 2.
- [44] G. S. Radyshevskaya, N. I. Nikurashina, and R. V. Mertslin, *J. Gen. Chem. USSR* **32**, 673 (1962).
- [45] R. B. Griffiths, *Phys. Rev. B* **7**, 545 (1973).
- [46] R. B. Griffiths, *Phys. Rev. Lett.* **24**, 715 (1970).
- [47] E. K. Riedel, *Phys. Rev. Lett.* **28**, 675 (1972).
- [48] E. K. Riedel and F. J. Wegner, *Phys. Rev. Lett.* **29**, 349 (1972).
- [49] A. Hankey, H. E. Stanley, and T. S. Chang, *Phys. Rev. Lett.* **29**, 278 (1972).
- [50] L. S. Schulman, *Phys. Rev. B* **7**, 1960 (1973).
- [51] A. Hankey and H. E. Stanley, *Phys. Rev. B* **6**, 3515 (1972).
- [52] L. P. Kadanoff et al., *Rev. Mod. Phys.* **39**, 395 (1967).
- [53] T. C. Lubensky and M. H. Rubin, *Phys. Rev. B* **12**, 3885 (1975).
- [54] A. J. Bray and M. A. Moore, *J. Phys. A* **10**, 1927 (1977).
- [55] N. M. Švrakić and M. Wortis, *Phys. Rev. B* **15**, 396 (1977).
- [56] T. W. Burkhardt and E. Eisenriegler, *Phys. Rev. B* **16**, 3213 (1977).
- [57] H. W. Diehl, *Int. J. Mod. Phys. B* **11**, 3503 (1997).
- [58] M. E. Fisher and G. Caginalp, *Commun. Math. Phys.* **56**, 11 (1977).

## Bibliography

---

- [59] G. Caginalp and M. E. Fisher, *Commun. Math. Phys.* **65**, 247 (1979).
- [60] K. Binder and P. C. Hohenberg, *Phys. Rev. B* **6**, 3461 (1972).
- [61] K. Binder and P. C. Hohenberg, *Phys. Rev. B* **9**, 2194 (1974).
- [62] H. W. Diehl and E. Eisenriegler, *Europhys. Lett.* **4**, 709 (1987).
- [63] W. Speth, *Z. Phys. B Condens. Matter* **51**, 361 (1983).
- [64] G. Gumbs, *J. Math. Phys.* **24**, 202 (1983).
- [65] K. Binder and D. Landau, *Surf. Sci.* **61**, 577 (1976).
- [66] S. Dietrich, in *Phase Transitions in Surface Films 2, proceedings of the NATO ASI (Series B) held in Eric, Italy, 19-30 June 1990*, edited by H. Taub, G. Torzo, H. J. Lauter, and S. C. Fain (1991), vol. B 267, p. 391.
- [67] S. Dietrich, Wetting phenomena, in *Phase Transitions and Critical Phenomena*, edited by C. Domb and J. L. Lebowitz (Academic, London, 1988), vol. 12, p. 1.
- [68] R. Pandit, M. Schick, and M. Wortis, *Phys. Rev. B* **26**, 5112 (1982).
- [69] M. Schick, in *Les Houches, Sessions XLVIII–Liquides aux interfaces/Liquids at interfaces*, edited by J. Charvolin, J. F. Joanny, and J. Zinn-Justin (Elsevier, Amsterdam, 1990), p. 415.
- [70] M. N. Barber, in *Phase Transitions and Critical Phenomena*, edited by C. Domb and J. L. Lebowitz (Academic, London, 1983), vol. 8, p. 145.
- [71] M. E. Fisher and A. E. Ferdinand, *Phys. Rev. Lett.* **19**, 169 (1967).
- [72] M. Planck, *Verhandlungen der Deutschen Physikalischen Gesellschaft* **2**, 237 (1900).
- [73] M. Krech, *Phys. Rev. E* **56**, 1642 (1997).
- [74] A. Gambassi, *J. Phys.: Conf. Series* **161**, 012037 (2009).
- [75] B. M. Law, *Prog. Surf. Sci.* **66**, 159 (2001).
- [76] J. Wilks and D. S. Betts, *An Introduction to Liquid Helium* (Clarendon Press, Oxford, second edition, 1987).
- [77] H. Kamerlingh Onnes, *Commun. Phys. Lab. Univ. Leiden* **120b** (1911).

- 
- [78] B. Svistunov, E. Babaev, and N. Prokof'ev, *Superfluid States of Mater* (CRC Press, Boca Raton, 2015).
- [79] D. van Delft and K. Peter, *Phys. Today* **63**, 38 (2010).
- [80] W. H. Keesom and M. Wolfke, *Leiden. Commun.* **190b** (1927).
- [81] W. H. Keesom and M. Wolfke, *Proc. Roy. Acad. Sci. Amst.* **31**, 81 (1928).
- [82] W. H. Keesom and K. Clusius, *Proc. Roy. Acad. Sci. Amst.* **35**, 307 (1932).
- [83] W. H. Keesom and A. P. Keesom, *Proc. Roy. Acad. Sci. Amst.* **35**, 736 (1932).
- [84] E. F. Burton, *Nature* **135**, 265 (1935).
- [85] P. Kapitza, *Nature* **141**, 74 (1938).
- [86] J. F. Allen and A. D. Misener, *Nature* **141**, 75 (1938).
- [87] W. E. Keller, *Helium-3 and Helium-4* (Plenum Press, New York, 1969).
- [88] F. London, *Nature* **141**, 643 (1938).
- [89] F. London, *Phys. Rev.* **54**, 947 (1938).
- [90] A. Einstein, *Ber. Berl. Akad.* **261** (1924).
- [91] A. Einstein, *Ber. Berl. Akad.* **3** (1925).
- [92] S. N. Bose, *Z. Phys.* **26**, 178 (1924).
- [93] L. Tisza, *Nature* **141**, 913 (1938).
- [94] L. D. Landau, *Phys. Rev.* **60**, 356 (1941).
- [95] O. Penrose, *Phil. Mag.* **42**, 1373 (1951).
- [96] D. S. Greywall, *Phys. Rev. B* **27**, 2747 (1983).
- [97] J. M. Parpia, D. J. Sandiford, J. E. Berthold, and J. D. Reppy, *Phys. Rev. Lett.* **40**, 565 (1978).
- [98] H. W. Ahlers, in *The Physics of Liquid and Solid Helium, Part I*, edited by K. H. Bennemann and J. B. Ketterson (John Wiley and Sons, Inc., New York, 1976).
- [99] K. R. Atkins, *Liquid Helium* (Cambridge University Press, Cambridge, 1959).

## Bibliography

---

- [100] S. W. Van Sciver and O. E. Vilches, *Phys. Lett. A* **55**, 191 (1975).
- [101] S. W. Van Sciver, *Phys. Rev. B* **18**, 277 (1978).
- [102] P. Taborek and L. Senator, *Phys. Rev. Lett.* **57**, 218 (1986).
- [103] H. J. Lauter, H. Godfrin, C. Tiby, H. Wiechert, and P. E. Obermayer, *Surf. Sci.* **125**, 265 (1983).
- [104] S. E. Polanco, J. H. Quateman, and M. Bertz, *J. Phys. Colloques* **39**, C6-344 (1978).
- [105] S. E. Polanco and M. Bretz, *Surf. Sci.* **94**, 1 (1980).
- [106] M. Bienfait, J. G. Dash, and J. Stoltenberg, *Phys. Rev. B* **21**, 2765 (1980).
- [107] G. D. L. Webster, M. Chester, E. Webster, and T. Oestereich, *J. Low Temp. Phys.* **40**, 207 (1980).
- [108] D. Sornette and J. P. Laheurte, *J. Phys. France* **47**, 1951 (1986).
- [109] J. Sivardière and J. Lajzerowicz, *Phys. Rev. A* **11**, 2090 (1975).
- [110] S. Dietrich and A. Latz, *Phys. Rev. B* **40**, 9204 (1989).
- [111] T. Getta and S. Dietrich, *Phys. Rev. E* **47**, 1856 (1993).
- [112] D. Mukamel and M. Blume, *Phys. Rev. A* **10**, 610 (1974).
- [113] A. Maciołek, M. Krech, and S. Dietrich, *Phys. Rev. E* **69**, 036117 (2004).
- [114] P. M. Chaikin and T. Lubensky, *Principles of condensed matter physics* (Cambridge University Press, Cambridge, 1995).
- [115] M. Abramowitz and I. A. Stegun, eds., *Handbook of mathematical functions* (Dover, New York, 1972).
- [116] Wolfram Research, Inc., Mathematica, <http://www.wolfram.com/mathematica/>.
- [117] S. Wolfram, *The Mathematica Book* (Wolfram Media, Inc., Champaign, 2003, fifth edition).
- [118] M. Galassi et al., *GNU Scientific Library Reference Manual* (Network Theory Ltd., 2009, third edition).
- [119] GNU Scientific Library (GSL), <http://www.gnu.org/software/gsl/>.

- 
- [120] G. M. Bell and D. A. Lavis, *Statistical mechanics of Lattice model*, vol. 1 (Ellis Horwood Ltd., Chichester, 1989).
- [121] S. Dietrich and M. Napiórkowski, Phys. Rev. A **43**, 1861 (1991).
- [122] K. Binder, D. Landau, and M. Müller, J. Stat. Phys. **110**, 1411 (2003).
- [123] B. Groh and S. Dietrich, Phys. Rev. Lett. **72**, 2422 (1994).
- [124] B. Groh and S. Dietrich, Phys. Rev. E **50**, 3814 (1994).
- [125] B. Groh and S. Dietrich, Phys. Rev. E **54**, 1687 (1996).
- [126] J. Köfinger, N. B. Wilding, and G. Kahl, J. Chem. Phys. **125** (2006).
- [127] N. B. Wilding, F. Schmid, and P. Nielaba, Phys. Rev. E **58**, 2201 (1998).



# Curriculum vitae

Nima Farahmand Bafi

- seit 2012 Doktorand  
Max-Planck-Institut für Intelligente Systeme, Stuttgart &  
Institut für Theoretische Physik IV, Universität Stuttgart  
Prof. Dr. S. Dietrich
- 2014-2016 Studiengang *Master of Music*  
Die Staatliche Hochschule für Musik und Darstellende Kunst Stuttgart
- 2010-2012 Masterarbeit  
Max-Planck-Institut für Intelligente Systeme, Stuttgart &  
Institut für Theoretische und Angewandte Physik, Universität Stuttgart  
Prof. Dr. S. Dietrich
- 2010-2014 Studiengang *Bachelor of Music*  
Die Staatliche Hochschule für Musik und Darstellende Kunst Stuttgart
- 2009-2012 Studiengang *Master of Science in Physics*  
Universität Stuttgart
- 2003-2009 Studiengang *Bachelor of Science in Physics*  
Sharif University of Technology, Teheran

